

# **Control system design for twisted and coiled polymer actuators**

Dissertation

Motoya Suzuki

Tokyo Denki University

March 2019

## Abstract

Robots that interact with humans must be safe, which sometimes requires that they be soft. Many types of soft actuators—which are lightweight and flexible and move in a smooth, lifelike manner—have been developed to establish compliant motion in robots. In 2014, Haines et al. reported a novel soft actuator, called a twisted and coiled polymer actuator (TCPA), that is fabricated by twisting, coiling, and annealing nylon fibers such as nylon thread or fishing line. TCPAs exploit the thermomechanical properties of nylon fibers to expand and contract by heating and cooling. TCPA is extremely inexpensive to fabricate; compared to a conventional motor, TCPA's power/mass ratio is quite high and it is 20% more deformable. To ease implementation and actuation, electro-active TCPA has been developed. Electric activation via Joule heating can be easily carried out by fabricating the TCPA by using conductive nylon fibers or twining heating wire to the nylon fibers. These properties have prompted the development of a variety of applications of TCPA.

Modeling and control methods are crucial for realizing robotic applications of TCPA; however, such methods have not yet been established. Control system design is difficult because of the effects of input saturation, appropriate PID gain tuning, and parameter variation, as well as the need for simple and robust control methods that do not require extensive experience in control system design.

In this thesis, we construct a robust and simple control system based on simple actuator models. In designing the control system, we investigate its response properties using frequency response analysis and derive a simple model that accounts for material properties based on experiments results. Further, we propose a control system design and verify its validity through numerical simulations and experiments. We then demonstrate the application of our modeling and controller designs to robotics by applying an antagonistic actuator to the 1link manipulator.

In modeling experiments, we derive a simple actuator model consisting of nonlinear statics and linear dynamics. Our proposed control system achieves good results compared to conventional control methods and can be implemented easily, owing to its extremely simple structure. Our proposed model and control system design can be applied and implemented in combination to simplify application. Therefore, the methods described in this thesis can contribute to TCPA applications.

## **Acknowledgments**

In the completion of this thesis, I am very grateful to my supervisor, Associate Professor Norihiro Kamamichi, for his attentive support and suitable suggestions. I have spent 3 worthwhile years in Soft mechanics Laboratory and I have learned a number of valuable matters concerning the research and job hunting. I am grateful to all judges for this thesis. I also wish to sincerely thank Dr. Jun Ishikawa, Dr. Akio Nakamura, Dr. Masami Iwase, for judge of my doctoral degree. Furthermore, I wish to thank my boss in Mitsubishi Electric corporation Living environment laboratory, Mr. Akira Sakai, for his recommendation. I also wish to sincerely thank fellow students, Mr. Satoshi Soga, Mr. Yuji Noguchi, Mr. Keishiro Nagase and Teppei Muraki, for their help. Finally, I would like to offer my special thanks my parents.

Motoya Suzuki

# Table of contents

- 1 **Introduction**..... 1
  - 1.1 Electro-active polymers.....1
  - 1.2 Twisted and coiled polymer actuator.....2
  - 1.3 Research task.....6
  - 1.4 The contents of the thesis.....8
  
- 2 **Modeling**.....9
  - 2.1 Background of TCPA modeling.....9
  - 2.2 Modeling method.....10
    - 2.2.1 Fabrication methods.....10
    - 2.2.2 Experimental environment.....11
    - 2.2.3 Frequency response analysis.....12
  - 2.3 Experiment results.....13
  - 2.4 Discussion.....15
    - 2.4.1 Model of the TCPA.....15
    - 2.4.2 Verification of actuator model.....16
  - 2.5 Summary.....17
  
- 3 **Control system design**.....19
  - 3.1 Introduction of controller design for TCPA.....19
  - 3.2 Anti-windup compensator for TCPA.....20
    - 3.2.1 Controller design based on anti-windup compensator.....20
    - 3.2.2 Numerical simulations of PI control with anti-windup compensator.....22
    - 3.2.3 Experiment verification of anti-windup compensator.....28
  - 3.3 Robust control for TCPA.....35
    - 3.3.1 Controller design based on disturbance observer.....35

3.3.2 Numerical simulation of disturbance observer.....	39
3.3.3 Experiment verification of disturbance .....	43
3.4 Simple controller design based on internal model control method.....	49
3.4.1 Controller design based on internal model control method.....	49
3.4.2 Experimental environmental and system identification.....	52
3.4.3 Experimental verification of internal model control.....	54
3.5 Summary.....	60
<b>4 Application to robotic systems.....</b>	<b>61</b>
4.1 Introduction of robotic system with TCPA.....	61
4.2 Antagonistic-actuator.....	62
4.2.1 Modeling and control of antagonistic-type actuator.....	62
4.2.2 Numerical simulation of the displacement control.....	65
4.2.3 Experiment verification of the displacement control.....	72
4.3 Control system design for robot-arm with antagonistic-actuator.....	81
4.3.1 Modeling of robot arm.....	81
4.3.2 Control system design for robot arm.....	84
4.3.3 Numerical simulations and experiments.....	85
4.4 Summary.....	87
<b>5 Conclusion .....</b>	<b>88</b>
<b>References .....</b>	<b>88</b>

## Table of Figures

Figure 1. Fabrication image of TCPAs.....	3
Figure 2. Actuation image of TCPAs.....	3
Figure 3. Image of actuation mechanism of TCPAs.....	4
Figure 4. Actuation image of electro-active TCPAs.....	4
Figure 5. Robotic application of TCPAs.....	5
Figure 6. Displacement responses under wind speeds from 0.0 to 1.0 m/s.....	7
Figure 7. Fabrication of TCPA.....	11
Figure 8. Experiment environment for frequency response analysis.....	12
Figure 9. Experiment results of frequency response analysis.....	15
Figure 10. Actuator model from voltage to displacement.....	16
Figure 11. Verification results of actuator model.....	17
Figure 12. Block diagram of PI-AW control.....	22
Figure 13. Identification result.....	23
Figure 14. Simulation result of the normal PI control (pulse reference signals) .....	25
Figure 15. Simulation result of the PI-AW control (pulse reference signals) .....	26
Figure 16. Simulation result of the normal PI control (step reference signals) .....	27
Figure 17. Simulation result of the PI-AW control (step reference signal) .....	28
Figure 18. Experimental environment for AW control experiment.....	29
Figure 19. Experiment result of the normal PI control (pulse reference signals) .....	31
Figure 20. Experiment result of the PI-AW control (pulse reference signals) .....	32
Figure 21. Experiment result of the normal PI control (step reference signals) .....	33
Figure 22. Experiment result of PI-AW control (step reference signals) .....	34
Figure 23. Maximum overshoot ratio in each experiment (n = 5, error means $\pm$ SD) .....	34
Figure 24. Actuator model from voltage to displacement.....	36
Figure 25. Block diagram of feedback control system with disturbance observer.....	39
Figure 26. Identification result of the dynamics from voltage to displacement.....	40
Figure 27. Simulation result of feedback control without the disturbance observer.....	42
Figure 28. Simulation result of feedback control with disturbance observer.....	43
Figure 29. Experiment system.....	44
Figure 30. Experiment result of the normal feedback control.....	45
Figure 31. Experimental result of feedback control with disturbance observer.....	46

Figure 32. Comparison of RMSE in experiments results (n=5, error means $\pm$ SD) .....	47
Figure 33. Comparison of the experiment results (n=5, error means $\pm$ SD) .....	48
Figure 34. The block of diagram internal model control system.....	52
Figure 35. Experiment environment for internal model control.....	53
Figure 36. Identification results of the actuator model.....	54
Figure 37. Experiment result of the feedforward control with the sinusoidal wave.....	55
Figure 38. Experiment result of the proposed control method with the sinusoidal wave.....	56
Figure 39. Experiment result of the conventional feedforward control of step response.....	57
Figure 40. Experiment result of the internal model control in step response.....	58
Figure 41. The response property due to the variation of the time constant $\lambda$ .....	60
Figure 42. Antagonistic-type TCPA.....	62
Figure 43. Block diagram of the TCPA's model.....	63
Figure 44. Control system design of antagonistic TCPA.....	64
Figure 45. Identification result of the force-displacement model.....	66
Figure 46. Identification result of the voltage-displacement model.....	67
Figure 47. Simulation result of single actuator.....	69
Figure 48. Simulation result of antagonistic actuator.....	70
Figure 49. Simulation result of a single actuator in pulse wave.....	71
Figure 50. Simulation result of an antagonistic actuator in pulse wave.....	72
Figure 51. Experimental system.....	73
Figure 52. Experiment result of a single actuator.....	74
Figure 53. Experiment result of antagonistic actuator.....	75
Figure 54. Experiment results of a single actuator in pulse wave.....	76
Figure 55. Experiment results of an antagonistic actuator in pulse wave.....	77
Figure 56. Block diagram of 2 DOF-PID control.....	79
Figure 57. Experiment result of Feedforward control.....	80
Figure 58. Experimental result of 2DOF-PID control.....	81
Figure 59. The block of diagram of actuator model.....	82
Figure 60. The model of robot arm.....	83
Figure 61. The block diagram of robot model.....	83
Figure 62. The control system of the manipulator.....	85
Figure 63. Numerical simulation results of motion control.....	86
Figure 64. Experiment result of motion control.....	86

# 1. Introduction

In this chapter, the introduction of this paper is explained. We explain background, research tasks and purpose of this paper.

## 1.1. Electro-active polymers

Soft actuators have received much attention in robotics and nursing care applications due to their safe and biomimetic smooth motions. Many types of soft actuators have been developed, *i.e.*, a pneumatic muscle, a shape memory alloy (SMA) actuator, an electro active polymer actuator and a bio-actuator. In particular, compared to conventional actuators, soft actuators based on high polymers are one of the most promising actuators because of possibilities of miniaturization and high power density. It is called as electro-active polymer (EAP) actuator and is activated by electric stimulate.

Many EAP actuators have been developed. According to the electric characteristics of typical EAP materials, EAPs are divided into a dielectric type EAP, a conductive polymer type EAP and an ionic polymer-type EAP. The characteristics of each EAP are described below.

- Ionic polymer metal composite

An ionic polymer metal composite (IPMC) responds to the electrical stimulate because of mobility of ions in high polymer. This actuator can be actuated by low voltage (1~3 V). The IPMC can be bended by an electric stimulate.

- Dielectric elastomer actuator

A mechanism of a DEA is electrostriction effect that produces shape change or mechanical deformation by applying an electric field. A polymer with high dielectric constant and low elastic stiffness can generate large strain by applying large voltage (kV order) since the induced strain is proportional to a square of electric field.

- Conductive polymer actuator

A conductive polymer actuator can generate the large displacement due to their electrochemical oxidation/reduction. This actuators generally require low voltage in the range of 1~4 V.

For realizing practical application of the soft actuators, good combination of performance characteristics such as power density, fabrication cost, displacement and controllability [1]. Although an ionic-

polymer metal composite (IPMC) can realize large deformation by low voltage (1-3 V) and high speed motion, fabrication cost is relatively high and the IPMC has unwanted property such as nonlinear dynamics and stress relaxation [2]. A dielectric elastomer actuator (DEA) can realize large strain (<400 %), but the DEA requires high actuation voltage (kV order) [3]. A conducting polymer actuator can realize large deformation by low voltage (1-4 V), but response speed is slow [4]. Therefore, a novel soft actuator having great property is desired.

## 1.2. Twisted and coiled polymer actuator

In 2014, Haines *et al.* reported a novel soft actuator made from Nylon fibers such as a fishing line [5]. The actuator can be easily fabricated by twisting and coiling Nylon thread. The fabrication image is shown in Figure 1. From the fabrication method and the structure, this actuator is called as twisted and coiled polymer actuator (TCPA) [6], super coiled polymer (SCP) actuator [7] or twisted and coiled actuator (TCA) [8]. The actuation mechanism of TCPA is based on thermos-mechanical response that the twisted and coiled Nylon fibers contract or extend by heating and cooling. The actuation image is shown in Figure 2. The TCPA is contract and extend by heating and cooling.

The TCPA has remarkable properties as follows:

- Its fabrication cost is extremely low since it is easily fabricated by commercially available Nylon fibers.
- It realizes large deformation over 20 %.
- It is flexible and lightweight.
- Its motion is silent.
- The actuation environment is unbounded, such as in water, in wet condition or in magnetic field.
- Compared to the shape memory alloy actuators, a hysteresis property of TCPA is small.

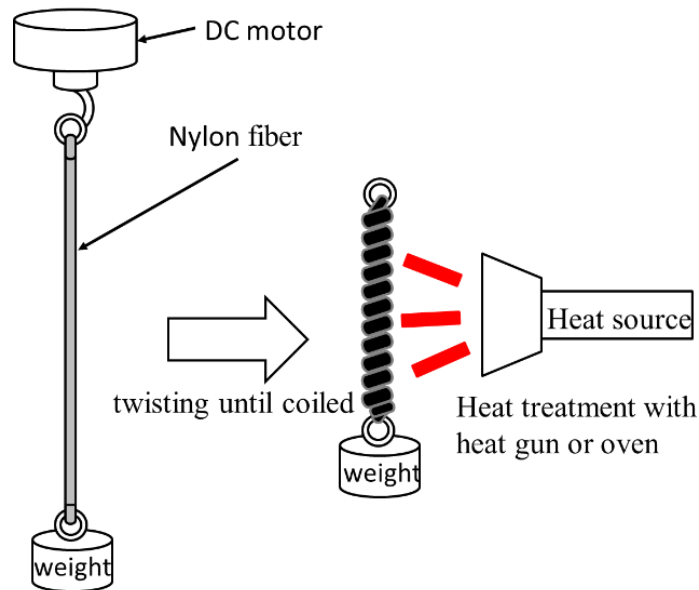


**Figure 1.** Fabrication image of TCPAs

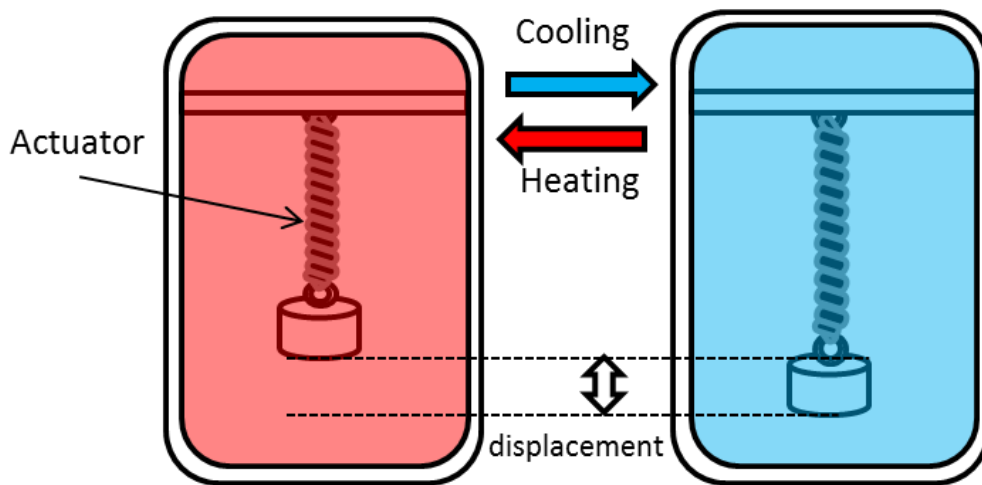


**Figure 2.** Actuation image of TCPAs

This actuator is based on thermo-mechanical properties of Nylon fibers. Figure 3 shows an image of the actuation mechanism. Twisting and coiling Nylon fibers, an internal molecular becomes twisted state. Internal molecular of Nylon fibers becomes alienated state when the fibers are heated. Therefore, the actuator contracts because giant torque is generated for making an internal molecular untwist-sate when the actuator is heated. The actuator expands because inverse torque is generated for making internal molecular twist-state when the actuator is cooled.

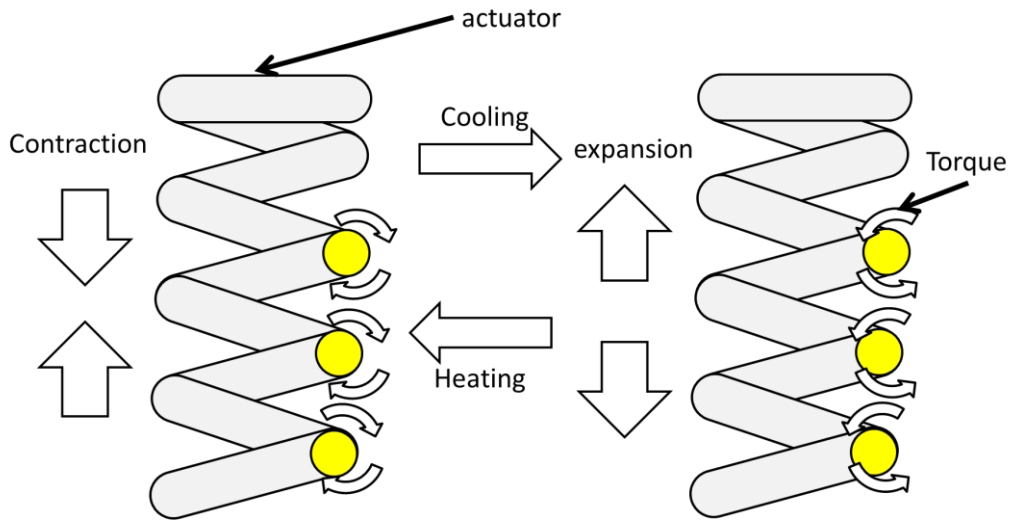


**Figure 3.** Image of actuation mechanism of TCPAs [5]

As a simple way of actuation and implementation, an electro-active TCPA driven by electrical input has been reported. The actuation mechanism of the electro-active TCPA is shown in Figure 4. This type of TCPA is fabricated with conductive Nylon fibers or twined with a heating wire, and can be driven easily by Joule heating [9]. By using the electro-active TCPA, a control system and driving circuit can be implemented simply. From these properties, various applications to robotics systems have been developed such as a robotic hand [10, 11, 12, 13], a power assist system [14, 15], a mobile robot [16], a morphing mechanism for flying robots [17], robot skin for human robots [18] and biomimetic robots [19]. In particular, various robotic hands of the electro-active TCPA have been developed. Examples of robotic application are shown in Figure 5. These applications are suitable for cure application and biomimetic application because of lightness and softness.

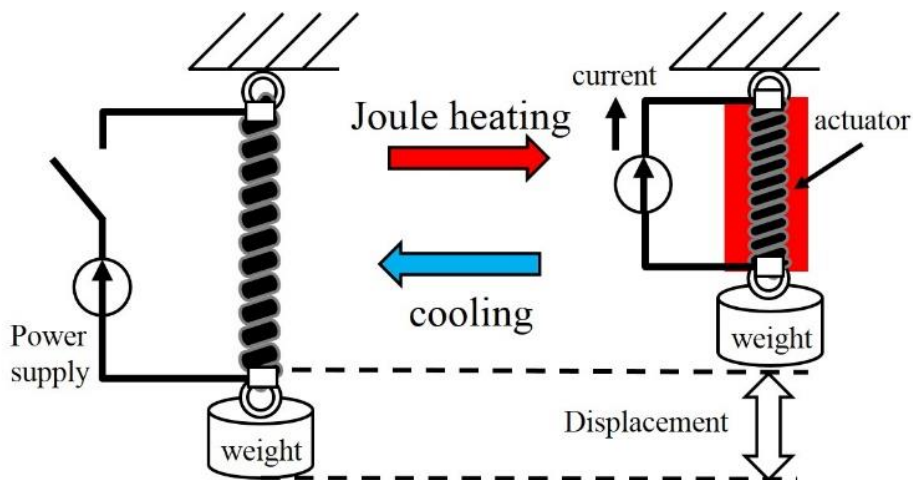
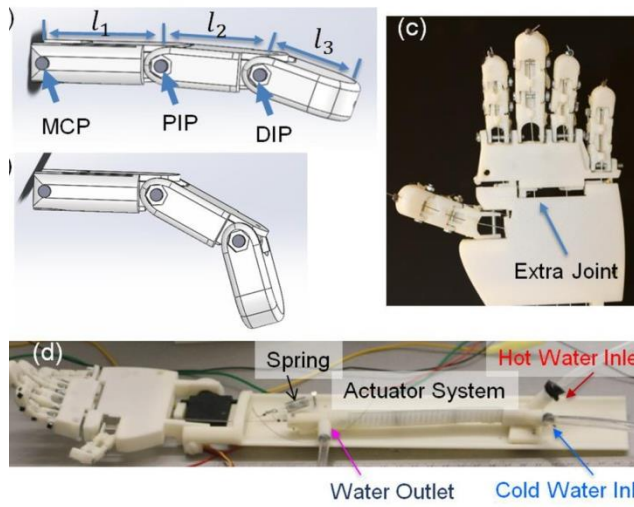


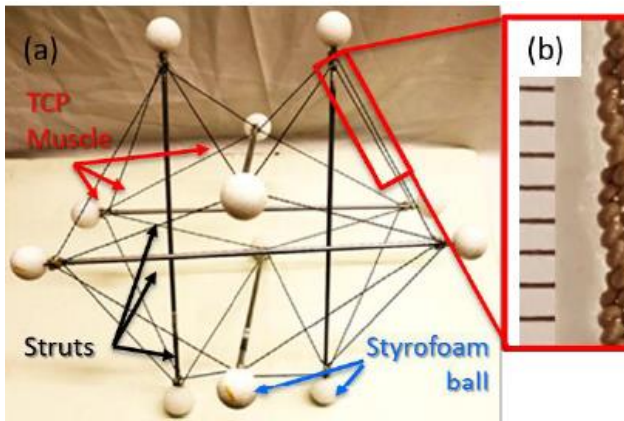
**Figure 4.** Actuation image of electro-active TCPAs



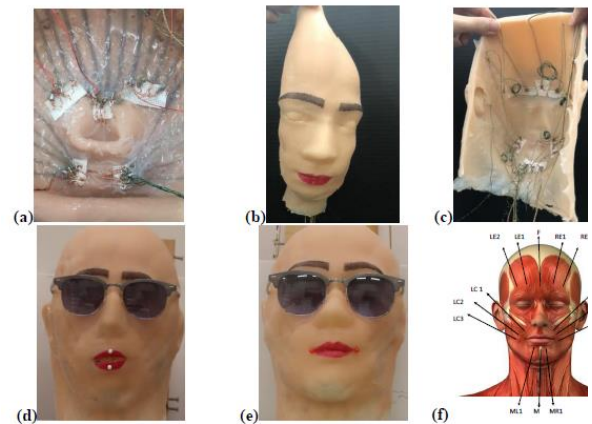
(a) Robotic hands by 3D printed [10]



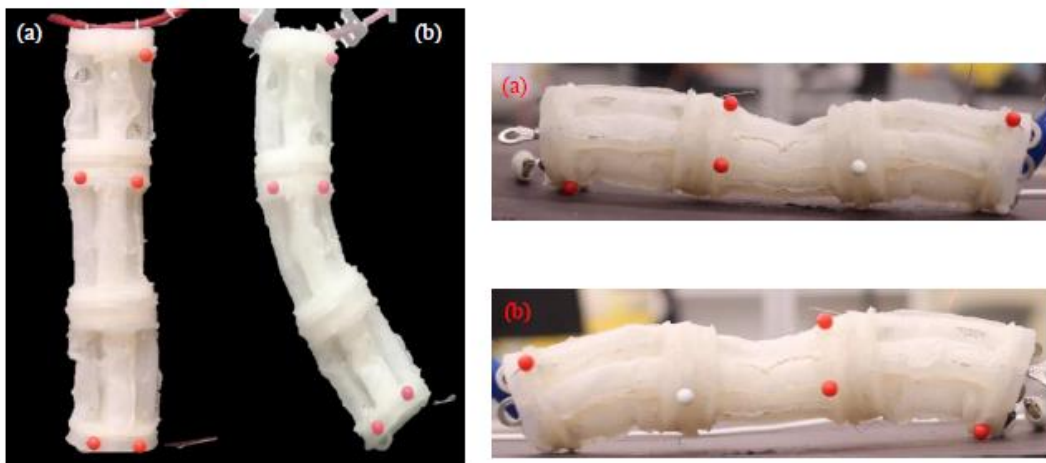
(b) power assist system [15]



(c) mobile robots [16]



(d) robot skin for human robots [18]



(e) bio-mimetic robots [19]

**Figure 5.** Robotic application of TCPAs

### 1.3. Research task

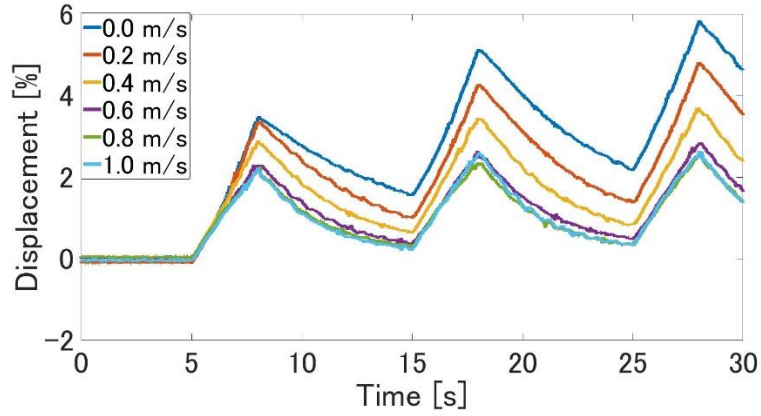
This actuator is suitable for robotic application because of low fabrication cost and good response performance. For realizing successful robotic application using the TCPA, synergetic integration of material development and control system design for the TCPA is desired. In particular, modeling and control methods considering material properties of the TCPA are important. The control system was mostly designed based on the nominal model of actuation dynamics, and linear feedback controllers were applied [20, 21]. Furthermore, the nonlinear feedback control methods had been demonstrated for realizing the high control performance [22, 23]. These control methods might achieve a good control performance of the single TCPA in static environments; however these control methods are designed without considering robustness against the actuation environment and disturbances. Actuation regulations and actuator dynamics quite depends on actuation environments because of the thermo-mechanical properties. The control system design considering the actuation environment is desired because robots using the TCPA are actuated in various environments. In particular, a following problem makes robotic application difficult:

- Input saturation

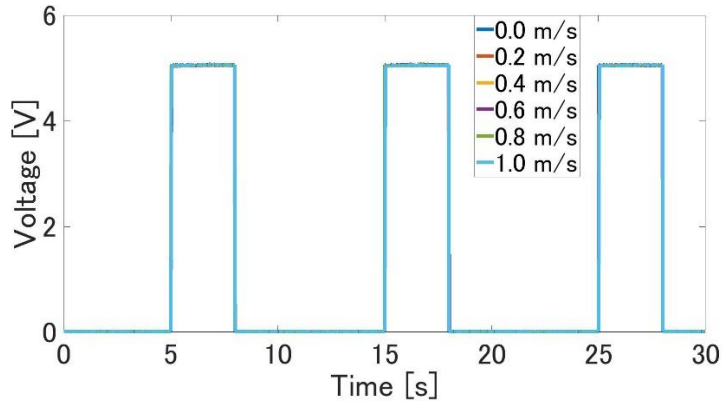
In case of driving by joule heating, the input saturation of the control signals should be set to prevent the TCPA from overheating. In addition, The negative control input to cool the actuator cannot be applied, then the input voltage needs to be set to 0 V and the actuator is cooled by heat dissipation. The input saturation may cause unwanted effects such as higher overshoot, a long settling time and even instability. The performance of the control system may be deteriorated by windup phenomena because of a rapid change of the target value or disturbance. The good control performance might not be realized because of this problem when the TCPA is applied to robots.

- Parameter variation

The output response of the TCPA is influenced by various conditions such as an ambient wind speed [20], a fabrication method [22, 23] and materials properties [5]. Figure 6 shows displacement responses of the electro-active TCPA under some wind speeds from 0.0 to 1.0 m/s. To evaluate the displacement response against variations of wind speeds, square wave with amplitude 5 V as the input voltage is applied under all of wind speeds. The good control performance might not be realized because of these parameter variations when the TCPA is applied to robots.



(a) Displacement



(b) Input voltage

**Figure 6.** Displacement responses under wind speeds from 0.0 to 1.0 m/s

Therefore, the robust control considering the actuation conditions and environment is desired for realizing successful robotic application using the TCPA. We should design the adequate control system depending on the actuation condition and purpose. In this thesis, we construct robust and simple control system based on simple actuator models for realizing robotic application. Actuator properties from an input voltage to a displacement are analyzed by frequency response analysis. Based on the analysis result, a simple transfer function model of the TCPA is derived. To resolve research task of the controller design, control systems based on simple actuator models is proposed. The validity of control systems is verified through numerical simulations and experiments. Furthermore, the robotic application of TCPAs is demonstrated. We apply the TCPA and a feedback control to a robot-arm. The validity of the control system of the robot-arm is verified through numerical simulations and experiments.

## **1.4. The contents of the thesis**

The rest of the thesis is organized as follows:

### **Chapter 2: Modeling**

This chapter shows that we investigate the frequency response through experiments. Based on experiment results, we constructed the actuator model. The validity of actuator model is verified.

### **Chapter 3: Control system design**

TCPA has many problems such as nonlinear properties, parameter-variation, input saturation and parameter-tuning. To solve these problems, the control system design for TCPA is proposed. The validity of the control system was verified through numerical simulations and experiments.

### **Chapter 4: Application to the robotic system**

In this chapter, we propose antagonistic-actuator for robotic application. Furthermore, the antagonistic actuators are applied to a robot-arm. The dynamical model of the robot is derived for numerical simulations. The angle control system is applied to robot-arm. The validity of the control system design is verified through numerical simulations and experiments.

### **Chapter 5: Conclusion**

This chapter summarizes the results and contributions of modeling and control system design. Furthermore, we explain future works.

## 2. Modeling

In this chapter, the modeling of the TCPA is explained. We analyzed the actuator properties and derived the simple model based on input-output data.

### 2.1. Background of TCPA modeling

For application and numerical analysis, many researchers reported a model of TCPA. Sharafi and Li proposed an accurate physical model [26]. Yang and Li focused on the microstructure, and they modeled the strain as a function of temperature. [27]. Cho *et al.* analyzed a nonlinear property of the TCPA and identified a nonlinear model by curve fitting [28]. Abbas and Zhao proposed dynamical model considering spring-structures [29]. Masuya *et al.* reported a nonlinear dynamical model based on an energy balance and a convective heat transfer [30]. Karami *et al.* proposed a nonlinear electro-mechanical model based on a phenomenological approach [31]. Tang *et al.* derived actuator models by a finite element method [32]. These models can simulate a behavior of the actuator; however, these accurate models are not suitable for controller design since the model structure is complex and number of parameters is larger. The simple model considering the linearity of actuator dynamics is desired. For control system design, applications and numerical simulations, actuator models should be expressed as linear time invariant (LTI) systems such as the transfer function or state-space model, which is often used in control engineering. Several researchers derived the LTI model of actuator from a time response of the actuator. Yip and Niemyer derived actuator dynamical model from an electric power to generated force or strain as a linear transfer function [20]. Arakawa *et al.* identified dynamical model as a linear time invariant black box model [21]. Here, we explain famous example as the dynamical model of Yip and Niemyer [20]. This actuator model can be expressed as construction of two sub-systems:

$$m \frac{d^2 y(t)}{dt^2} + d \frac{dy(t)}{dt} + ky = c\Delta T(t), \quad (1)$$

$$C_v \frac{d\Delta T(t)}{dt} = -\alpha S_c \Delta T(t) + \frac{v^2(t)}{R} \quad (2)$$

where  $y(t)$  is a displacement,  $\Delta T(t)$  is a temperature change from an ambient temperature,  $v(t)$  is an input voltage.  $m$ ,  $d$  and  $k$  are mechanical parameters, *i.e.* mass, damping coefficient and spring constant.  $C_v$  is a heat capacity,  $\alpha$  is a heat transfer coefficient,  $S_c$  is an area of the surface of the TCPA,  $c$  is

a proportional coefficient and  $R$  is an electric resistance. This model nonlinear consist nonlinear statics of joule heating and linear dynamics from electric power to displacement. Although the structure of this linear dynamical model is simple for control system design, the validated region of the motion is unclear since the restricted time responses were investigated. In particular, the frequency response of the actuator has not been investigated yet. Therefore, the actuator model for the control system design needs to be derived since the actuator modeling for control system designs has not been established yet.

In this chapter, we investigate the frequency response of the actuator for modeling of TCPA. The frequency response analysis is useful for control system design and the characteristics of measurement frequency range is able to derived. We perform experiment of frequency response analysis from an input voltage to a displacement. Based on experiment results, we investigated the validity of the actuator model derived by frequency response analysis.

## **2.2. Modeling method**

For modeling of the TCPA, the electro-active TCPA needs to be fabricated. In this section, we explain fabrication methods and modeling methods of the TCPA.

### **2.2.1. Fabrication methods**

The fabrication method of the TCPA have been studied and reported in many previous researches; however the effective fabrication conditions such as payload, heating and annealing depend on types of materials. In this thesis, the fabrication conditions are determined by trial fabrications in preliminary experiments based on the method of the previous researches [5].

The TCPA used in this research was fabricated by the silver-plated Nylon thread (AGposs 100/3, Mitsufuji). Fabrication procedures are as follows:

1. Setup: One-side of the Nylon thread is connected to a motor, and a weight is hung on the other side of the thread. In our experiment, the length of the Nylon thread is set as 300 mm and the weight of 50 g is used.
2. Twisting and coiling: The thread is twisted with the motor until the coil shape appears.
3. Heat treatment: To fix the coiled shape, an annealing process is conducted. In our experiment, a thermostatic oven is used, and the temperature is kept to 180 °C in an hour, then cool to the room temperature at a slow speed.

Here, the length of Nylon fibers was determined so that the length of the fabricated TCPA adjusts to the experimental setup. The payload to the Nylon thread was determined by preliminary experiments.

The actuation behavior of the fabricated TCPA is shown in Figure 7. The length of a normal state is 100 mm. When the voltage of 10 V was applied to TCPA where the weight of 50 g is suspended, the maximum actuation strain was about 10 %.

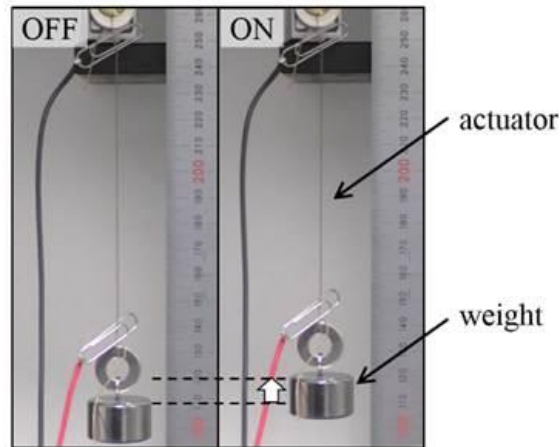


**Figure 7.** Fabrication of TCPA

### **2.2.2. Experimental environment**

In this section, we explain the experimental environment. A schematic diagram of our experimental environment is shown in Figure 8. The actuator is placed in a chamber (As-one). In the experimental environment, a temperature in the chamber is set as 23 °C. In the environments, a real-time measurement and frequency response analysis are carried out by using a frequency response analyzer (DS-3200, ONOSOKKI). The control input signal is computed in frequency response analyzer and applied to the power amplifier. The power amplifier outputs the driving voltage according to the control signal. The output of the actuator is measured by sensors and the output data is input to the frequency response analyzer. Here, we performed a frequency response analysis experiment from the voltage to the displacement and a frequency response analysis experiment from voltage to generated force separately. In the frequency response analysis experiment from the voltage to the displacement, the displacement data is measured by laser displacement meter (IA-100, KEYENCE) and a weight of 50 g is attached to the actuator.

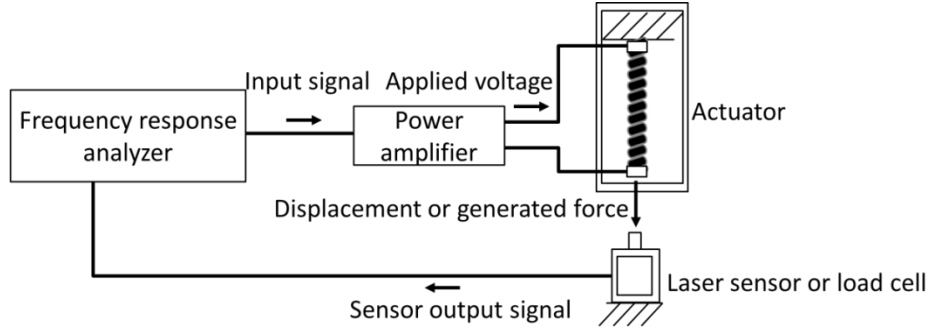


**Figure 8.** Experiment environment for frequency response analysis

### 2.2.3. Frequency response analysis

We explain methods of the frequency response analysis. For identifying the frequency response from input voltage to output, a sinusoidal wave voltage is applied to the actuator. The input voltage  $v(t)$  is given as

$$v(t) = A \sin(2\pi ft) + V_{offset} \quad (3)$$

where  $A$  is amplitude of a sinusoidal wave,  $f$  is frequency and  $V_{offset}$  is offset voltage. If dynamics from input voltage  $v(t)$  to output  $y(t)$  can be expressed as LTI model, the output can be expressed as

$$y(t) = B \sin(2\pi ft + \varphi) + BV_{offset} \quad (4)$$

where  $B$  is amplitude of a sinusoidal wave output, and  $\varphi$  is a phase delay. Note that  $y(t)$  is a displacement. Compare the sinusoidal wave of the equations (3-4), the phase delay  $\varphi$  can be derived. Furthermore, the gain  $ga$  can be calculated by  $ga=20\log_{10}(B/A)$ .

To confirm the linearity of the frequency response, coherences need to be derived. The frequency transfer function  $Z(j\omega)$  can be expressed as

$$Z(j\omega) = \left| \frac{B}{A} \right| e^{(j\omega + \varphi)} = \frac{D_p(j\omega)}{N_p(j\omega)} \quad (5)$$

where  $\omega$  is angular frequency,  $D_p(j\omega)$  is the polynomial denominator and  $N_p(j\omega)$  is the polynomial numerator of the identified transfer function. Here, the coherence is defined as

$$Coh(j\omega) = \frac{|D_p(j\omega) \cdot \bar{N}_p(j\omega)|}{|N_p(j\omega)|^2 |D_p(j\omega)|^2} \cdot \quad (6)$$

$$0 \leq Coh(j\omega) \leq 1$$

As the coherence is closer to 1, the linearity of the data is higher. If the coherence is close to 0, the actuator model is expressed as a LTI model difficulty. Therefore, frequency response analysis is performed by the following procedure:

1. Apply input voltage

Applying sinusoidal wave voltage  $v(t) = A \sin(\omega t) + V_{offset}$  to the actuator for joule heating, input-output data from input voltage to output displacement is measured.

2. Calculation of the frequency response

The gain  $ga$  and the phase delay  $\varphi$  are derived by comparing sinusoidal wave of the input and the output. From the gain  $ga$  and the phase delay  $\varphi$ , the frequency transfer function is calculated.

3. Calculation of the coherence

Inserting the denominator polynomial and the numerator polynomial of the frequency transfer function into the equation (6), the coherence is calculated.

Repeating process (1)-(3) in all frequency, we can derive a frequency response. Measuring input-output data and calculating the frequency response analysis are carried out automatically by the frequency response analyzer. The amplitude, offset voltage, frequency ranges are determined by using software of the frequency response analyzer.

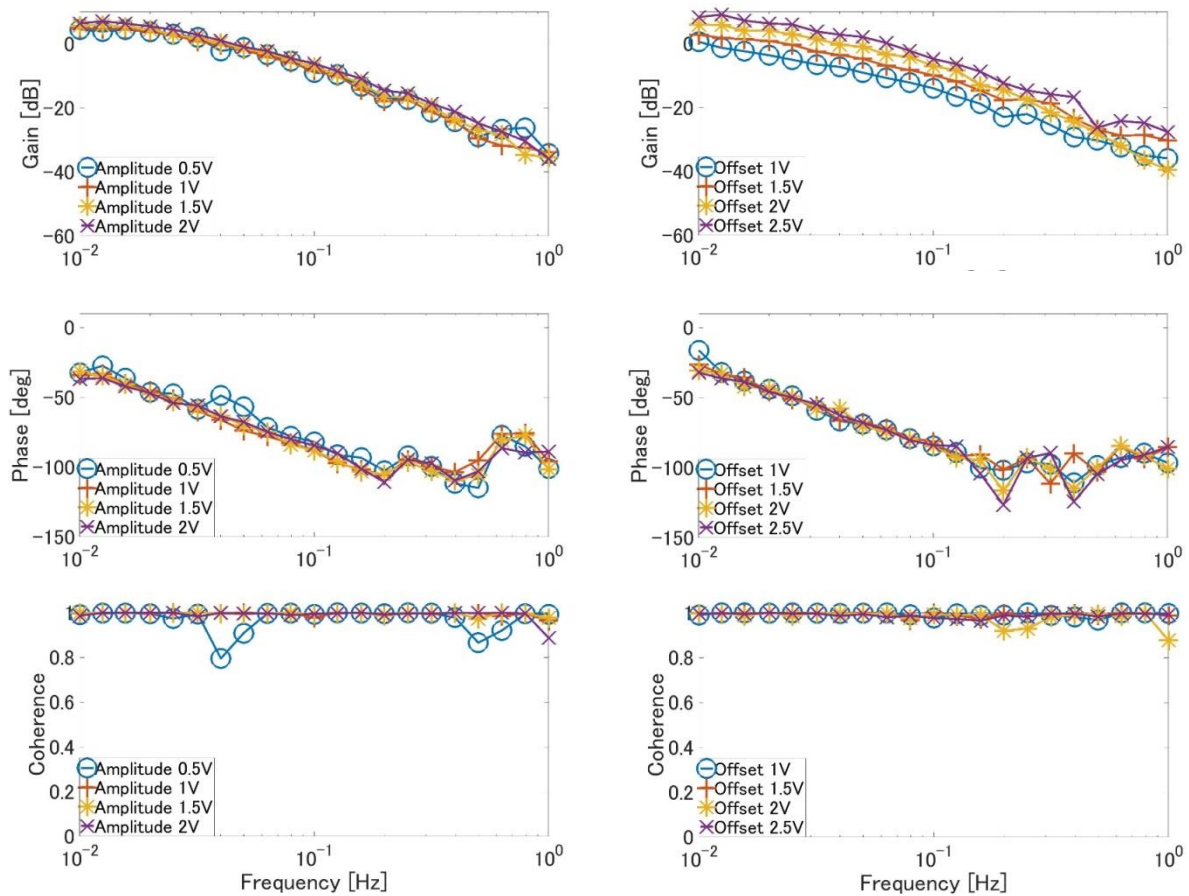
By using the frequency response analysis, the linearity of actuator dynamics can be investigated. Therefore, the validity of the simple model for control system design might be proved comparing the model and the frequency response.

### 2.3. Experiment results

In this section, we explain experiment result. We measured 21 data at equal intervals on the logarithmic axis in the range from 0.01 Hz to 1 Hz. Minimum frequency is 0.01 Hz because maximum frequency of the frequency response analyzer is 0.01 Hz. Maximum frequency is 1 Hz because the actuator cannot actuated from 1 Hz. Experimental data was average of three trials. Here, we analyzed frequency response on two conditions; 1) the offset voltage of input voltage is changed in steps of 0.5 V

and the amplitude of input voltage is constant. 2) the offset voltage is constant and the amplitude of input voltage is changed in steps of 0.5 V.

Experiment results from the voltage to the displacement are shown in Figure 9. In case of the constant offset voltage, the offset voltage was 2 V and the amplitude voltage was changed from 0.5 V to 2 V per 0.5 V. Although the amplitude increases, the gain value and the phase value of frequency response overlaps. The gain decreases with a slope of 20 dB/dec and the phase is close to -90 deg as the frequency is higher. The gain value and the phase value decrease after 0.01 Hz. In particular, the actuator dynamics are considered to have adequately linearity since the coherence of frequency response is close to 1 in all range. Actuator dynamics from the voltage to the displacement is considered to be expressed as LTI system because of the coherence. In case of the constant amplitude voltage, the offset voltage was changed from 1 V to 2.5 V per 0.5 V and the amplitude voltage is 1 V. As same as the constant amplitude voltage, the gain decreases with a slope of 20 dB/dec and the phase is close to -90 deg as the frequency is higher. The gain value and the phase value decrease after 0.01 Hz. The coherence is close to 1 in all frequency. The gain value increases as the offset voltage increases. These results also are considered to be occurred by nonlinearity of Joule's law.



(a) The offset voltage was 2 V and the amplitude

(b) The offset voltage was changed from 1 to 2.5

voltage was changed from 0.5 V to 2 V per 0.5 V V per 0.5 V and the amplitude voltage was 1 V

**Figure 9.** Experiment results of frequency response analysis

## 2.4. Discussion

From experiment results, actuator dynamics can be expressed as LTI system since the coherence is close to 1 in all frequency. However, the gain value increases as the offset voltage increases. In this section, the linear dynamical model is explained. The validity of the linear dynamical model is discussed considering the experiment results.

### 2.4.1. Model of the TCPA

Based on experiment results and previous papers, the actuator model is derived. Here, the nonlinear property from the input voltage to the electric power can be represented by Joule's law,

$$p(t) = \frac{v^2(t)}{R} \quad (7)$$

where  $R$  is electrical resistance,  $v(t)$  is the input voltage, and  $p(t)$  is the electric power. Although the electrical resistance varies slightly with the strain and temperature of the TCPA, the electrical resistance is considered to be constant [24]. From analysis results of the coherence, the actuator dynamics is assumed to be expressed as the LTI system. Based this assumption, the actuator is expressed as a system in Figure 10. The model consists of two sub-systems  $g$  and  $H$ , which are connected in series.  $g$  represents a nonlinear function as a square root function;

$$g(v) = v^2(t) \quad (8)$$

$H(s)$  represents dynamics from the squared input voltage  $v^2(t)$  to the output  $y(t)$ .  $y(t)$  is the generated force or the displacement. In experiment results, dynamics can be linearized as LTI model since the coherence is closer to 1 in all frequency. Therefore,  $H(s)$  is assumed to be expressed as the LTI system;

$$H(s) = \frac{y(s)}{u(s)} = \frac{b_m s^m + b_{m-1} s^{m-1} + \dots + b_0}{s^n + a_{n-1} s^{n-1} + \dots + a_0} \quad (9)$$

where  $a_i$  ( $i=1,2,\dots$ ) and  $b_j$  ( $j=0,1,2,\dots$ ) are the parameters of the actuator model,  $u$  is identified as  $u(t)=v^2(t)$  and  $m$  and  $n$  are the order of the actuator model.  $m$  and  $n$  is determined the order of the actuator model so that the controller system design is simple and adequate.

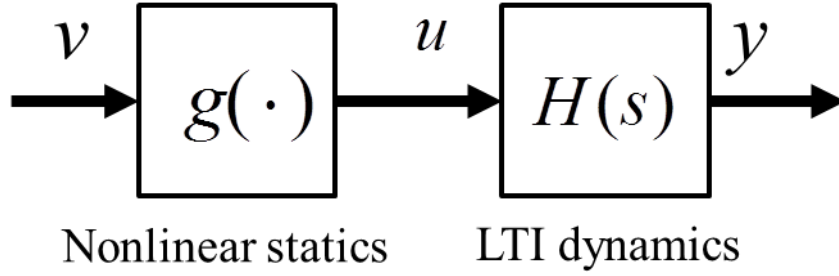


**Figure 10.** Actuator model from voltage to displacement

#### 2.4.2. Verification of actuator model

To investigate validity of the model, the frequency transfer function of the model is derived. Transforming the model using Laplace transform, the transfer function  $H(j\omega)$  of the actuator from  $u$  to  $y$  is expressed as

$$H(j\omega) = \frac{y(j\omega)}{u(j\omega)}. \quad (10)$$

If  $u(t) = v^2(t)$  is linearly approximated in the average voltage  $V_{offset}$ ,  $u$  is calculated by  $u \approx 2V_{offset} v$ . Therefore, the linearized model from  $u$  to  $y$  is expressed as

$$\frac{y(j\omega)}{v(j\omega)} = 2V_{offset} H(j\omega). \quad (11)$$

From the equation, the gain value increases because of the increase of the offset voltage  $V_{offset}$ . To verify the validity of actuator model, the frequency response of the experiment data divided by  $2V_{offset}$ . The experiment data divided by  $2V_{offset}$  is showed in Figure 11. Figure 11 shows that both the gain value and the phase value overlap. The actuator has nonlinearity of Joule heating and dynamics from squared voltage to output can be expressed as LTI systems. Therefore, the actuator model can simulate the experiment results.

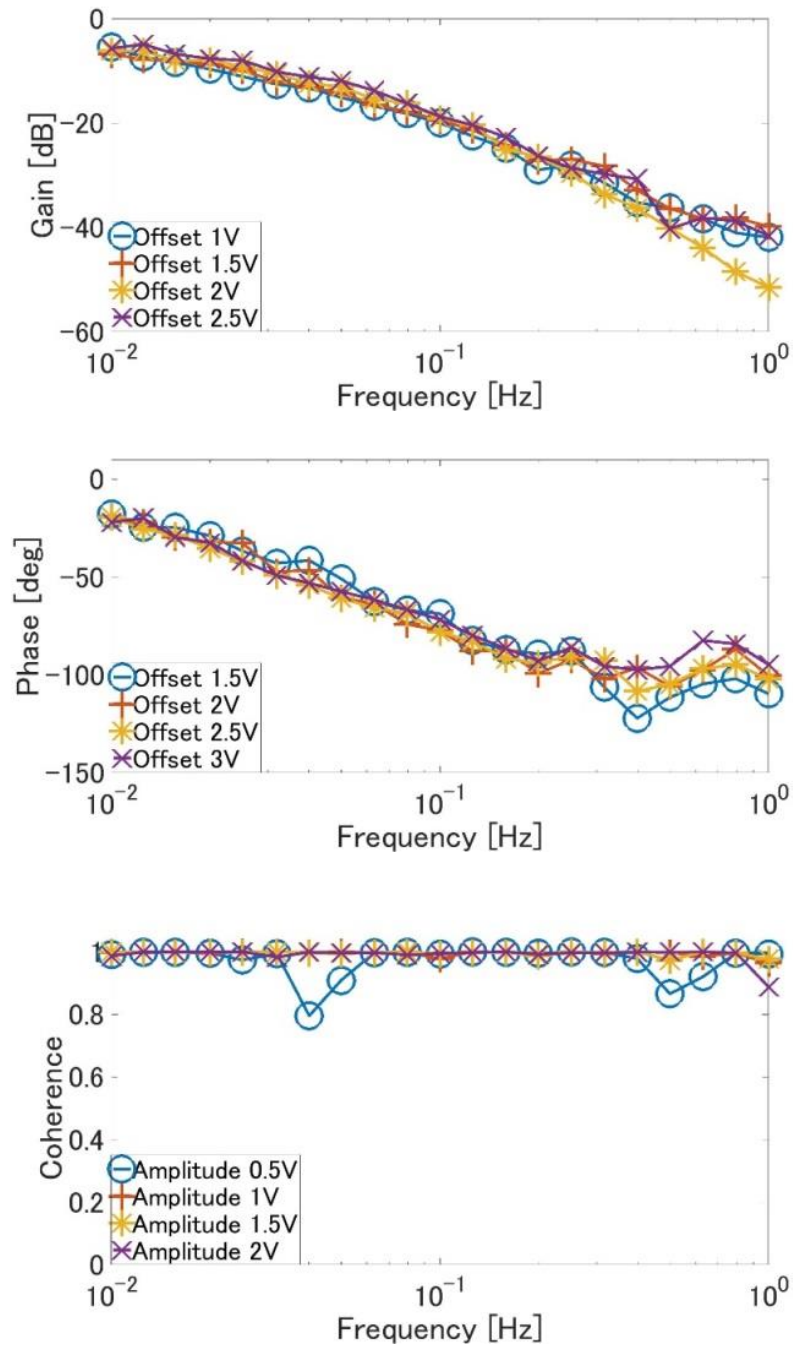


**Figure 11.** Verification results of actuator model

## 2.5. Summary

In this chapter, we focused on the simple model method of the electro-active TCPA. The linearity of the actuator dynamics was investigated through the frequency response analysis. Based on experiment results, the validity of the model was verified. Experiment results show that the actuator has the linear dynamics and the nonlinear statics of squared. At least, the model considering the nonlinear statics and

the linear dynamics can simulate the behavior of the actuator in low frequency range. The structure of the model is simple. Therefore, these experiment results can contribute the control system design for TCPAs.

### 3. Control system design

In this chapter, we explain the control system of the TCPA. We constructed the control system design base on actuator models. The validity of the controller was verified through numerical simulations and experiments.

#### 3.1. Introduction of controller design for TCPA

Various control methods of the electro-active TCPA have been reported with a view to the robotic applications. In many previous paper of the control system design, PID control is applied for control of the displacement or output force. By tuning PID gains, the desired control performance is realized. Yip and Niemeyer proposed a linear time invariant (LTI) model of the actuator based on the physical phenomena and designed a PD controller [20]. Arakawa et al. modelled the thermomechanical and thermoelectric property as a linear time invariant black box model and designed a PID and a PI-D controller based on the identified model [21, 33]. Sutton *et al.* designed a simple force control system based on the LTI first order model [34]. Luong *et al.* applied an adaptive PID sliding mode control to achieve high tracking and robust performance [24]. These control methods might achieve a good control performance of the single TCPA; however these control methods is designed without considering robotic applications. Actuation regulations and actuator dynamics quite depends on actuation environments because of the thermo-mechanical properties. The control system design considering the actuation environment is desired when the TCPA is applied to robotic applications because robots using the TCPA are actuated in dynamical environments. We focus a following task which is main problem for applications: 1) These control systems were designed without considering the effect of input saturation. 2) Tuning of the appropriate PID gains is difficult. Therefore, a control precision is deteriorated because of windup phenomena. 3) Actuator dynamic is varied by several conditions such as an external load, a wind speed and the fabrication method. The control system for TCPA should solve these tasks so as to make the structure of the controller as possible as simple. Designing the adequate control system depending on the actuation condition and purpose, the robotic application using the TCPA is realized.

In this chapter, the control system was proposed for solving each task separately. We proposed three control systems for solving main problem of robotic application. The validity of the control system design was verified through numerical simulations and experiments.

## 3.2. Anti-windup compensator for TCPA

The control system was mostly designed based on the modeling of actuation dynamics, and practical PID feedback controllers were applied. These control methods had been applied to achieve a good control performance of the TCPA; however, these control systems were designed without considering the effect of input saturation. In case of driving by joule heating, the input saturation of the control signals should be set to prevent the TCPA from overheating. In addition, it should be set due to the limitation of a driving circuit. Then, the performance of the control system is deteriorated by windup phenomena when the control signal is saturated by a rapid change of the target value or disturbance. The windup phenomena causes various unwanted effects such as a higher overshoot, a long settling time and even instability by the increasing of the integral action of the controller [35]. The performance of the control system may be deteriorated by windup phenomena because of a rapid change of the target value or disturbance when the TCPA is applied to robots. Although this problem can be solved by applying a feedback controller without using an integrator or with setting a low gain; the controller with the integrator and its appropriate gain setting is needed to achieve high tracking performance. In particular, the integrator on the controller should be applied so as to eliminate a steady state error between a reference signal and an output of the TCPA. Therefore, the control system design with considering the windup phenomena is desired.

To improve control performance, an anti-windup compensator is applied to the feedback controller for the TCPA. The control performance is verified through numerical simulations and experiments.

### 3.2.1. Controller design based on anti-windup compensator

In this section, we explain control system design methods for the TCPA. The diagram of the control system is shown in Figure 12. The control system consists of a nonlinear compensator, an input saturation and a feedback controller with anti-windup compensator.

For control system designs and numerical analysis, a model of the actuator is derived. Although the TCPA have been modeled in various ways such as a detailed model in consideration of physical phenomenon, these models are unsuitable for control system design due to complexity of the model structure and a number of parameters. To make the modeling for control system designs simple, a gray-box modeling based on the LTI model is applied with reference to methods of Yip and Niemeyer [20].

The response of the TCPA has relations to temperature, and in case of joule heating, temperature has relations to the applied electric power. Therefore, we assume that the model of TCPA consists of nonlinear statics of Joule's law and LTI dynamics from applied power to displacement. Note that the electric power is proportioned to the square of the applied voltage in the unchanged condition of electric resistance. Here, as with reference of Yip and Niemeyer [20], we assumed that the actuator model

can be expressed as construction of two sub-systems (1) and (2). Combine the equations (1) and (2), the actuator model from the input voltage  $v(t)$  to the displacement  $y(t)$  can be expressed as a linear ordinary differential equation:

$$\frac{d^3 y(t)}{dt^3} + a_2 \frac{d^2 y(t)}{dt^2} + a_1 \frac{dy(t)}{dt} + a_0 y(t) = b_0 v^2(t) \quad (12)$$

where  $a_{i(i=0,1,2)}$  and  $b_0$  is model parameters as  $a_2=(dRC_v+mRaS_c)/mRC_v$ ,  $a_1=(kRC_v+dRaS_c)/mRC_v$ ,  $a_0=kRaS_c/mRC_v$  and  $b_0=c/mRC_v$ . In this paper, model parameters in equation (12) are identified from experiment data.

To compensate the nonlinear statics of the TCPA, the series compensator for linearization is applied as

$$v(t) = \sqrt{u(t)} \quad (13)$$

where  $u(t)$  is a control signal calculated by the controller and  $v(t)$  is the input voltage. The equation (13) is the inverse nonlinearity compensator. By inserting the compensator (13) after the feedback controller, control system design based on a linear control theory can be considered.

Next, to avoid breaking of the actuator by overheating, the input voltage is limited within riskless driving voltage. The saturated control signal  $u(t)$  is given as

$$u(t) = \begin{cases} u_{\max} & (u_{\max} < u_c(t)) \\ u_c(t) & (u_{\min} \leq u_c(t) \leq u_{\max}) \\ u_{\min} & (u_c(t) < u_{\min}) \end{cases} \quad (14)$$

where  $u_{\max}$  and  $u_{\min}$  are limit of the square value of input voltage and  $u_c$  is the control signal of feedback controller. Note that the saturation is determined by the preliminary experiment.

A PI controller with the compensator called as anti-windup (PI-AW) is introduced. In this paper, the AW compensator of Reference [36] is applied to the TCPA. The windup phenomenon occurs due to the increasing of the integral quantity of the controller when the control signal is saturated. To solve this problem, the integral action is stopped by a feedback loop when the control signal is saturated. To realize the above mechanism, the control input  $u_c(t)$  is given as

$$u_c(t) = K_p \left( e(t) + \frac{1}{T_I} \int z(\tau) d\tau \right) \quad (15)$$

where  $z(t)$  is a new input of the integrator.  $z(t)$  is defined as

$$z(t) = e(t) - \frac{1}{K_p} (u_c(t) - u(t)) \quad (16)$$

where  $K_p$  is a proportional gain and  $T_I$  is an integral time. The equation (15) is equal to the normal PI controller when the control signal is not saturated. The integral action can be stopped by a feedback loop of  $u_c(t) - u(t)$  when the control signal is saturated. Therefore, the influence of the integral windup can be eliminated. The applied method is quite simple to design the control system and doesn't depend on actuator model. In addition, high tracking performance can be achieved due to effect of an integral action.

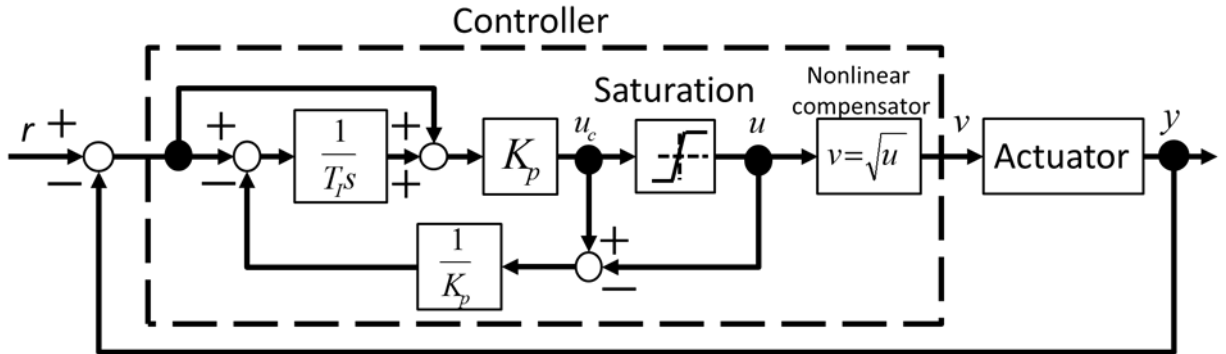


**Figure 12.** Block diagram of PI-AW control

### 3.2.2. Numerical simulations of PI control with anti-windup compensator

The validity of the control system is investigated through numerical simulations. First, we conduct numerical simulations based on the identified model. The TCPA used in the experiment was fabricated by the silver-plated Nylon thread (AGposs 100/2, Mitsufuji). The Nylon thread in uncoiled state is 300 mm length and 0.1 mm diameter. The configuration is 100 mm length and 0.3 mm diameter. The electric resistance is  $73.5 \Omega$  in unloaded condition. When the weight of 20 g is attached to the actuator, the maximum strain of the actuator is about 10 % by 10 V.

We identified the model parameters by using experiment data. In the experiment, the input-output data of pulse response was measured. In this experiment, the actuator was activated by voltage control, the pulse voltage with multilevel amplitudes was applied. The displacement was measured with a laser

displacement meter (KEYENCE: IA-100). The displacement is defined as shrinkage ratio [%] of the initial length of the actuator. In this experiment, a 20 g weight was attached to the actuator and the room temperature is 23 °C.

By using a system identification tool of MATLAB, the model parameters are identified as  $a_2=92.5$ ,  $a_1=2269$ ,  $a_0=836.9$  and  $b_0=94.44$ . The fitting ratio is 90.82 %. Identification results are shown in Figure 13. In this figure, the experimental data and simulation result of the identified model are plotted. The simulation results agree well with the experimental result.

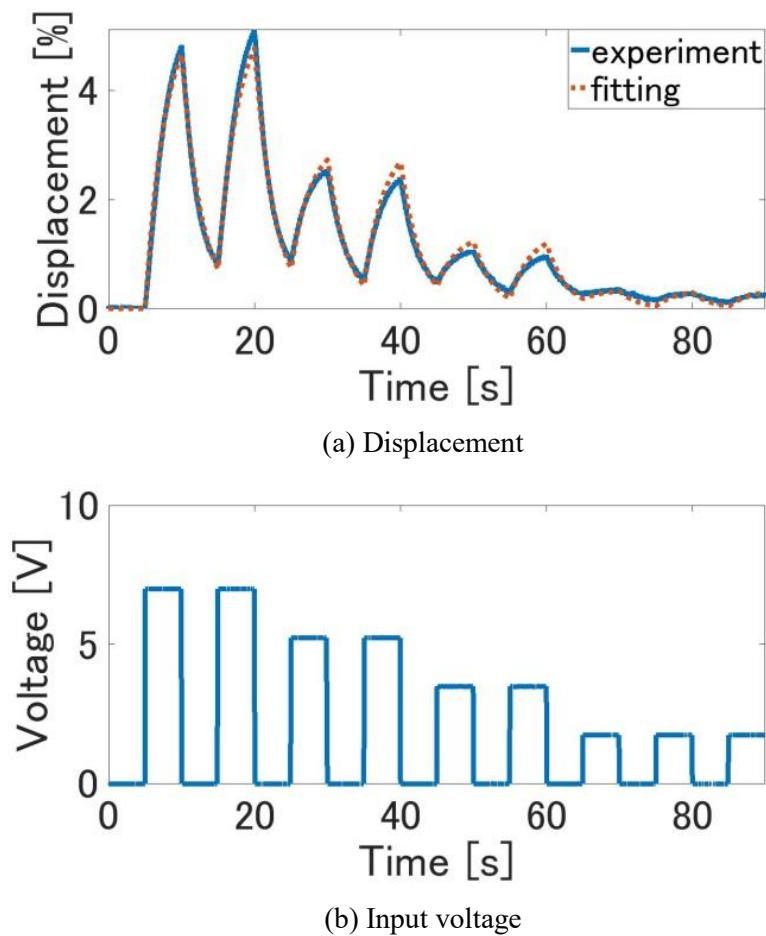
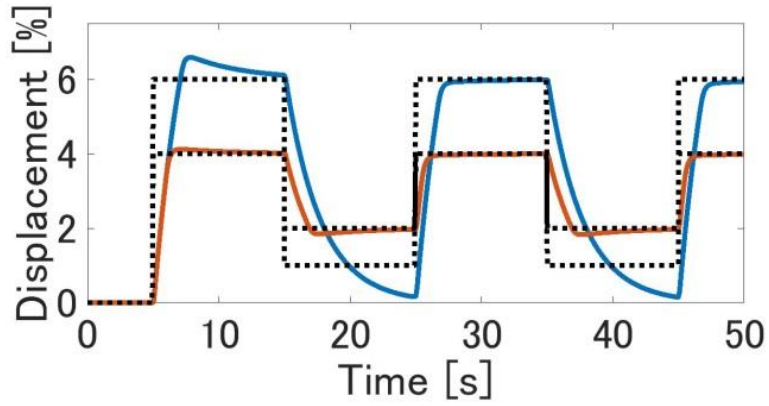


**Figure 13.** Identification result of model of TCPA

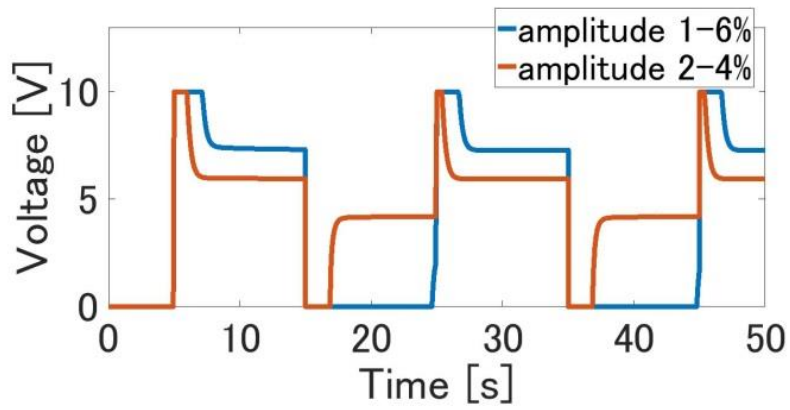
The numerical simulations are conducted by using MATLAB. In the numerical simulation, the output response of the actuator is calculated by using the differential equation of the actuator model and ode45 function of MATLAB. The maximum input  $u_{max}$  and the minimum input  $u_{min}$  are set as 100 V<sup>2</sup> and 0 V<sup>2</sup>, respectively, that is, the maximum input voltage  $V_{max}$  and the minimum input voltage  $V_{min}$

are 10 V and 0 V, respectively. The controller gains are set as  $K_p=80$ ,  $T_I=0.05$  in all simulations, so that the closed loop system becomes stable by using the identified model.

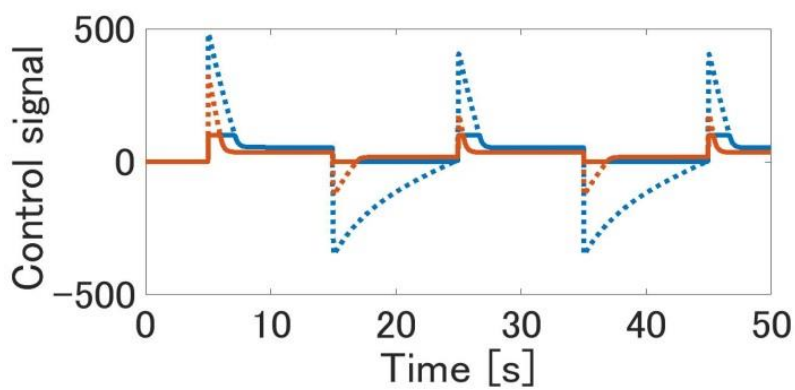
First, to verify the validity of the anti-windup compensator for repetitive expansion and contraction motions, the reference signals are set as pulse waves from 1 % to 6 % and from 2 % to 4 %. The simulation results of the PI control without the anti-windup compensator are shown in Figure 14. In case of relatively small range of motions, *i.e.* the reference signal from 2 % to 4 %, the overshoot is small and the displacement can be tracked to the reference signal since integral quantity of the tracking error has an insignificant effect. On the other hand, in case of relatively large range of motion, *i.e.* the reference signal from 1 % to 6 %, a large overshoot occurs in the first rise motion. In addition, in the stretch back motions, the displacement overshoots hugely and does not converge to the reference signal due to the accumulated integral quantity of the tracking error. As observed in the simulation results, the windup phenomena lead to unwanted behaviors such as large overshoot and long settling time. The simulation results of the PI-AW control are shown in Figure 15. The overshoot behavior is resolved and the displacement is able to track to the reference signals since the integral quantity is kept in adequate quantity even in large tracking errors by the anti-windup compensator. As shown in the results, even if large range of motions is applied, appropriate control performance is able to be achieved.



(a) Displacement (solid) and reference (dotted)

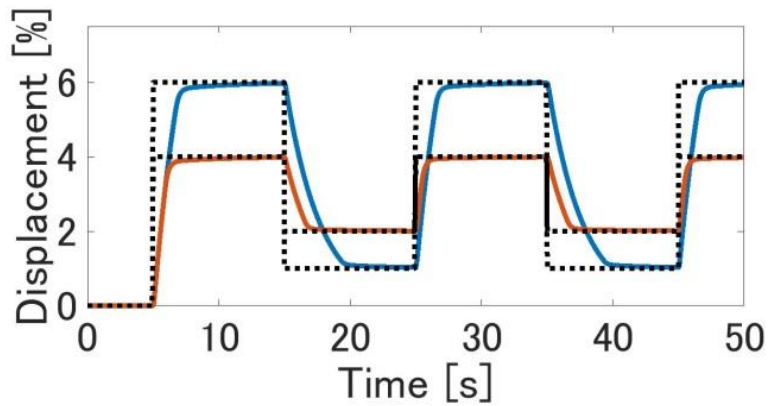


(b) Input voltage

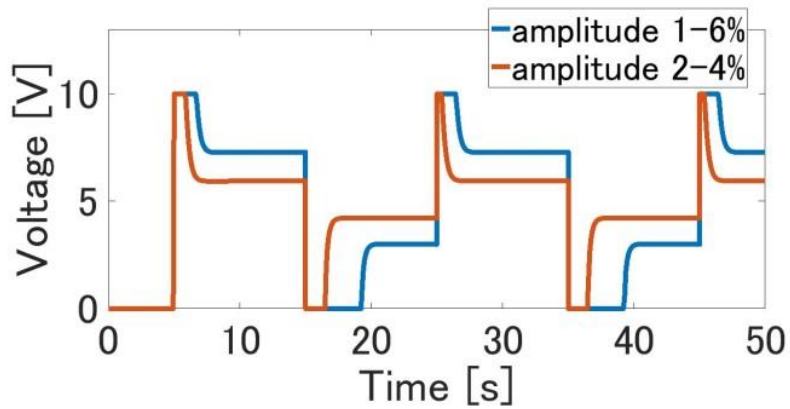


(c) Control signals from PI controller (dotted) and saturated signals (solid)

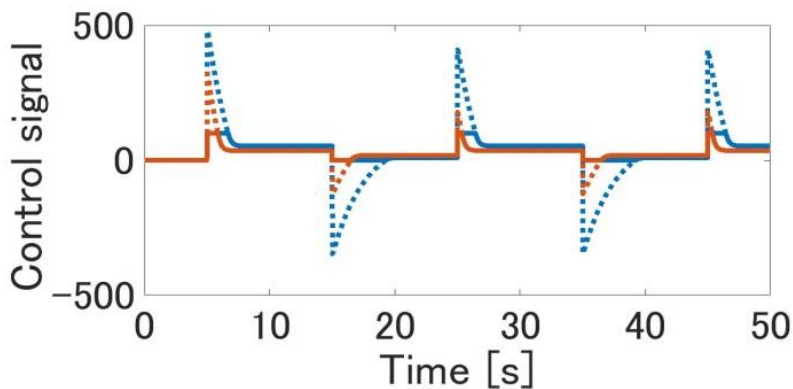
Figure 14. Simulation result of the normal PI control (pulse reference signals)



(a) Displacement (solid) and reference (dotted)



(b) Input voltage

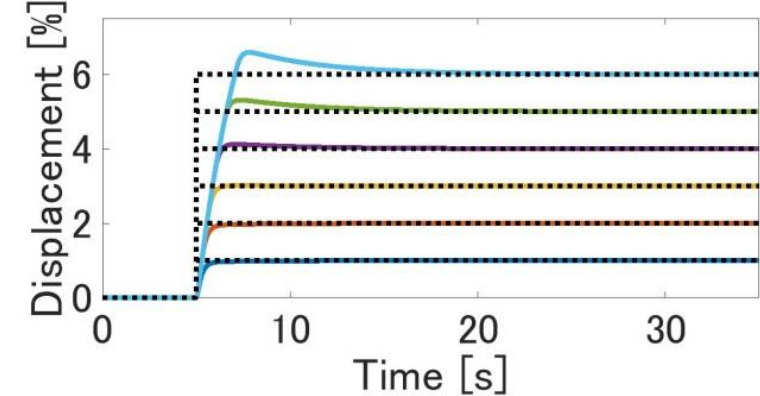


(c) Control signals from the PI controller (dotted) and saturated signals (solid)

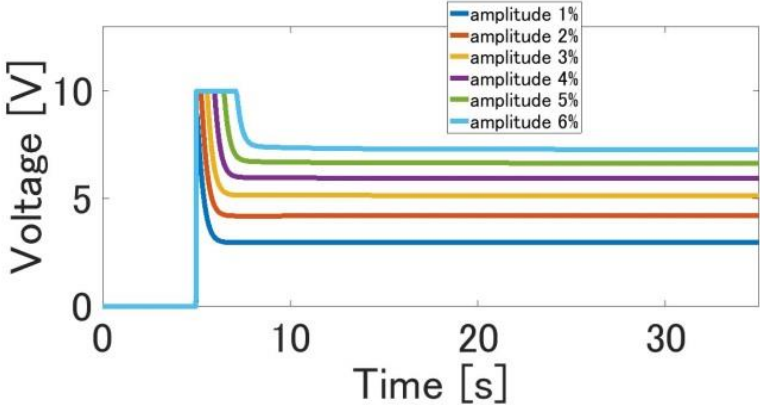
**Figure 15.** Simulation result of the PI-AW control (pulse reference signals)

Next, to verify the detailed effect of the anti-windup compensator, the reference signals are set as step signals with several amplitudes from 1 % to 6 %. The simulation results of the PI control without the anti-windup compensator are shown in Figure 16. Although good control performance is achieved when the input saturation is small or zero, the overshoot and settling time increase with the increasing

the amplitude of the step reference signals and the input saturation. These behaviors are caused by the increase of the accumulated integral quantity of the tracking error, as the increase of the amplitude leads to the increase of the tracking error. When the tracking error becomes opposite in sign, the integral controller interferes the motion due to the integral quantity of the tracking error. Note that the differences in steady state values of the input voltages become smaller as the steady state values of the displacements increases. This feature is due to the square nonlinear property of Joule's law. On the other hand, the simulation results of the PI-AW control are shown in Figure 17. In case of the PI-AW control, the recovery time from input saturation becomes short and the overshoot is resolved by the effect of the anti-windup compensator. From these simulation results, we confirmed the effect of anti-windup compensator.

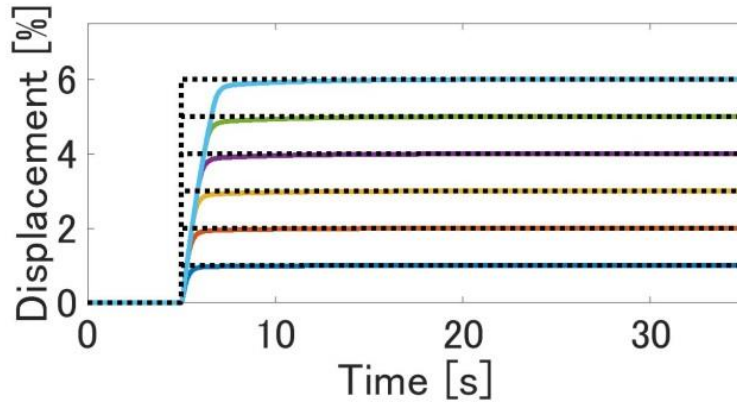


(a) Displacement (solid) and reference (dotted)

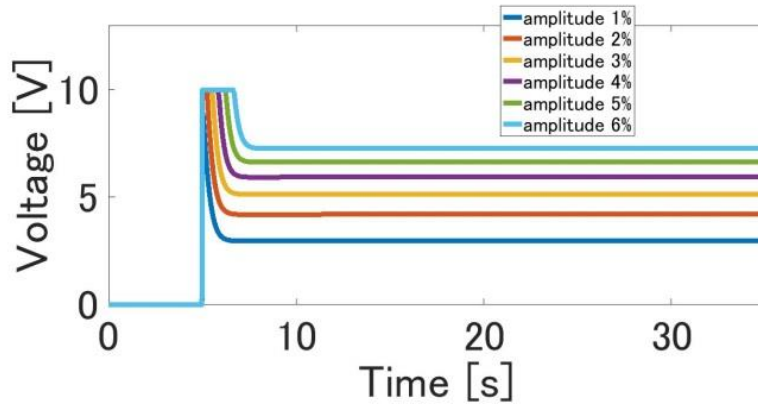


(b) Input voltage

**Figure 16.** Simulation result of the normal PI control (step reference signals)



(a) Displacement (solid) and reference (dotted)



(b) Input voltage

**Figure 17.** Simulation result of the PI-AW control (step reference signal)

### 3.2.3. Experiment verification of anti-windup compensator

The validity of the control system is investigated through experiments. The experimental conditions are set to be same as numerical simulations. In this section, we explain the experiment environment and experiment result.

A schematic diagram of our experimental environment is shown in Figure 18. In the environment, a real-time measurement and control system is implemented by using a digital signal processor (DSP) system (MTT, SBOX2). A control program is built in Matlab/Simulink and loaded to the DSP system. The control input signal is computed in DSP and applied to the power amplifier. The power amplifier outputs the driving voltage according to the control signal, and activates the actuator. The displacement of the actuator is measured by a laser displacement meter (KEYENCE, IA-100) and inputs to the DSP.

The sample time of the controller is set as 1 ms. The actuator is placed in a chamber (As-one). In this experiment, a temperature in the chamber is set as 23 °C. A weight of 20 g is attached to the actuator as same as the condition of the modeling experiment.

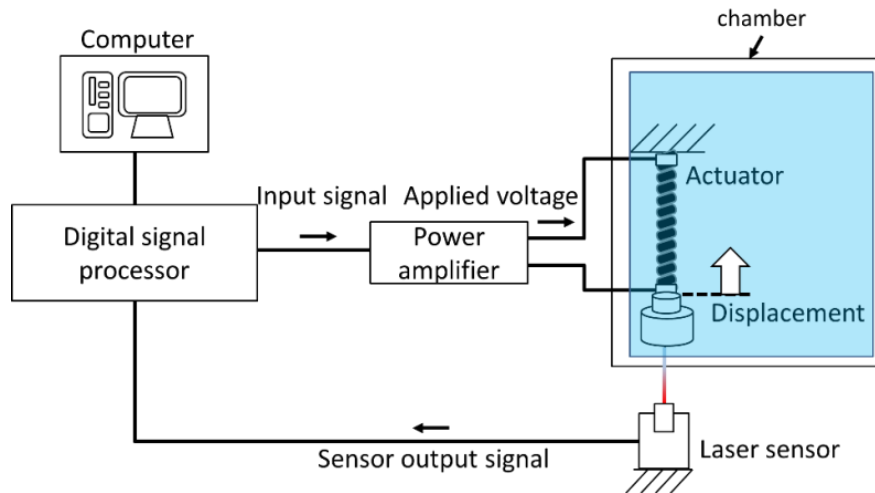
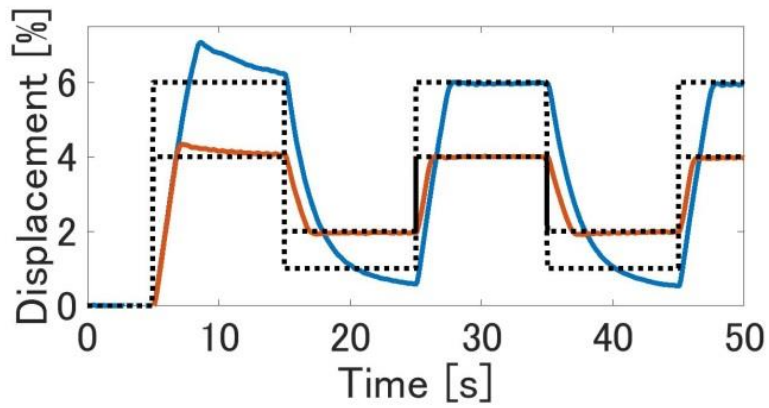


**Figure 18.** Experimental environment for AW control experiment

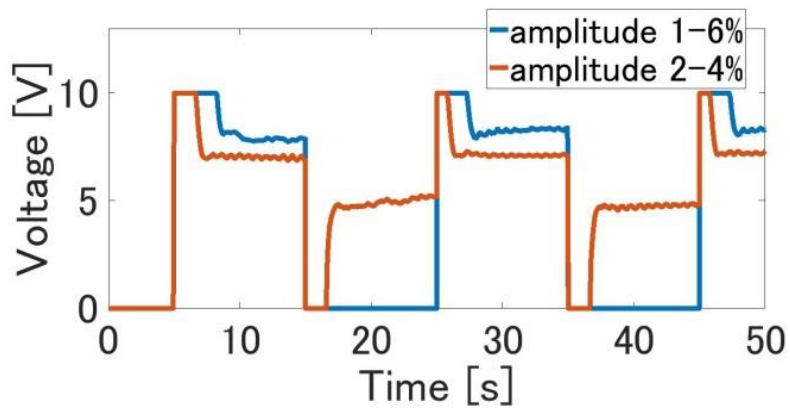
First, the reference signals are set as pulse waves from 1 % to 6 % and 2 % to 4 % to verify the validity of the anti-windup compensator for repetitive expansion and contraction motions as same as numerical simulations. Experiment results of the normal PI control without anti-windup compensator are shown in Figure 19. In the normal PI controller, in case of the relatively small range of motions, *i.e.* the reference signal from 2 % to 4 %, the overshoot is small since the integral quantity of the integral controller is relatively small. However, in case of the relatively large range of motions, *i.e.* the reference signal from 1 % to 6 %, the large overshoot arises due to the windup phenomenon, that is, the accumulated integral quantity of the tracking error becomes too large. In addition, the settling time becomes large since the recovery time from input saturation becomes large due to the integral quantity of the error, and the displacement does not converge to the reference in the stretch back motion. The experiment result indicated the windup phenomena lead to unwanted effects, as same as the simulation results. On the other hand, experimental results of the PI-AW control are shown in Figure 20. In both cases of different levels of the reference signals, the overshoot is kept small since the anti-windup compensator prevent accumulating the integral action when the control signal is saturated. In particular, compared to the normal PI control, the settling time becomes short and the overshoot becomes small in the reference signal from 1 % to 6 % as same as numerical simulation results. From Figure 20, it can be seen that the anti-windup compensator achieves appropriate control performance.

Next, to evaluate the effect of the PI-AW control, the reference signals are set as step signals with several amplitudes from 1 % to 6 % as same as numerical simulations. Experiment result is shown in Figure 21 and Figure 22, In case of the normal PI control shown in Figure 21, the overshoot and settling time increase with the increasing the amplitude of the step reference signals and the input saturation. On the other hand, in case of the PI-AW control shown in Figure 22, the recovery time from input saturation becomes short and the overshoot is resolved by the effect of the anti-windup compensator. Although minor differences between numerical simulations and experimental results exist caused by modeling errors and environmental disturbances, the experiments indicated the equivalent results with numerical simulations and the validity of the proposed method was confirmed.

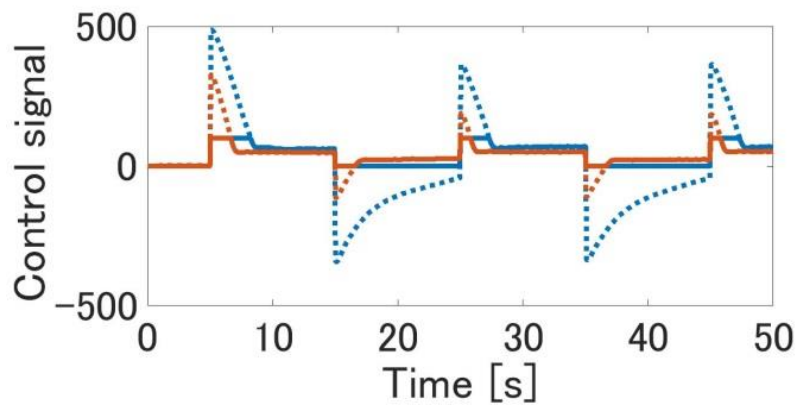
Figure 23 shows a maximum overshoot ratio in the experiments of Figure 21 and Figure 22, which is calculated by dividing the first overshoot by the amplitude of the reference signals in each experiment. These data in the figure are the average of measured experimental data for five trials. Although the normal PI controller achieves good control performance when the amplitude of the reference signal is small, the overshoot increase when the amplitude of the reference signal becomes large. On the other hand, the overshoot in the PI-AW control is almost nothing and good control performances are realized in every levels of reference signals. In particular, the maximum overshoot in case of 6% reference signal decreased from 14.799 % to 0.1024 % by applying anti-windup compensator. Furthermore, as with the numerical simulations, we confirmed the PI-AW controller is able to achieve good control performance for controlling the TCPA.



(a) Displacement (solid) and reference (dotted)

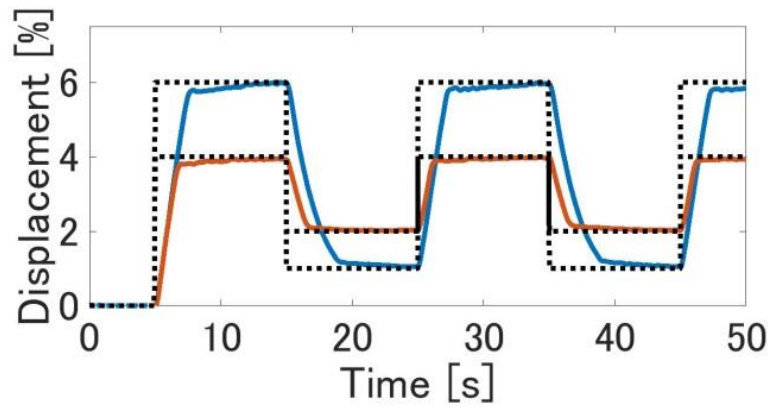


(b) Input voltage

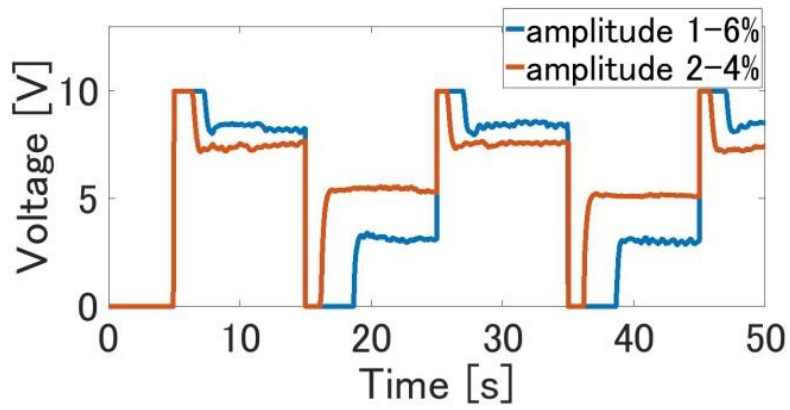


(c) Control signals from PI controller (dotted) and saturated signals (solid)

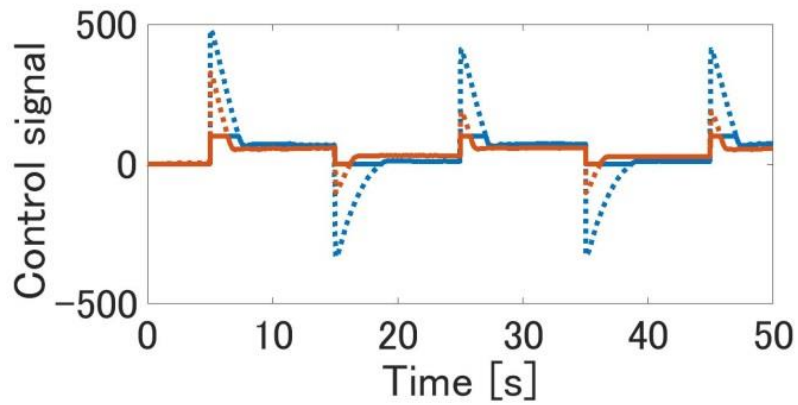
**Figure 19.** Experiment result of the normal PI control (pulse reference signals)



(a) Displacement (solid) and reference (dotted)

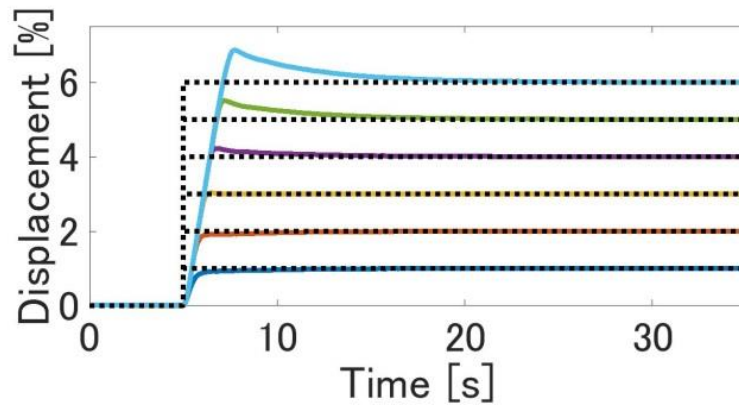


(b) Input voltage

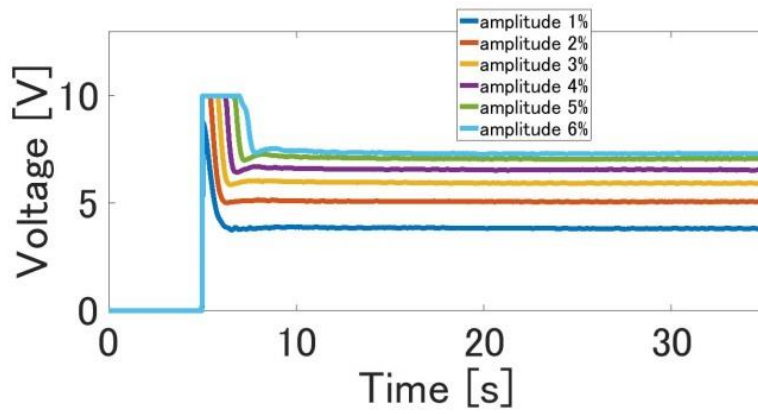


(c) Control signals from PI-AW controller (dotted) and saturated signals (solid)

**Figure 20.** Experiment result of the PI-AW control (pulse reference signals)

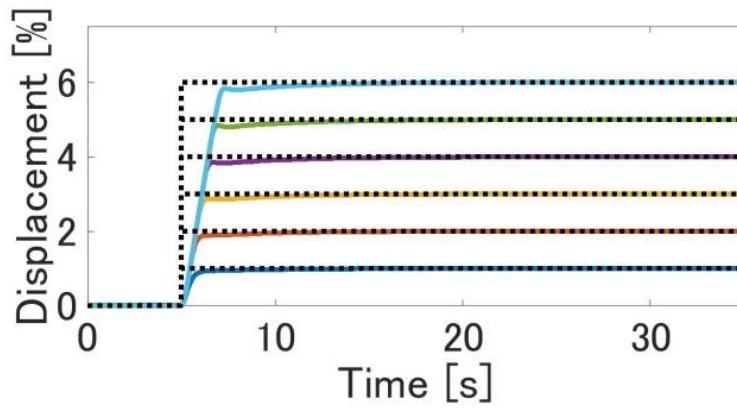


(a) Displacement (solid) and reference (dotted)

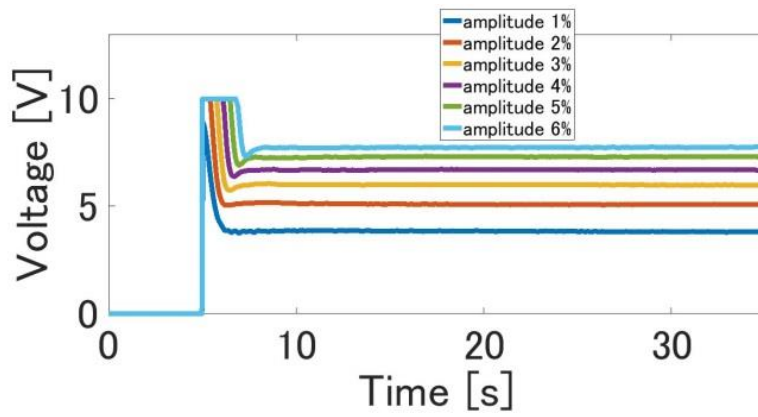


(b) Input voltage

**Figure 21.** Experiment result of the normal PI control (step reference signals)



(a) Displacement (solid) and reference (dotted)



(b) Input voltage

**Figure 22.** Experiment result of PI-AW control (step reference signals)

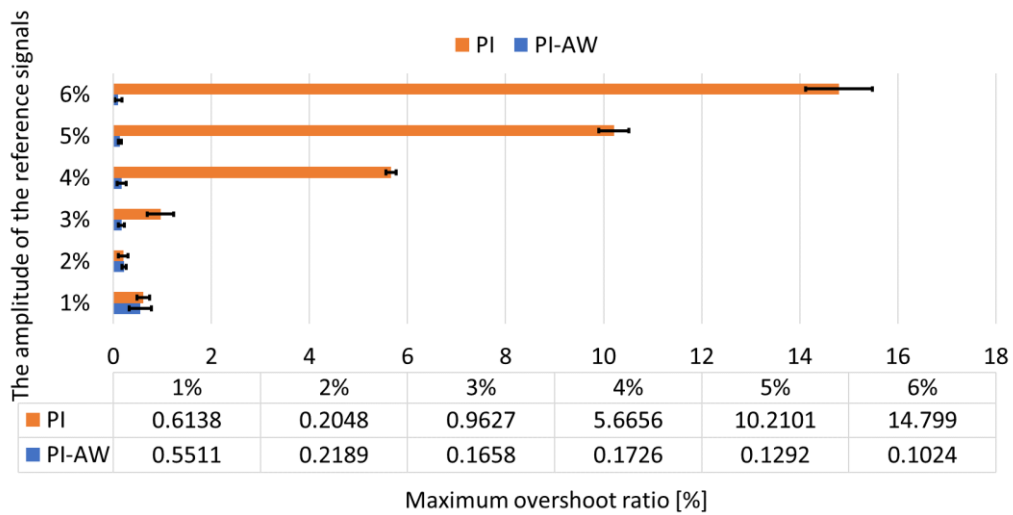


**Figure 23.** Maximum overshoot ratio in each experiment (n = 5, error means  $\pm$  SD)

### 3.3. Robust control for TCPA

To realize the control of the actuator, the linear PID control has been applied [20, 21, 34]. It has been reported that dynamics from the input voltage to the temperature or the displacement exhibit a nonlinear and hysteresis properties. In addition, the output response of the TCPA is influenced by unconsidered conditions such as an ambient wind speed [20], a fabrication method [23] and materials properties [5]. Therefore, the linear feedback control might not achieve good control performance. The feedback controller should be adjusted for good robustness and high tracking performance depending on the external disturbance, load weight fluctuation, actuation environment or reference signal. Furthermore, the control system design method should consider the gap between the nominal model and actual response. Although Luong *et al.* applied an adaptive PID sliding mode control to achieve high tracking and robust performance [24], the construction of the control system becomes quite complex. Therefore, simple and easy control system design methods are desired.

To solve this problem, a simple feedback controller with a disturbance observer was applied to the TCPA for realizing good robustness and high tracking performance. The control system performance was verified through numerical simulations and experiments.

#### 3.3.1. Controller design based on disturbance observer

In this section, a control system design method based on a disturbance observer for the electro-active TCPA is introduced.

For control system designs and numerical simulations, a model of the actuator is derived. Here, the nonlinear property from the input voltage to the electric power can be represented by Joule's law,

$$p(t) = \frac{v^2(t)}{R} \quad (17)$$

where  $R$  is electrical resistance,  $v(t)$  is the input voltage, and  $p(t)$  is the electric power. Although the electrical resistance varies slightly with the strain and temperature of the TCPA, the electrical resistance is considered to be constant. Based this assumption, the actuator is expressed as a system in Figure 24. The model consists of two sub-systems  $N$  and  $G$ , which are connected in series.  $N$  represents a nonlinear function as a square root function;

$$N(v) = v^2(t). \quad (18)$$

$G(s)$  represents dynamics from the squared input voltage  $v^2(t)$  to the displacement  $y(t)$ . Here,  $G(s)$  is assumed to be expressed as the LTI system;

$$G(s) = \frac{b_m s^m + b_{m-1} s^{m-1} + \dots + b_0}{s^n + a_{n-1} s^{n-1} + \dots + a_0} \quad (19)$$

where  $a_i$  ( $i=1,2,\dots$ ) and  $b_j$  ( $j=0,1,2,\dots$ ) are the parameters of the actuator model, and  $m$  and  $n$  are the order of the actuator model. These parameters of the dynamical model are identified by using experiment data based on system identification methods. In addition,  $n$  and  $m$  of  $G(s)$  are determined so that the modeling accuracy becomes as high as possible by system identification experiments from low-order to high-order. Because we apply the black box modeling and system identification method based on the experimental data, it is necessary to re-identify the model for every TCPA with different specifications. However, the identification method used in the paper is commonly applied in control system designs and is effective because of its simplicity for applications.

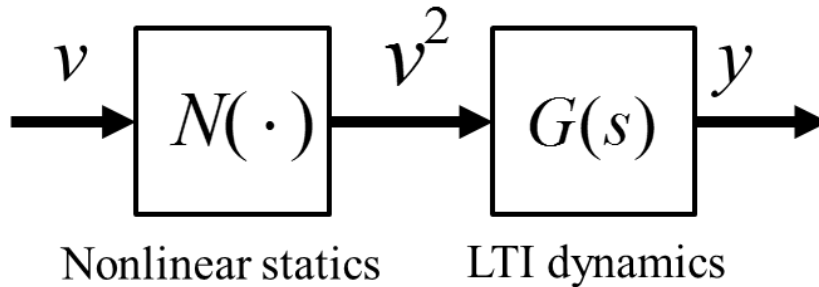


**Figure 24.** Actuator model from voltage to displacement

We explain feedback control system methods for electro-active TCPAs. The block diagram of the control system is shown in Figure 25. The control system consists of an inverse static nonlinearity  $N^{-1}$ , a feedback controller  $C$ , and a disturbance observer.

First, the feedback controller  $C$  considering dynamics  $G(s)$  is designed. In the actuator properties, the nonlinear statics of the square function of the input exists. By applying the inverse static nonlinearity  $N^{-1}$ , the feedback controller  $C$  is able to be designed simply with linear control theory. Hence, the inverse compensator  $N^{-1}$  is implemented by the square root function  $N$ ;

$$v(t) = \sqrt{u(t)} \quad (20)$$

where  $u(t)$  is the control signal calculated by the controller and  $v(t)$  is the input voltage. By insertion into the compensation of equation (20) after the feedback controller  $C$ , the control system can be designed by using linear control theory. Although any feedback controller can be applied, in this research, the feedback controller  $C$  is given as a conventional simple PI controller;

$$u_{FB}(t) = K_p \left( e(t) + \frac{1}{T_I} \int^t e(\tau) d\tau \right) \quad (21)$$

where the control signal  $u_{FB}(t)$  is the control signal from the feedback controller  $C$ ,  $K_p$  is a proportional gain and  $T_I$  is an integral time. These controller parameters are determined using the pole assign method based on the dynamics  $G(s)$ .

Next, the input voltage is limited within riskless driving voltage to avoid breaking of the actuator by overheating. In addition, the minimum input voltage is set because a negative input is unrealizable because of the joule's heating property. Therefore, the control signal  $u(t)$  is given as

$$u(t) = \begin{cases} u_{\max} & (u_{\max} < u_c(t)) \\ u_c(t) & (u_{\min} \leq u_c(t) \leq u_{\max}) \\ u_{\min} & (u_c(t) < u_{\min}) \end{cases} \quad (22)$$

where  $u_{\max}$  and  $u_{\min}$  are limits of the control signal, which are the square value of limited input voltage, and  $u_c$  is the control signal of the controller. In our control system, the range of input saturation is determined by trial actuation in preliminary experiments.

Finally, the disturbance observer is designed by using the dynamical model  $G(s)$ . To eliminate the influence of unconsidered factors such as a disturbance, hysteresis property, nonlinear property, or parameter variation, it is necessary to measure these influences and derive the detailed actuator model based on physical phenomena; however, these factors cannot be directly measured. In the control system, these unconsidered factors are estimated as an input disturbance  $d(t)$  by using the nominal model  $G(s)$ . In this study, the disturbance observer of Srivildiz and Ohnishi [37] is applied to the TCPA. It is assumed that the nominal model of the actuator from input  $u=v^2$  to output  $y$  can be expressed as a LTI model  $G(s)=y(s)/u(s)$ . The input disturbance  $d$  is assumed to be expressed as a deviation between an estimated input and an actual input  $u(t)$

$$d(s) = \{G^{-1}(s)y(s) - u(s)\} \quad (23)$$

where  $G^{-1}(s)$  is the inverse actuator model. However, the input disturbance  $d$  cannot be calculated by using input and output data because equation (23) is non-proper. Here, the estimated disturbance is

$$\hat{d}(s) = Q(s)d(s) \quad (24)$$

where  $Q(s)$  is a low-pass filter. The estimated disturbance needs to satisfy the follow condition:

$$\lim_{t \rightarrow \infty} \{\hat{d}(t) - d(t)\} = 0. \quad (25)$$

Therefore, the conditions of the  $Q(s)$  are

- 1) DC gain of  $Q(s)$  is  $Q(0)=1$ ,
- 2)  $Q(s)G^{-1}(s)$  is strictly proper or proper.

By combining (24) and (25), the estimated disturbance is

$$\hat{d}(s) = \{Q(s)G^{-1}(s)y(s) - Q(s)u(s)\}. \quad (26)$$

The control input to the actuator is applied as the summation of control signal  $u_{FB}(t)$  from the feedback controller and the estimated disturbance;

$$u_c(t) = u_{FB}(t) - \hat{d}(t). \quad (27)$$

Therefore, the actuator output  $y(t)$  is

$$y(s) = G(s)\{d(s) - \hat{d}(s) + u_{FB}(s)\}. \quad (28)$$

Therefore, the influence of the input disturbance  $d(t)$  can be eliminated by the feedback of the estimation disturbance.

Compared with other robust control methods, this method makes the control system configuration relatively simple, and a response similar to the nominal model is realized.

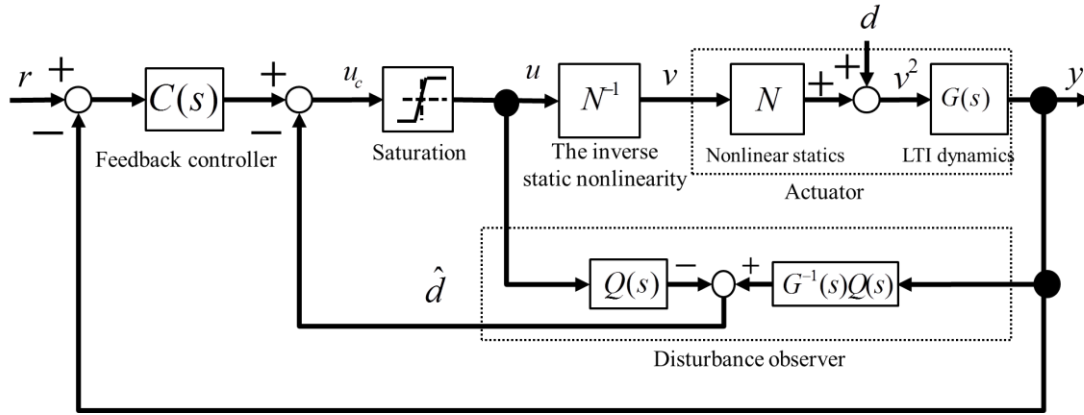


**Figure 25.** Block diagram of feedback control system with disturbance observer

### 3.3.2. Numerical simulation of disturbance observer

The validity of the disturbance observer was investigated through numerical simulations. In this section, we explain simulation methods and simulation results. To conduct numerical simulations, the model of the actuator was identified from preliminary experiment data. In the experiment, the TCPA was fabricated out of the silver coated nylon thread (Mitufuji, 100/3 ×3) The length of the TCPA was approximately 100 mm. The maximum strain was 10 % when the applied voltage was 10 V.

First, we identified the actuator model by using experimental data. For model identification, the input-output data with persistent excitation such as M-sequence and sweep signals are typically suitable. However, in the application of the TCPA, model identification by using the pulse response was fully effective [20, 21] and simply realized. In the simulation, to verify the robustness of the control system against environmental variation, the actuator was driven in two different environments; 1) standing air at room temperature, and 2) forced air at room temperature. The wind speed in the forced air experiment was 1.5 m/s. The room temperature was set as 23 °C. A pulse voltage of 6 V was applied and the displacement was measured with a laser displacement meter (KEYENCE: IA-100). In this experiment, a 50 g weight was attached to the actuator.

.  $G(s)$  is assumed to be expressed as the first order system:

$$G(s) = \frac{b}{s + a} \quad (29)$$

For parameter identifications, a discrete-time state space model of the actuator was identified by using N4SID function of MATLAB. The parameter of the transfer function  $G(s)$  was derived by discrete-continuous conversion method with the zero-order hold. The model parameters in standing air were identified as  $a=0.1399$  and  $b=0.09062$  and the fitting ratio was 85.17 %. In case of the forced cooling air, the parameters were identified as  $a=0.3248$  and  $b=0.07245$  and the fitting ratio was 89.05 %. Identification results are shown in Figure 26. The simulation results agree well with the experimental result.

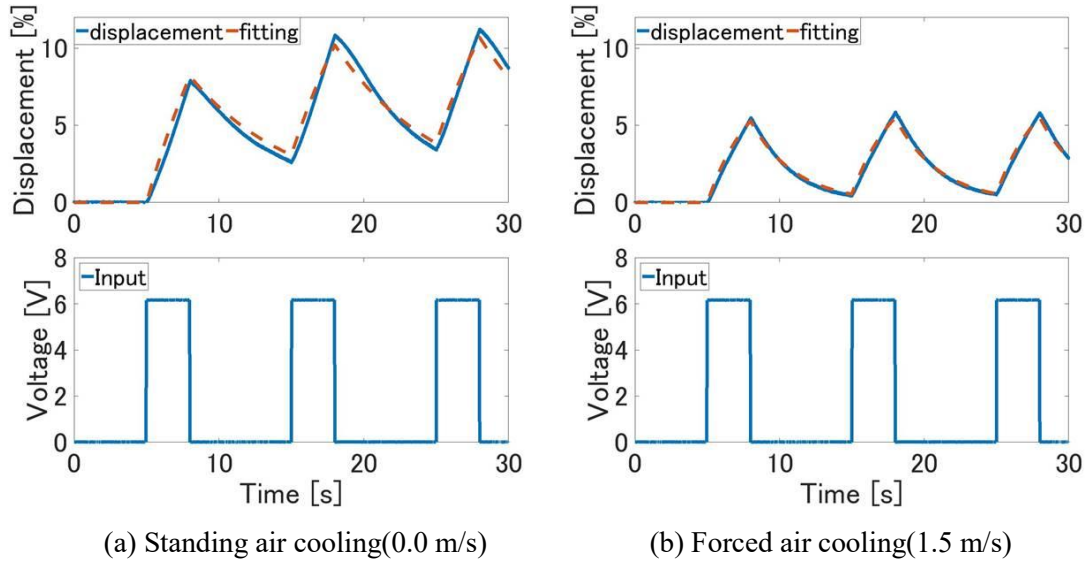


**Figure 26.** Identification result of the dynamics from voltage to displacement

Next, we explain the simulation method. The numerical simulations were conducted by using MATLAB/Simulink. In our numerical simulation, an ordinary differential equation was solved by using the Ode45function of MATLAB. The low-pass filter was set as a first order filter

$$Q(s) = \frac{1}{T_c s + 1} \quad (30)$$

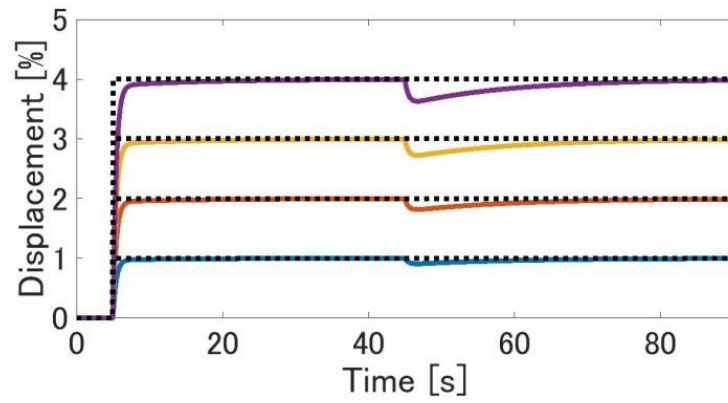
where  $T_c$  was a time constant. The input saturation was set as  $u_{max}=100 \text{ V}^2$  and  $u_{min}=0 \text{ V}^2$ , that is, the maximum and minimum voltage were 10 V and 0 V, respectively. In the simulation, to verify the performance of the disturbance observer against the environmental variation, the parameters of the model were changed from standing air cooling to forced air cooling at 45s, that is, the wind speed was varied. The reference signal was a step signal with several amplitudes from 1 % to 4 %.

In the simulation, the controller parameter were determined as  $K_p=25$  and  $T_f=12.5$  by the pole placement method so that the overshoot did not arise and the closed loop system became stable. The

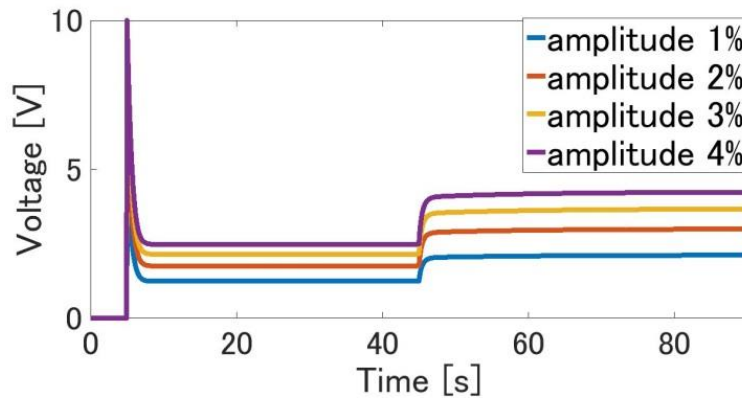
sampling time was set to 0.001 s and the time constant of the filter  $T_c$  was set to 0.1 s. In the simulation, we compared the simulation result of a normal feedback control and the feedback control with the disturbance observer to verify the validity of the disturbance observer.

The simulation results of the normal feedback control are shown in Figure 27. In the figure, the dotted lines are reference signals and the solid lines are experimental data. From 0 to 45 s, each displacement converged to the reference signals and the overshoot did not arise. Therefore, good control performance could be realized when the model parameters were not varied. However, from 45 to 90 s, a large tracking error arose when the model parameters were varied from the standing cooling air to the forced cooling air. Although each displacement converged to the reference signal as time passed, the convergence time was quite long. It is possible that this large tracking error could be removed by adjusting the control parameter to a high gain. However, in a wide actuation range, the high gain feedback control might lead to an unwanted influence such as an increase of the overshoot, a decrease of control accuracy because of input saturation, or an increase of a noise.

The simulation results of the feedback control with the disturbance observer are shown in Figure 28. From 0 to 45 s, the estimated disturbance was computed as 0 because the model parameter was not varied. Therefore, good control performance was realized as same as the simulation result of normal feedback control. However, from 45 to 90 s, each displacement converged to the reference signal even when the model parameters were varied. The large estimated disturbance was computed by the variation of the model parameter after 45 s. In addition, the rise of the input voltage at 45 s became fast compared with the normal feedback control. The tracking error decreased compared with the normal feedback control, because the influence of variation of the model parameter was removed by the feedback of the estimated disturbance. These simulation results show that robust and high tracking control result can be realized with the effect of the disturbance observer.

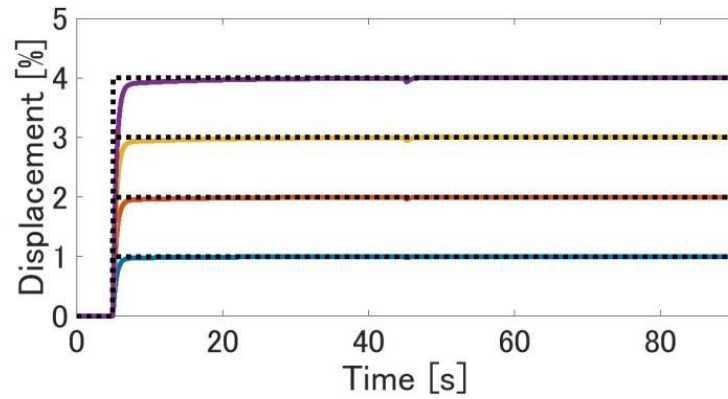


(a) Displacement (the solid line) and reference (the dotted line)

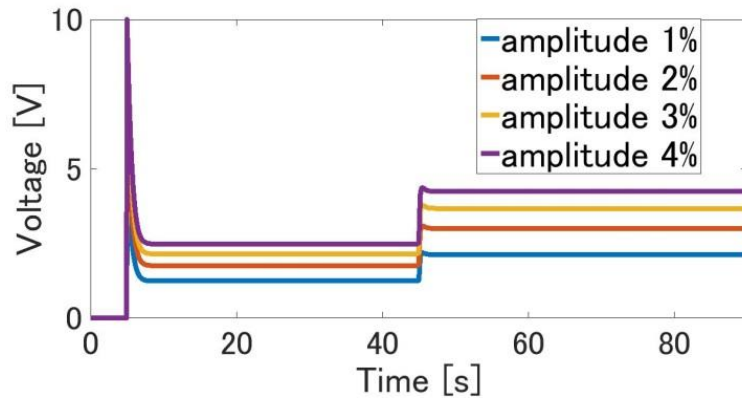


(b) Input voltage

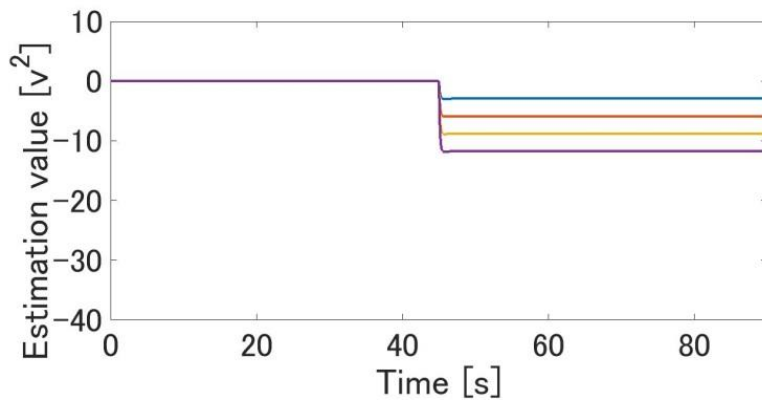
**Figure 27.** Simulation result of feedback control without the disturbance observer



(a) Displacement (the solid line) and reference (the dotted line)



(b) Input voltage



(c) Estimated disturbance

**Figure 28.** Simulation result of feedback control with disturbance observer

### 3.3.3. Experiment verification of disturbance observer

The validity of the control system was investigated through experiments. The experimental conditions were the same as in the numerical simulations. We explain the experiment environment and results.

A schematic diagram of the experimental environment is shown in Figure 29. In the environment, the control input signals are calculated by using the displacement and reference signal measured by a digital signal processor (MTT, SBOX2). The control signal from the computer was applied to the power amplifier, which could output the input voltage according to control signals. The displacement of the actuator was measured by a laser displacement meter (KEYENCE, IA-100). The control programs of the digital signal processor were implemented by using MATLAB/Simulink. The sample time of the controller was set as 0.001 s. In addition, to verify the robustness of the control system against an environmental variation, the wind speed of the environment was varied in the numerical simulations. The wind speed was varied from 0.0 to 1.5 m/s by using a DC fan motor at 45 s. The cooling system was only used for causing the environmental variation. In this experiment, the room temperature was set as 23 °C and a 50 g weight was attached to the actuator. The displacement of the actuator is measured by a laser displacement meter (KEYENCE, IA-100).

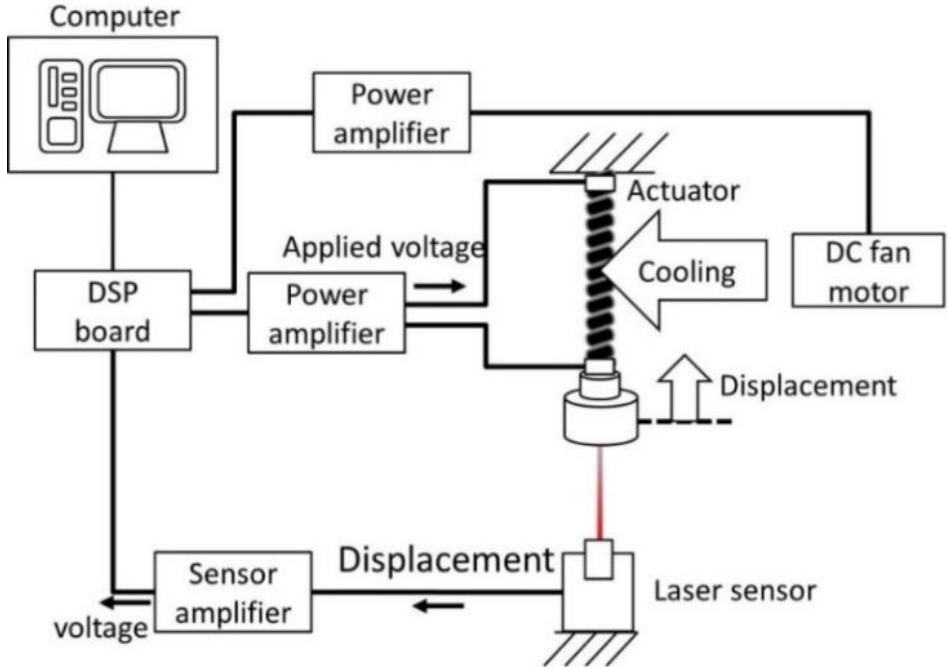
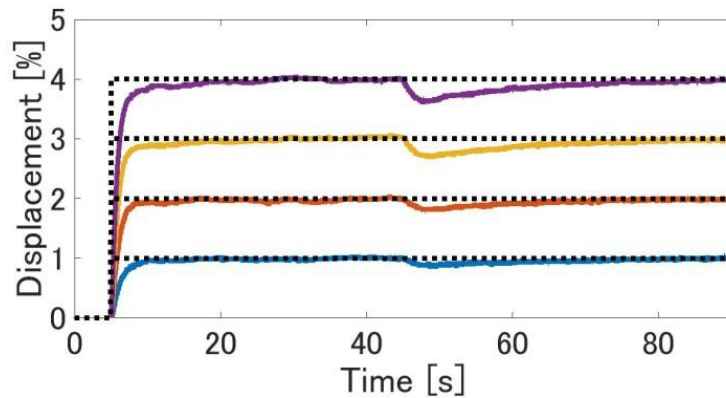


**Figure 29.** Experiment system for verification of disturbance observer

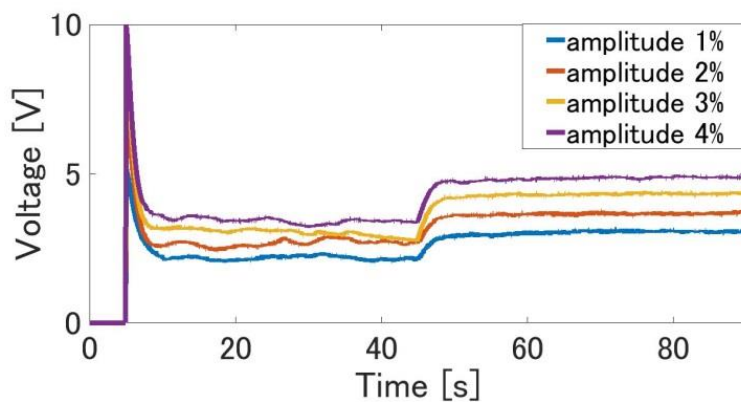
Experimental results of normal feedback control are shown in Figure 30. From 0 to 45 s, each displacement converged to the reference signals and the overshoots did not arise, the same as in the numerical simulation results. From 45 s to 90 s, although each displacement converged to the reference signal as time passed, the convergence time was relatively long, as in the numerical simulation results. The large tracking error arose because of the variation of the environment from the standing air to the

forced air. Although minor differences between numerical simulations and experimental results occurred, caused by modelling errors and environmental disturbances, the results were the same as in the numerical simulation.

Experimental results of the feedback control with the disturbance observer are shown in Figure 31. From 0 to 45 s, each displacement converged to the reference signals. From 45 to 90 s, the large tracking error decreased compared with the normal feedback control, because the influence of disturbance was removed by the disturbance observer. These experiments showed that the good control performance can be realized, even when the environment is varied as in the numerical simulations. Furthermore, from about 5 to 8 s, a large estimated disturbance was computed because of the deviation between the actual response and the model of the actuator. The transient response improved because of the feedback of this large estimated disturbance compared with normal feedback control. Although the input voltage became noisy, the control performance close to the numerical simulation was realized even when compared with normal feedback control. These experiment results show that the disturbance observer can realize good, robust control results.

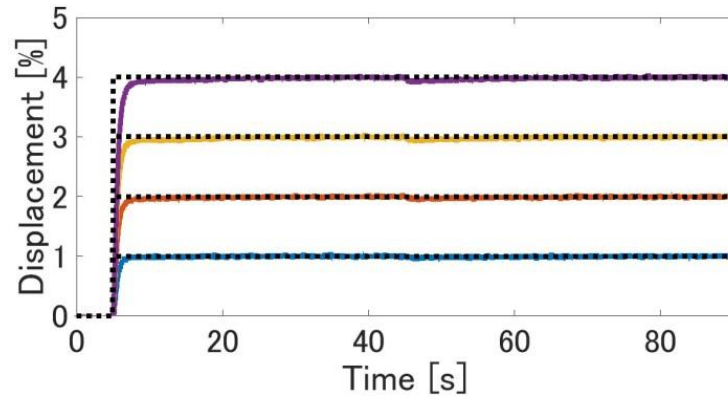


(a) Displacement (the solid line) and reference (the dotted line)

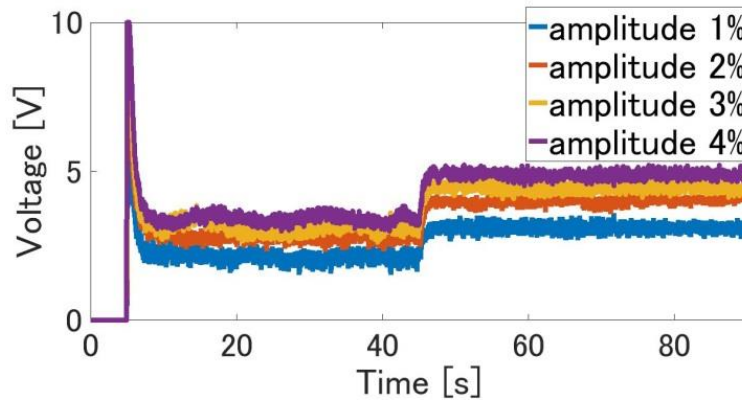


(b) Input voltage

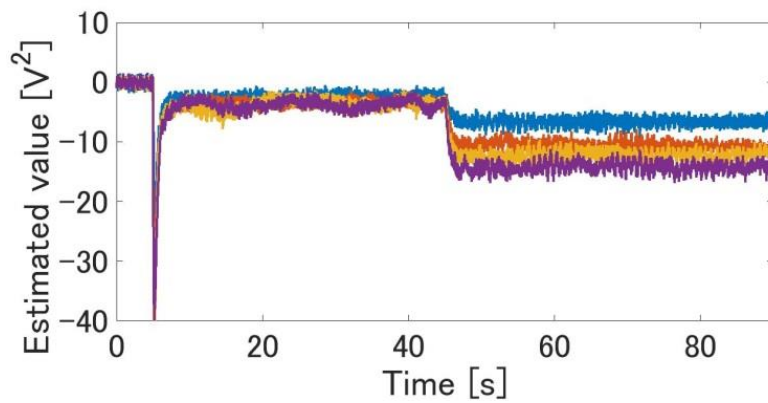
**Figure 30.** Experiment result of the normal feedback control



(a) Displacement (the solid line) and reference (the dotted line)



(b) Input voltage



(c) Estimated disturbance

**Figure 31.** Experimental result of feedback control with disturbance observer

To evaluate the control performance in the experiment, the root mean square error (RMSE) of the tracking error which is an index of tracking performance, was computed using experimental data from 45 to 90 s. The RMSE is defined as

$$RMSE = \sqrt{\frac{1}{L} \sum_{i=0}^{T_{sim}} (r(i) - y(i))^2} \quad (31)$$

where  $r(i)$  and  $y(i)$  are the reference signal and actual output data at time  $i$ , and  $L$  is number of the output data. The RMSE from the experiments is shown in Figure 32. The data in the figure are the average of measured experimental data for five trials. The results show that the tracking error of normal feedback control increased as the amplitude of the reference signal increased. However, the tracking error of the feedback control with the disturbance observer decreased considerably in each experiment compared to the normal feedback control. These results show that the disturbance observer can eliminate the influence of unconsidered factors and realize robust control results.

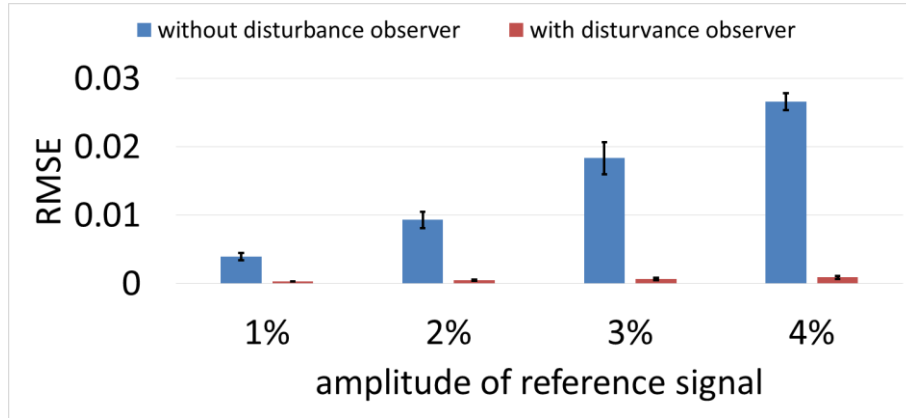


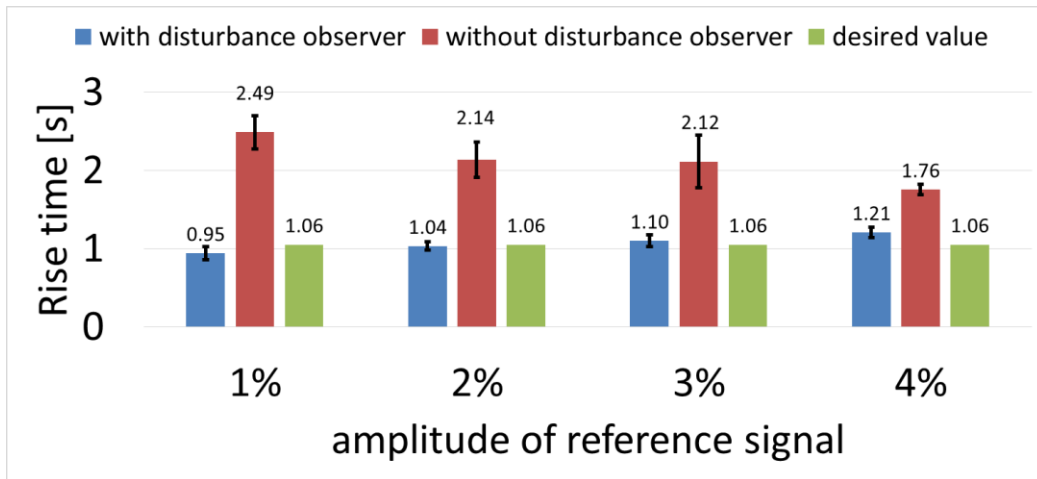
**Figure 32.** Comparison of RMSE in experiments results (n=5, error means  $\pm$  SD)

To evaluate the control performance in terms of nominal errors, the rise time and the settling time, which are a general evaluation metrics for evaluating feedback control performance at the transient response [38], were calculated by using experimental data from 5 to 45 s. The settling time is the time required for reaching the reference signal. In this research, the settling time was calculated as the time reaching within 10 % of the reference signal. The rise time is the time in which the actuator output  $y(t)$  rises from 10% to 90% of the steady-state response. If the rise time and the settling time are close to the response of the nominal model, the control system is considered to realize robust control performance.

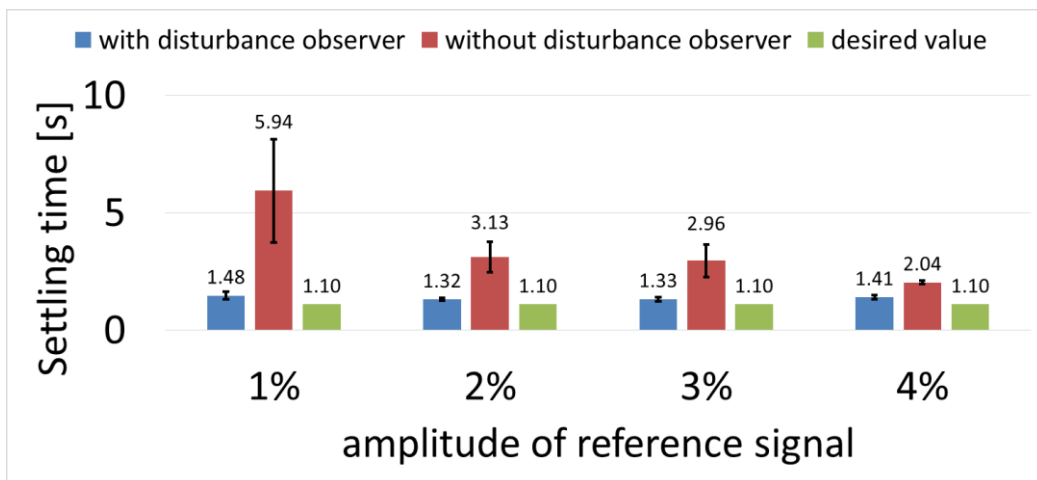
The rise time and the settling time for the experiment results are shown in Figure 33. The experimental data in these figures is the average of measured data for five trials. The desired value is the simulation result based on the nominal model. In the case of normal feedback control, as the amplitude of the reference signal decreases, the differences between the experimental result and the desired value increases. The nominal model only agrees well with the response property at approximately 4% of the

displacement. As observed in Figure 33, the normal feedback control cannot achieve an appropriate control result in a relatively wide actuation range.

However, in case of feedback control with the disturbance observer, although a minor difference exists between the desired value and the experiment value, the transient response is improved by the disturbance observer. In each experiment, the settling time and rise time became closer to the simulation result. The gap caused by the nominal error decreased because of the effect of the feedback of the estimated disturbance of the nominal error. As shown in the results, robust control performance can realize in wide actuation range.



(a) Rise time



(b) Settling time

**Figure 33.** Comparison of the experiment results (n=5, error means  $\pm$  SD)

### 3.4. Simple controller design based on internal model control method

These researches indicate that the PID control can realize high tracking and robust performance if the controller gains are tuned adequately. However, tuning of the appropriate PID gains is difficult. Although various auto-tuning methods were reported as Ziegler-Nichols method, CHR method and optimization based an evaluation function [39], the PID gains to realize the desired response need to be determined by trial and errors of preliminary experiments. From these problems, more simple control method for stabilizing the control system of the TCPA and realizing the desired response is desired.

To solve these problems, the control system design method called as an internal model control is applied. This controller structure is simple and can be designed easily without experience in parameter-tuning based on controls theory. The internal model control consists of the feedforward controller and feedback controller based on the model. The control system can realize high tracking performance, and the desired response of the TCPA is obtained due to a feedforward control signal and a feedback of estimated disturbances. In this section, the control system performance is verified through experiments.

#### 3.4.1. Controller design based on internal model control method

We explain control system design methods for the TCPA. To design the controller based on the model, a gray-box modeling is applied. In addition, the internal model control method is introduced

For control system design, the model of the TCPA consists of two sub-systems: nonlinear statics  $N$  and LTI dynamics  $G_D$ , which are connected in series.  $N$  is expressed as a square function;

$$N(\cdot) = v^2 \quad (32)$$

The transfer function of the linear dynamics  $G_D(s)$  from the squared input voltage  $v^2(t)$  to the displacement  $y(t)$  is expressed as a third order transfer function;

$$G_D(s) = \frac{b_0}{s^3 + a_2s^2 + a_1s + a_0} \quad (33)$$

The block diagram of the control system is shown in Figure 34. The control system consists of an inverse compensator of static nonlinearity  $N^{-1}$ , a feedforward controller  $G_C$  and a nominal model  $G_D$ .

First, the inverse compensator  $N^{-1}$  for canceling the nonlinearity of the Joule's law is implemented by the square root function;

$$v(t) = \sqrt{u(t)} \quad (34)$$

where  $u(t)$  is the control signal calculated by the controller and  $v(t)$  is the input voltage. By inserting the series compensation of the equation (34) after the controller  $G_c$ , the control system can be designed by linear control theory.

To avoid breaking of the actuator by overheating, the maximum input voltage is limited within risk-less driving voltage. The maximum input voltage is set so that the actuator isn't overheated nor does not reach to displacement limitations of the coil-coil contact. In addition, the minimum input voltage also is limited since the negative control signal is unrealized in normal voltage driving. Therefore, the saturated control signal  $u(t)$  is given as

$$u(t) = \begin{cases} u_{\max} & (u_{\max} < u_c(t)) \\ u_c(t) & (u_{\min} \leq u_c(t) \leq u_{\max}) \\ u_{\min} & (u_c(t) < u_{\min}) \end{cases} \quad (35)$$

where  $u_{\max}$  and  $u_{\min}$  are limit of the square value of input voltage and  $u_c$  is the control signal of the controller  $G_c$ . Note that the saturation  $u_{\max}$  is determined by the preliminary experiment, and  $u_{\min}$  is set to zero.

The internal model control based on the LTI dynamical model is designed as same with the reference of [40]. The arbitrary reference model can be applied under the condition of minimum phase system. In this paper, for simplification of the controller design, the reference model  $F(s)$  is given as a conventional low-pass filter;

$$F(s) = \frac{1}{(\lambda s + 1)^3} \quad (36)$$

where  $\lambda$  is a time constant. Here, the time constant  $\lambda$  is adjusted so that the controller can realize the desired response from the reference signal to the output. Note that the reference model is expressed as the third-order transfer function so that the controller  $G_D(s)$  becomes proper.

Next, to cancel the linear dynamics  $G_D(s)$ , the controller  $G_C(s)$  from the reference signal to the control signal is given as the inverse model of linear dynamics;

$$G_C(s) = F(s)G_D^{-1}(s) \quad (37)$$

Note that  $G_D(s)$  is assumed to have the stable poles and zeros. If the modeling error and any disturbance don't exist, the response from the reference signal to the output becomes the desired response based on the reference  $F(s)$  since the controller  $G_C(s)$  balances the poles and zeros of the linear dynamics. However, the output is not able to track under the conditions with the unconsidered factor such as nonlinear property, disturbances and nominal error in actual environments. Therefore, the mechanism considering these factors is needed.

The feedback mechanism compensating the influence of the modeling error and some disturbance is designed. Here, the deviation  $e_M$  between the actuator output and the estimated output of the model is expressed as

$$e_M(s) = y(s) - G_D(s)u(s) \quad (38)$$

To compensate  $e_M$ , the control signal  $u_c$  is given as

$$u_c(s) = G_C(s)\{r(s) - e_M(s)\} \quad (39)$$

where  $r$  is a reference signal. By applying above control method, the response from the reference signal to the output is equal to the desired response of the reference model  $F(s)$  since the  $e_M$  is eliminated due to the feedback compensation.

The internal model control has following advantages:

1. It is extremely simple to design the control system since the control system can be implemented by only adjusting the reference model if the model of the TCPA can be derived.
2. This control method can realize the good control performance close to the desired feedforward control where the modeling error and some disturbance don't exist.
3. The internal stability of the control system is guaranteed since the LTI physical model of the TCPA doesn't have the unstable zeros and poles.

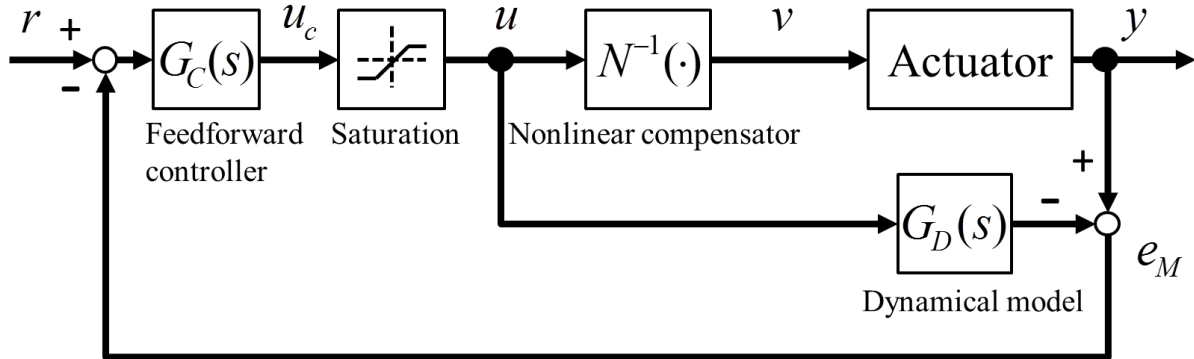


**Figure 34.** The block of diagram internal model control system

### 3.4.2. Experimental environmental and system identification

The validity of the control system is investigated through experiments. In this section, we explain the experimental environment, the system identification results and experiment result.

The electro-active TCPA used in the experiments was fabricated by the silver-plated Nylon thread (AGposs 100/2, Mitsufuji). The Nylon thread in uncoiled state is 300 mm length and 0.1 mm diameter. The Nylon thread in coiled state is 85 mm length and 0.4 mm diameter after over-twisting. The configuration of the actuator is 100 mm length and 0.3 mm diameter. The electric resistance is  $74.2 \Omega$  in unloaded condition. The length of the actuator is 100 mm. When a 20 g weight is attached to the end of the actuator, the maximum strain of the actuator is about 10 % by 10 V.

A schematic diagram of our experimental environment is shown in Figure 35. In the environment, a real-time measurement and control system is implemented by using a digital signal processor system (MTT, SBOX2). A control program is built in MATLAB/Simulink and loaded to the digital signal processor system. The control input signal is computed in digital signal processor and applied to the power amplifier. The power amplifier outputs the driving voltage according to the control signal. The output displacement of the actuator is measured by a laser displacement meter (KEYENCE, IA-100) and the displacement data is input to the digital signal processor. The displacement is defined as shrinkage ratio [%] of the initial length of the actuator. The sample time of the controller is set as 1 ms. The actuator is placed in a chamber (As-one). In the experimental environment, a temperature in the chamber is set as  $23 \text{ }^\circ\text{C}$  and a weight of 20 g is attached to the actuator.

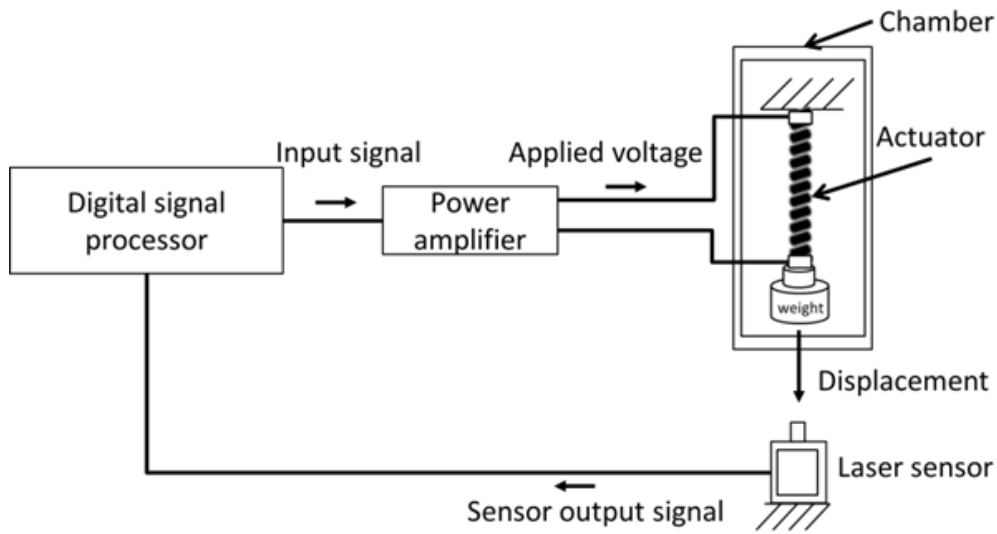
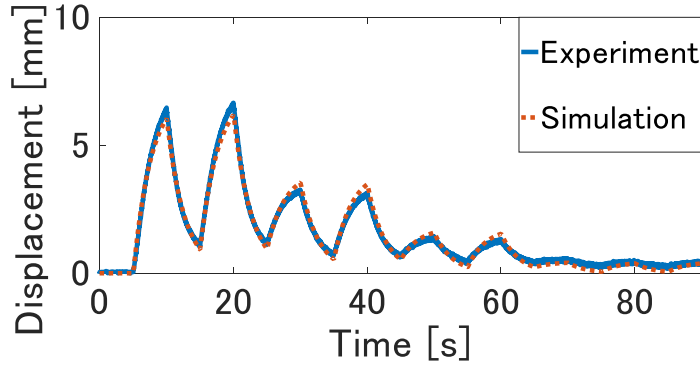


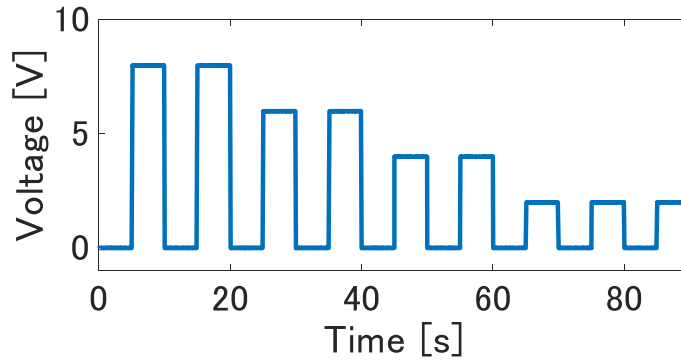
**Figure 35.** Experiment environment for internal model control

In this section, we explain the identification method of the dynamical model. The model parameters were derived using input-output data of the experiments. In the experiment, the input voltage-output displacement of pulse response with multilevel amplitudes was measured. For parameter identification, a discrete-time state space model of the actuator is identified by using N4SID function of MATLAB. The parameter of the transfer function  $G_D(s)$  is derived by using discrete-continuous conversion method with zero-order hold.

By using a system identification toolbox of MATLAB, the model parameters are identified as  $a_2=371.1$ ,  $a_1=1003$ ,  $a_0=44.09$  and  $b_0=42.09$ . Identification results are shown in Figure 36. In this figure, the experimental data and simulation result of the identified model are plotted. The fitting ratio is 89.25 %. The simulation results agree well with the experimental result.



(a) Displacement



(b) Input voltage

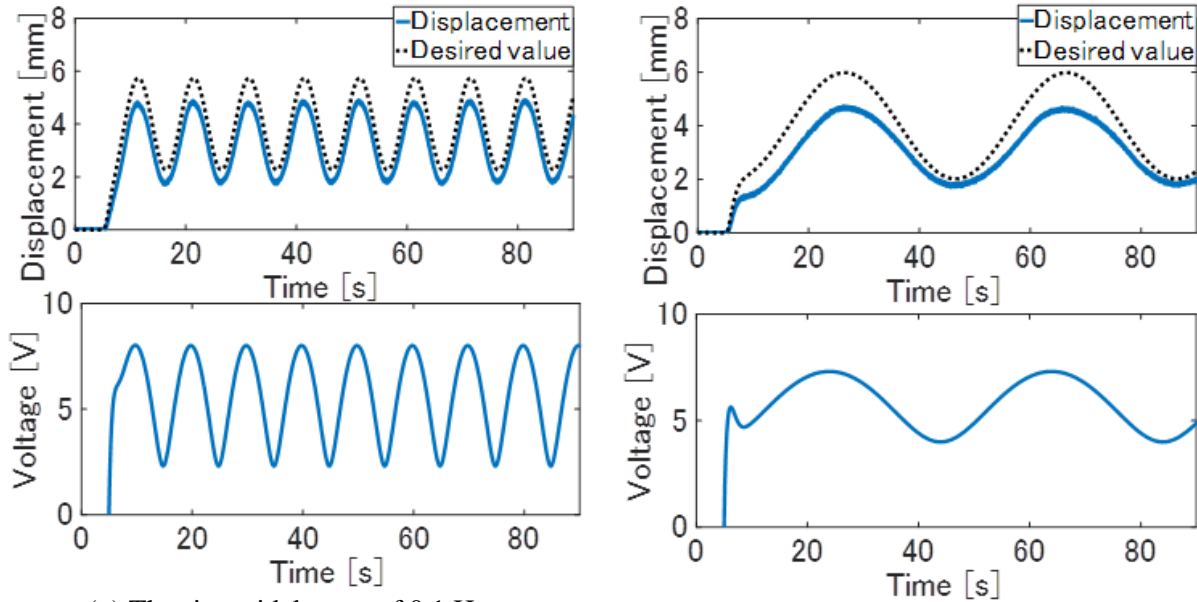
**Figure 36.** Identification results of the actuator model

### 3.4.3. Experimental verification of internal model control

The validity of the internal model control is investigated as the controller can balance the actuator properties adequately and realizes the desired response. The reference signals are set as sinusoidal waves with the frequency of 0.1 Hz and 0.025 Hz and the peak value from 2 mm to 6 mm. The reference signal is set as the composite wave with the sinusoidal waves of 0.1 Hz and 0.025 Hz. The time constant  $\lambda$  is set to 0.5 s as the control signal is not saturated. To verify the validity of the proposed control system, the experiment result of the internal model control is compared to the conventional feedforward control based on the LTI model. In the conventional feedforward control, the control signals  $u_c$  is given as  $u_c = G_c(s)r(s)$ .

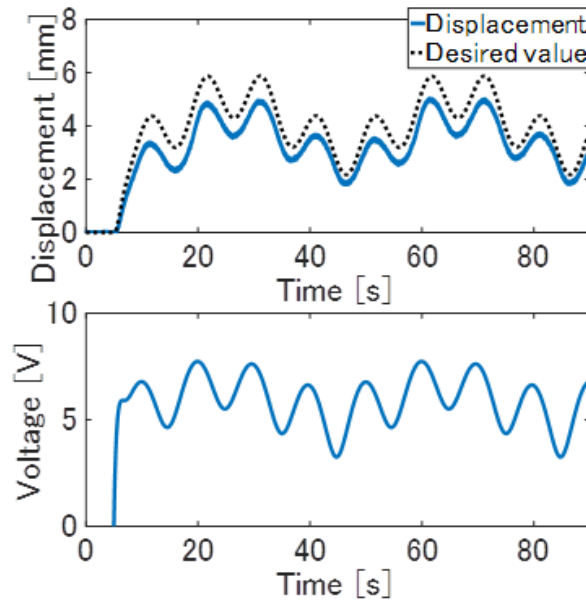
Experiment results of the feedforward control are shown in Figure 37. In this Figure, the solid line is the displacement of the TCPA and the dotted line is a desired value, that is, the reference signal after passing through the reference model  $F(s)$ . From Figure 37 (a) and (b), although the displacement is varied along to the reference signal, the large tracking error between the displacement and the desired value arises. From Figure 37 (c), the large tracking error arises as same with the result of the sinusoidal wave of 0.1 Hz and 0.025 Hz. This tracking error is considered to arise due to the unconsidered

factors such as nonlinear thermal conductivity [30], mechanical property [31], noise, the parameter variation due to the temperature dependence and the coil-coil contact and so on. Furthermore, these parameters might be varied due to the coil-coil contact.so on. Therefore, the feedforward control based on LTI model cannot realize the desired response.



(a) The sinusoidal wave of 0.1 Hz

(b) The sinusoidal wave of 0.025 Hz

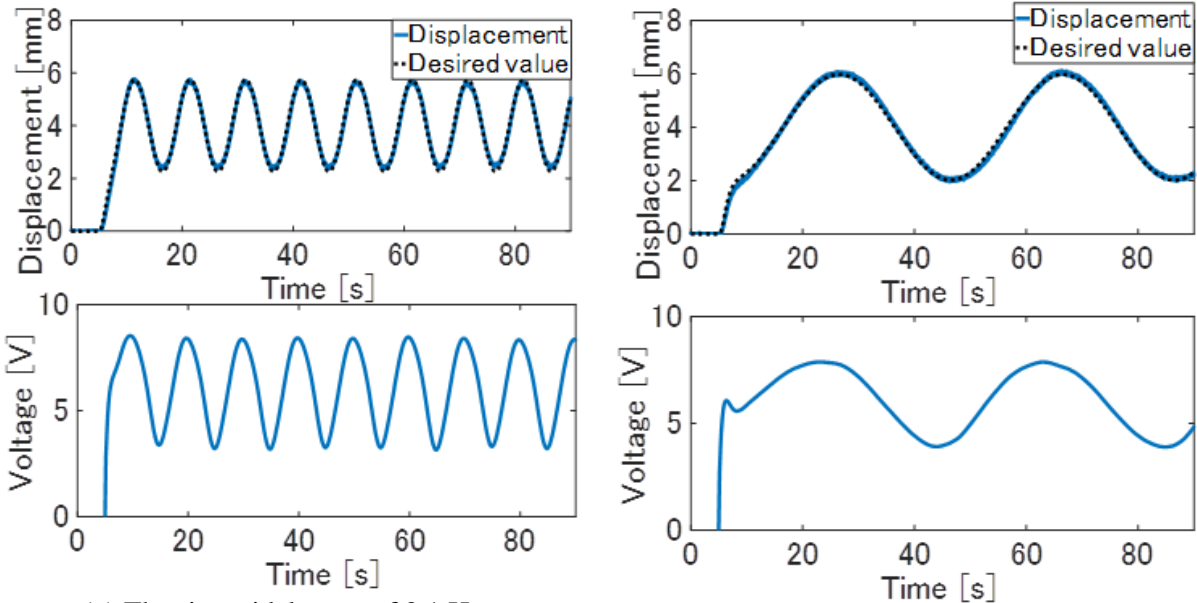


(c) The composite wave with the sinusoidal wave of 0.1 Hz and 0.025 Hz

**Figure 37.** Experiment result of the feedforward control with the sinusoidal wave

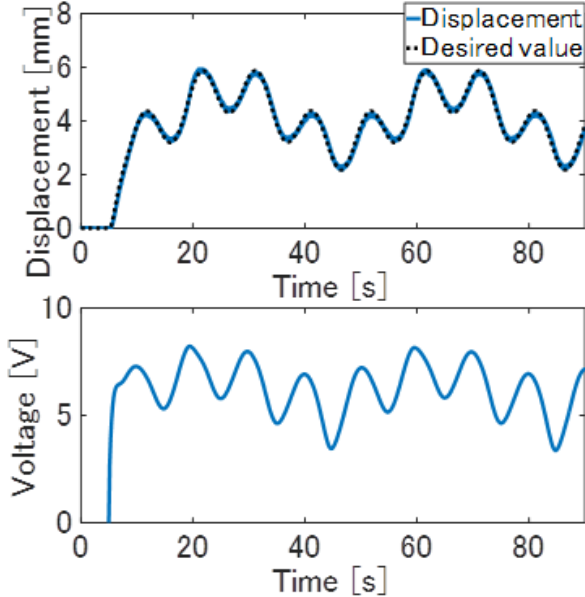
Experiment results of the internal model control are shown in Figure 38. In each control results, the large error decreased and the displacement of the actuator can be tracked to the desired value com-

pared to the feedforward control. As observed in the results, the desired control performance can be realized due to the feedback of deviation between the actual output and the estimated output of the nominal model. In the experiment, the displacement control can be realized in the same response performance for other amplitude and frequency of the target signal if the input voltages are within the upper limitation of the input saturation. Therefore, as shown in the results, the internal model control can eliminate of the nominal error and disturbance, realize and the desired control performance.



(a) The sinusoidal wave of 0.1 Hz

(b) The sinusoidal wave of 0.025 Hz



(c) The composite wave of 0.1 Hz and 0.025 Hz

**Figure 38.** Experiment result of the proposed control method with the sinusoidal wave

To further investigate the control performance of the internal model control, the reference signals are set as the step wave with multilevel amplitude. Experiment results of the conventional feedforward control are shown in Figure 39. In each experiment result of the step wave, the large steady state error between the displacement and the desired value arises. This steady state error is considered due to the modeling error and disturbances. This tracking error is considered to arise due to the unconsidered factors such nominal errors and disturbance. Therefore, the feedforward control based on LTI model cannot realize the desired response.

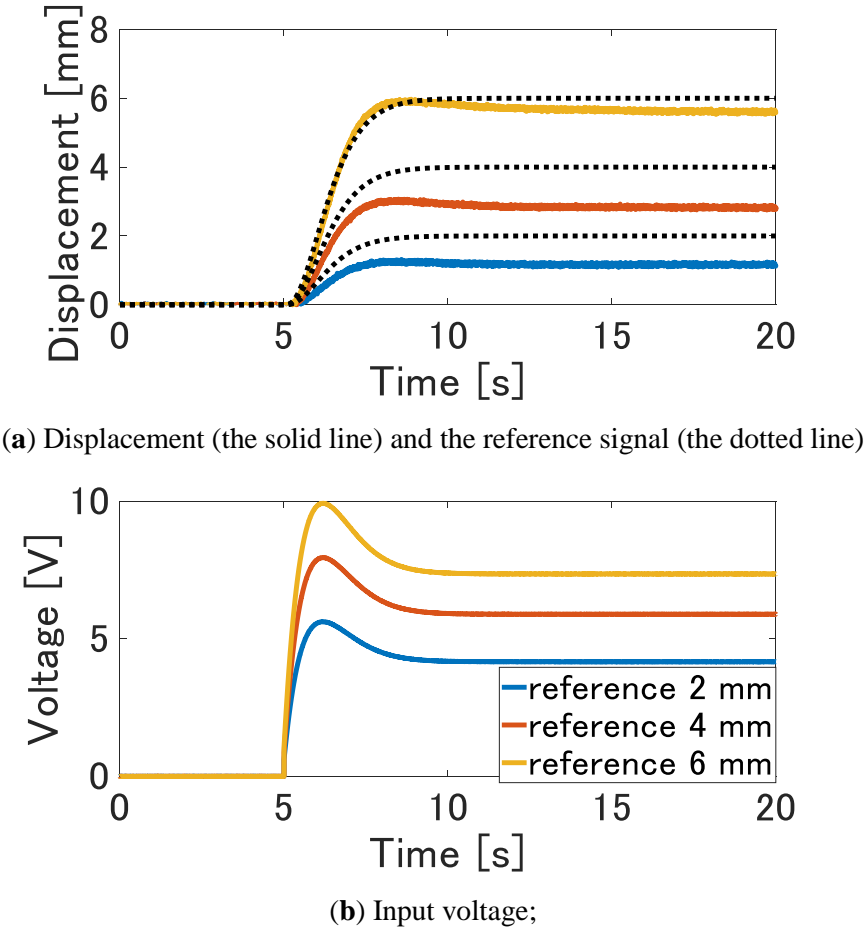
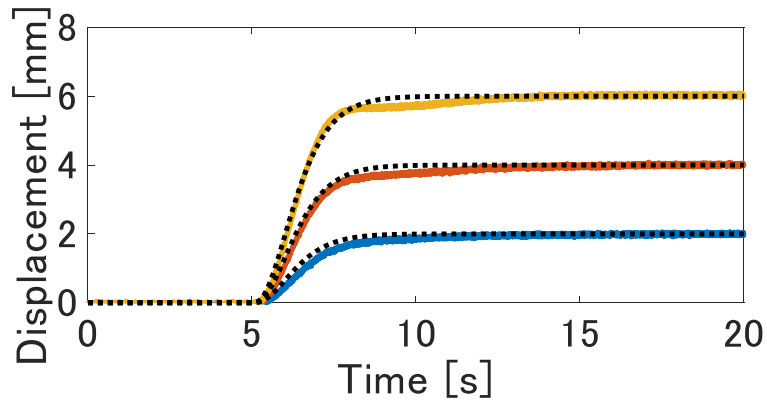


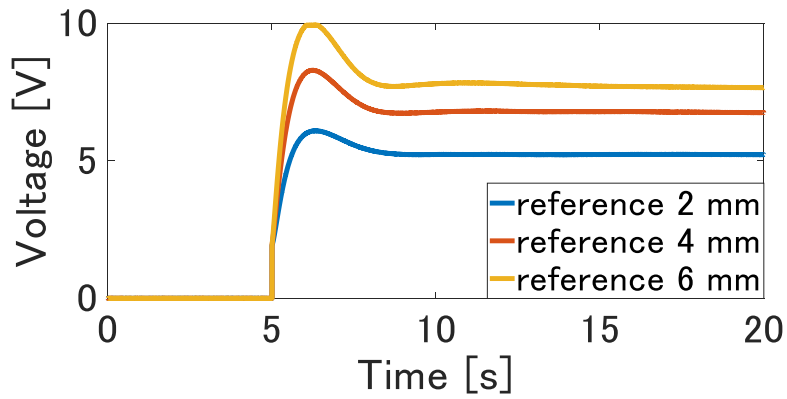
**Figure 39.** Experiment result of the conventional feedforward control of step response

Experiment results of the internal model control are shown in Figure 40. In each experiment result, the overshoot doesn't arise, and the displacement can be tracked to the desired value. Although quite small errors between the displacement and the desired value arise in the transient response, the steady state errors are eliminated due to the feedback of the internal model. The displacement is able to be tracked to the desired value since the control signal is adequately adjusted due to the feedback of the output error. From these results, the nominal error and disturbances can be eliminated due to the inter-

nal model feedback. As also shown in these results, the internal model control can balance the actuator properties adequately and realize the desired control performance.



(a) Displacement (the solid line) and the reference signal (the dotted line)



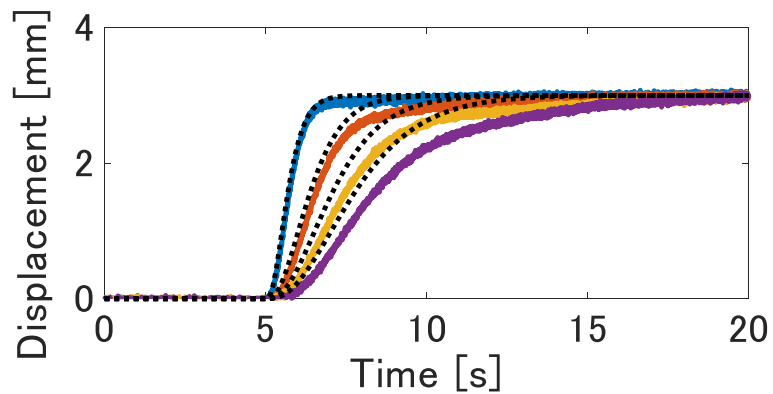
(b) Input voltage

**Figure 40.** Experiment result of the internal model control in step response

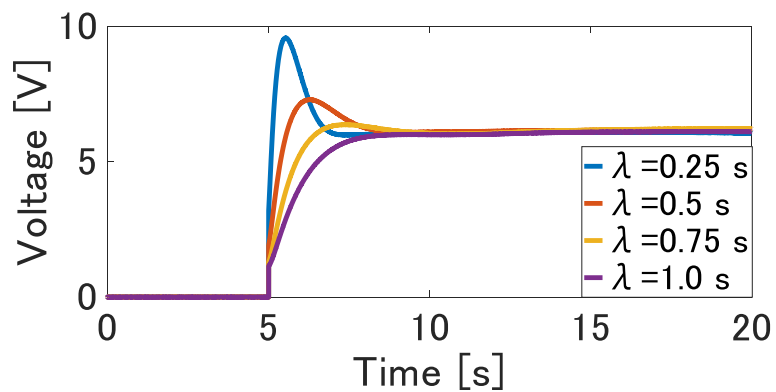
We verified that the proposed control method can realize the desired control performance. Here, as with the method of the reference of Yip and Niemeyer [20], the rise time is recorded when the pole of the reference model is varied. In the experiment, the time constant  $\lambda$  is changed from 0.25 s to 1 s per 0.25 s. Note that the pole is a reciprocal of the time constant  $\lambda$ . The reference signal is the step wave with amplitude of 3 mm. These parameters are determined so that the control input is not saturated to evaluate the dependence of the time constant.

Experiment results are shown in Figure 41. In this figure, the solid line is the measured displacement and the dotted line is the desired value. In each result, the displacement converges the reference signals. The response speed is higher as the time constant is smaller. On the other hand, as the time constant is larger, the response speed from the reference signal to the displacement is slower. Furthermore, the tracking error between the desired value and the displacement increases as the time constant

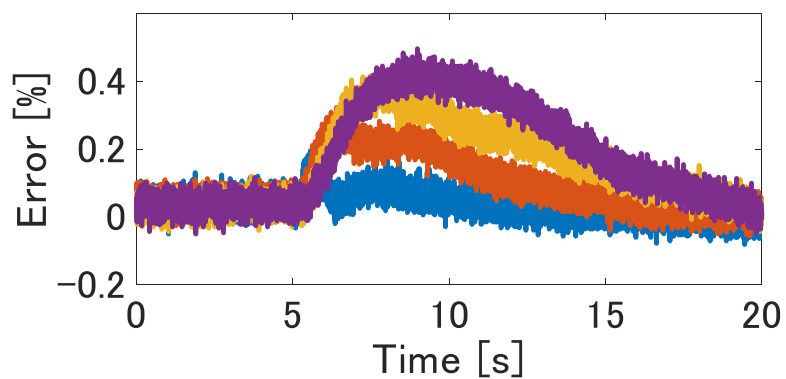
is larger, that is, the tracking performance is higher as the pole is larger. This is considered to arise due to small gain theorem which is trade-off between the control performance and stability [41]. From Figure 41 (d), it is observed that the rise time increases due to the increase of the time constant. As shown in result, the response from the reference signal to displacement depends on the time constant of the reference model. Therefore, the desired control performance can be realized by adjusting the pole of the reference model.



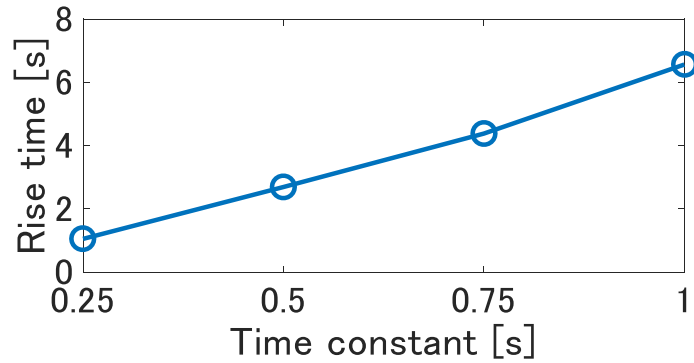
(a) Displacement (solid line) and the desired value (dotted line)



(b) Input voltage



(c) Tracking error between the displacement and the desired value



(d) Rise time vs time constant:

**Figure 41.** The response property due to the variation of the time constant  $\lambda$

### 3.5. Summary

In this chapter, the control system design for applications was proposed. In particular, to solve problems such as joule heating, input saturation, nominal error and parameter-tuning, the control system was applied to the actuator. The validity of the control system design was investigated through numerical simulations and experiments. The anti-windup compensator was applied to the single TCPA. Compared to the conventional PI control, the precision of the displacement control was improved. In addition, the robustness of the control against parameter-variations was realized by applying the disturbance observer. Based on internal model control methods, the control system can be designed easily. Selecting from these control methods depending on the situation of the actuation, good control results is realized.

## 4. Application to robotic systems

In this chapter, we explain the demonstration of robotics system using the TCPA. We proposed antagonistic actuator, and applied the actuator to robot-arms.

### 4.1. Introduction of robotic system with TCPA

For applying the TCPA to the application, the modeling and controller design had been performed. Based on these results, the robot-arm with TCPA is demonstrated. However, the robot-arm using the single TCPA may not realize the good control performance because the TCPA is not suitable for being repeatedly expanded and contracted. A symmetric response characteristic due to asymmetric input property and the difference of heating cooling speeds remain a problem. In case of actuation by Joule heating, both of positive and negative voltage rise the actuator's temperature. The negative control input to cool the actuator cannot be applied, then the input voltage is set to 0 V and the actuator is cooled by heat dissipation. In addition, response speeds depend on environment and are different between heating and cooling [20]. Arakawa *et al* and Sutton *et al*. applied the feedback control to the TCPA with Joule heating [33, 34]. In case of the tracking to the pulse signals, a large error arises in stretch back motion due to the above problem. Therefore, the TCPA is not suitable for being repeatedly expanded and contracted. To solve this problem, Yip *et al*. analyze response characteristics of TCPA under forced air and develop robotic hand with cooling fan [20]. Arakawa *et al*. proposed PID control method with the cooling fan [34]. Although the Peltier device can apply negative energy for cooling, uniform cooling is difficult due to long and thin shape of the actuator. Therefore, the simple methods for application are desired.

To solve these problems, we proposed antagonistic-actuator. The antagonistic-actuator consists of two TCPA. By the effect of antagonistic-structure, expanding and contracting can be realized repeatedly. Applying the antagonistic actuator to the robot arm, good control performance of robot-arm is realized. In this chapter, the effect of antagonistic-structure and control system design is investigated through numerical simulation. Comparing the single actuator, the validity of the antagonistic-actuator is verified. Furthermore, the antagonistic-actuator is applied to the robot-arm for investigating validity of our control system. The feedback controller was selected depending on the actuation condition and properties of robot-arm. The control performance of the robot-arm with antagonistic-actuator was investigated through numerical simulation and experiments.

## 4.2. Antagonistic-actuator

In this section, we apply antagonistic-structure to the TCPA. The validity of the antagonistic-structure is verified through numerical simulation and experiments. Furthermore, the control performance was improved by applying PID control.

### 4.2.1. Modeling and control of antagonistic-type actuator

We explain an antagonistic-type actuator and control methods. Figure 42 shows a schematic overview of the antagonistic-type TCPA actuator, where two TCPA elements are arranged antagonistically. The normal length of each element is same. The position of a weight is set as an operating point, that is, an output of the actuator. Since negative inputs for extending cannot be applied, the expanding motion depends on natural cooling. By this structure, the antagonistic actuator can generate force in both expansion and construction directions. Therefore, the response in the expansion motion can be improved by the antagonistic action. The control input of the antagonistic-type actuator is divided into positive and negative and applied to each element.

Applying the antagonistic structure, the maximal generating force/displacement decreased compared to the single actuator. However, our method is easy to implement the compact and silent actuator devices compared to air-cooling systems [20][34].

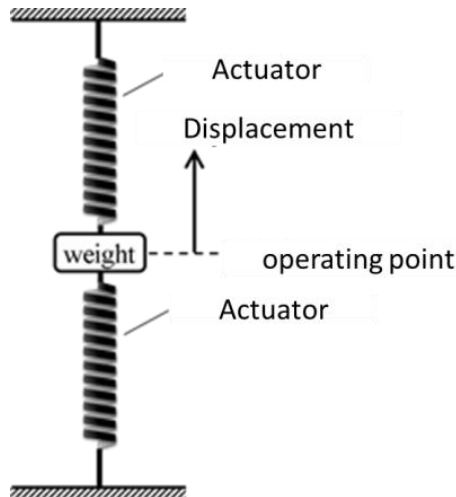


**Figure 42.** Antagonistic-type TCPA

Modelling and controller design methods are explained. Since a detailed physical model of the TCPA have not established, we apply a system identification based on a linear system model. A model for the actuator is assumed to be represented by a system in Figure 43. The model consists of two sub-systems  $G_{VF}$  and  $G_{FY}$ , which are connected in series.  $G_{VF}$  represents dynamics from the input voltage  $v$

to the generated force  $f_1$ .  $G_{FY}$  represents mechanical dynamics from the force  $f_2$  to the displacement of the actuator  $y$ . The force  $f_2$  is the difference between the generated force  $f_1$  and the external load  $f_l$ .

For control system design of the antagonistic-type TCPA, we need to identify  $G_{VF}$  and  $G_{FY}$ . In this paper,  $G_{VF}$  and  $G_{FY}$  are assumed to be linear time-invariant system, and are identified separately by using experimental input-output data. The identification procedures are as follows:

1. Identification of  $G_{VY}$

The model parameters of  $G_{VY} = G_{FY}G_{VF}$  are identified by using measurement data of responses from input voltage to output displacement.

2. Identification of  $G_{FY}$

The model parameters of  $G_{FY}$  are identified by using measurement data of responses from input force (load)  $f_l$  to output displacement.

3. Calculation of  $G_{VF}$

$G_{VF}$  is calculated as  $G_{VY} / G_{FY}$ .

In the procedures 1 and 2, the parameters are identified by using least-square methods, which are executed with the system identification tool in MATLAB. Since we apply the gray box modeling and the system identification method based on the experimental data, it needs to re-identify the model for every TCPA with different specifications. However, the identification method used in the paper is commonly applied in control system designs and effective due to simplicity for applications.

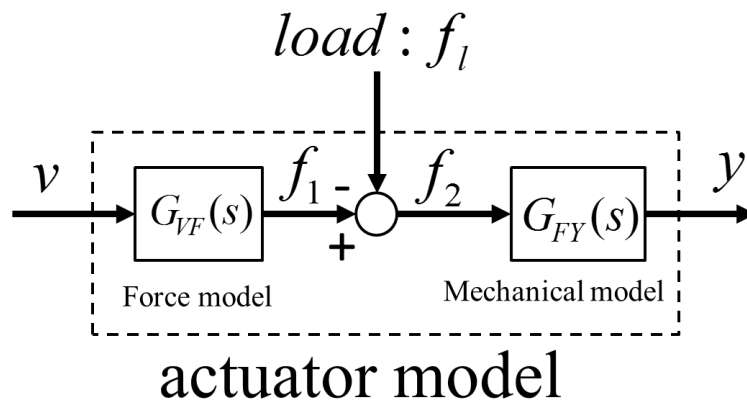


**Figure 43.** Block diagram of the TCPA's model

To investigate the validity of the antagonistic structure, simple feedback control methods are applied. Figure 44 shows a block diagram of the control system of the antagonistic-type TCPA actuator. In this figure, the actuator dynamics of the antagonistic-type actuator is expressed as the parallel force models and the whole mechanical model. The difference of the output forces from two force models is entered into the mechanical model. The mechanical model is expressed as a combined dynamics of the two actuator elements with the antagonistic structure. The mechanical model's parameters of the antagonistic-type actuator is assumed to be half as large as the values of the parameters of the single actuator. Then, the stiffness of antagonistic actuator model becomes equivalent to double of that of the single actuator model.  $C(s)$  is a feedback controller,  $e$  is an error signal which is the difference between an output displacement  $y$  and a reference signal  $r$ .  $u$  is a control signal by the feedback controller  $C(s)$ .

In this control system, the feedback control signal  $u$  is dividing into positive and negative signals and these signals are applied to each actuator element. In addition, to avoid breaking of the actuator element by overheating, the input voltages are limited within riskless driving voltage. Therefore, the input voltages  $v_1$  and  $v_2$  are given as

$$v_1(t) = \begin{cases} v_{\max} & (v_{\max} < u(t)) \\ u(t) & (0 \leq u(t) \leq v_{\max}) \\ 0 & (u(t) < 0) \end{cases} \quad (40)$$

$$v_2(t) = \begin{cases} 0 & (0 < u(t)) \\ -u(t) & (v_{\min} \leq u(t) \leq 0) \\ -v_{\min} & (u(t) < v_{\min}) \end{cases}$$

where  $v_{\max}$  and  $v_{\min}$  are limiting value of input voltage.

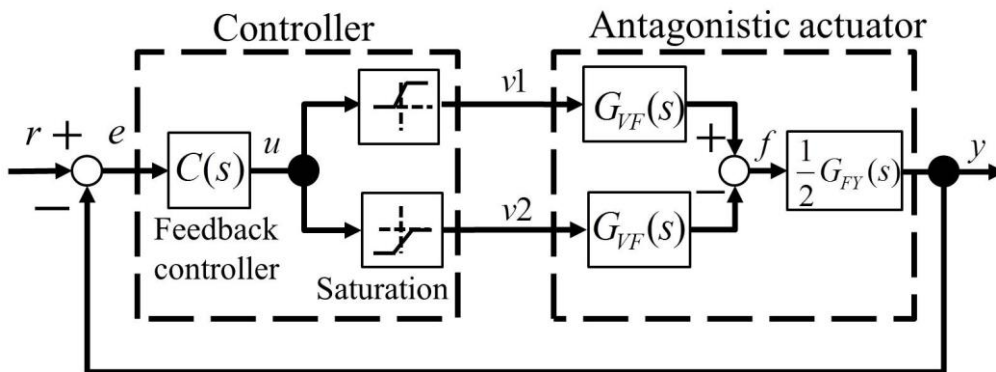


**Figure 44.** Control system design of antagonistic TCPA

### 4.2.2. Numerical simulation of the displacement control

We investigated the validity of the proposed method through numerical simulation. The model of the actuator is identified using experimental input-output data. For simulating antagonistic structure, the input voltage-force model and the force-displacement model are derived. In the experiment, room temperature was set as 23 °C. First, we identified the force-displacement model from response data of step load. In the experiment, a 50 g weight is attached to the end of the actuator and is dropped. The input force  $f_l$  is calculated by  $f_l = -mg$  where  $m$  is mass of the weight and  $g$  is gravitational acceleration. The model from the input load to the output force is considered as a mass-spring-damper model, and is expressed as a second order system. By applying the least squares methods, the force-displacement model was derived as

$$G_{FY} = \frac{2.58 \times 10^4}{s^2 + 13.11s + 2.118 \times 10^3} . \quad (41)$$

The identification result is shown in Figure 45. In this figure, the experimental data and simulated data of the identified model are plotted. Precision of model is 91.33 %. The simulation result agrees well with a dynamic response of the step load.

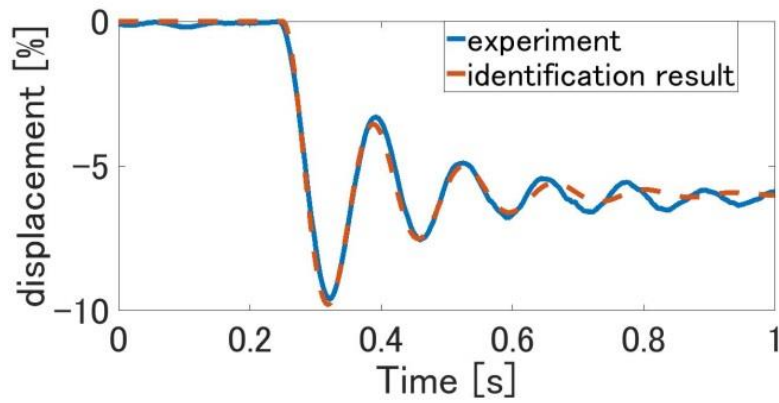
Next, we identified the voltage-displacement model from actuation response. In the experiment, a 50 g weight is attached to the end of actuator. A step voltage of 10 V is applied to the actuator. The model from the input voltage to the output displacement is assumed to be expressed as the linear time-invariant model in a similar way. The order of the model is selected adequately under the condition of second or higher order so as to make the voltage-force model proper. In the same way to the above, the model was derived as a second order model

$$G_{VY} = \frac{6.3809}{s^2 + 12.49s + 7.709} . \quad (42)$$

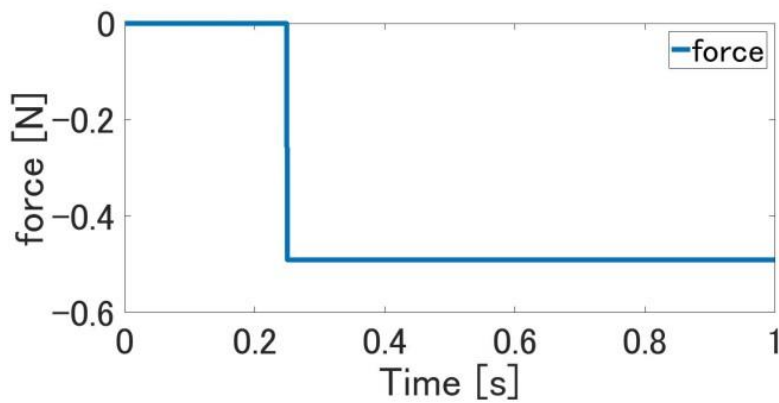
The identification result is shown in Figure 46. Precision of model is 86.74 %. The simulation result agrees well with the experimental data.

Finally, the voltage-force model is calculated as  $G_{VF} = G_{VY} / G_{FY}$ . The model was obtained using the equation (41) and (42) as

$$G_{VF} = \frac{2.472s^2 + 32.41s + 5.236 \times 10^3}{s^2 + 12.49s + 7.709} \quad (43)$$

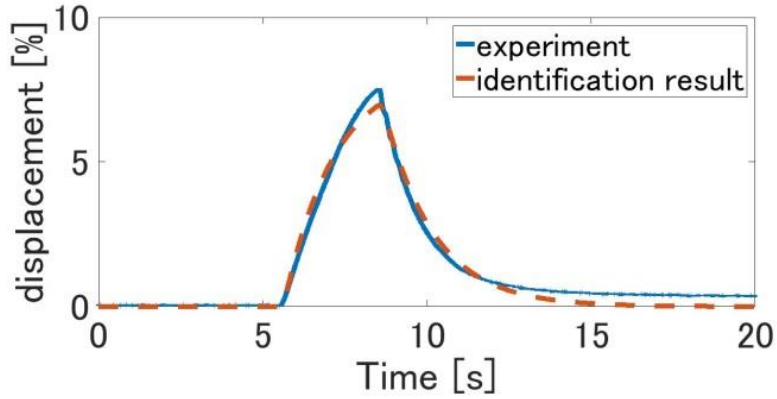


(a) Identification result

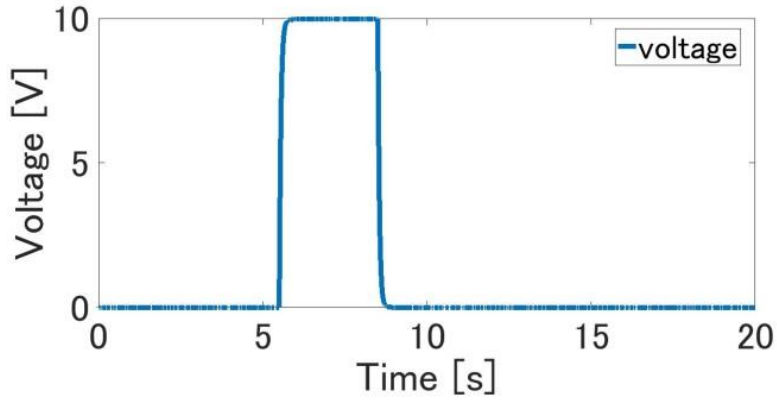


(b) Input force

**Figure 45.** Identification result of the force-displacement model



(a) Identification result



(b) Input voltage

**Figure 46.** Identification result of the voltage-displacement model

The numerical simulations were conducted by using MATLAB/Simulink. For investigating the effect of the antagonistic structure, we applied a proportional control as the control input is proportional to the deviation between the reference signal and the measured value of the displacement.

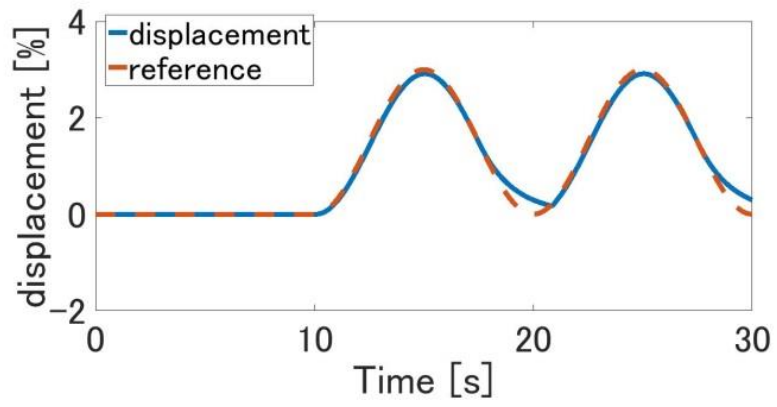
Figure 47 shows the result of single actuator, and Figure 48 shows the result of the antagonistic actuator. In the both cases, the proportional gains are set as 40. The reference signals are set as a sin wave with an amplitude of 3 % and a frequency of 0.1 Hz. Note that the reference signals are set within the range of positive value, i.e. from 0 % (equilibrium state) to +3 % since the single actuator cannot expand from the initial length. The maximum input voltage  $v_{max}$  and the minimum input voltage  $v_{min}$  are set as 10 V and -10 V, respectively.

In case of the single actuator of Figure 47, the input voltage was restricted to zero when the actuator stretched back and the tracking errors arose. This behavior is inevitable since a negative input for cooling cannot be applied. The quick rise and jiggly variation of the input voltage were found at around 21 s. This behavior is caused by the variation of the tracking error as the reference signal

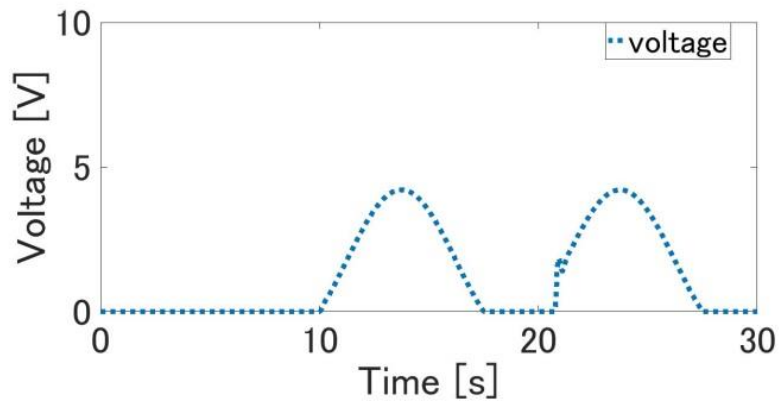
reached to the displacement and the recovery from the input saturation and the inversion of the error occurred suddenly.

In case of the antagonistic-type actuator in Figure 48, the tracking errors decreased due to the effect of the negative inputs by the antagonistic structure. In this numerical simulation, we applied the asymmetric reference signal to the equilibrium state. Therefore the input voltages of two actuators were different. As seen in Figure 48 (b), the input voltage of the actuator 2 was applied during latter term of stretch back motion, as the tracking error become negative. In the numerical simulations, the displacement control can be realized in the same response performance for other amplitude and frequency of the target signal if the input voltages are within the upper limitation of the input saturation.

To confirm the validity of the method in more detailed, other simulations with pulse reference signals were demonstrated. The simulation results are shown in Figure 49 and Figure 50, where the amplitude of the pulse reference signals are set as the value from 1 to 3 %. In all cases of the single actuator of Figure 49, although the input voltages were saturated in rising term, the contraction motions of the actuators were relatively fast and conversed to constant values near the reference signals quickly. However, the expansion motions were quite slow and the tracking errors become large. On the other hand, in cases of the antagonistic actuator of Figure 50, the expansion motions were improved by the effect of the antagonistic structure. Although steady-state errors and rising time increased due to the stiffness increase of the actuator, the control performance can be improved by applying a PID controller.

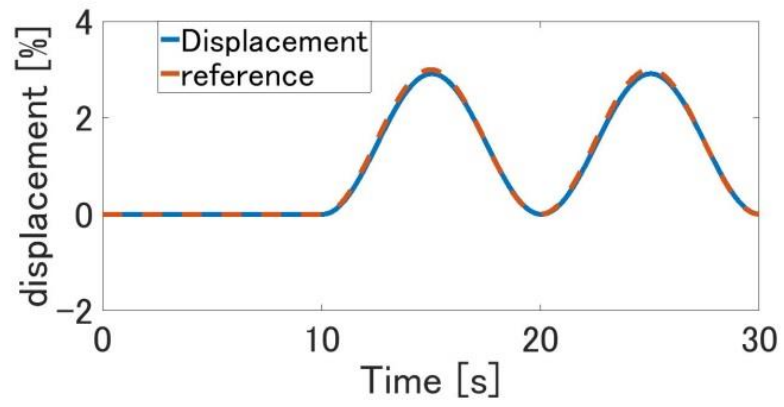


(a) Displacement

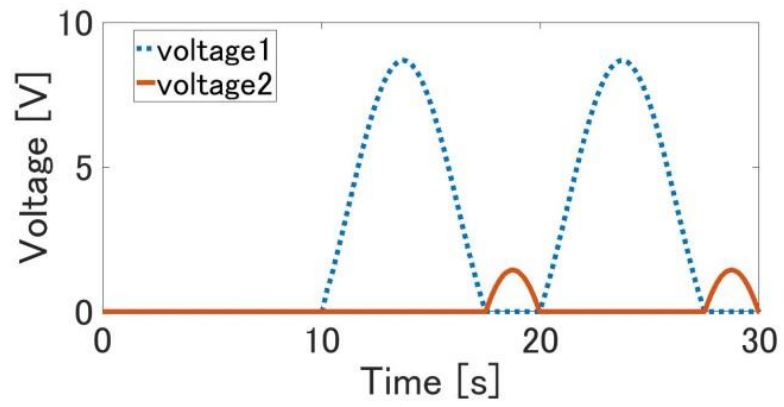


(b) Voltage

**Figure 47.** Simulation result of single actuator

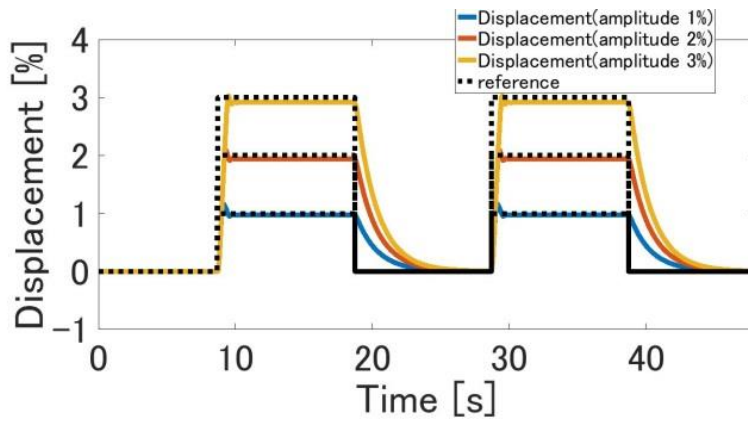


(a) Displacement

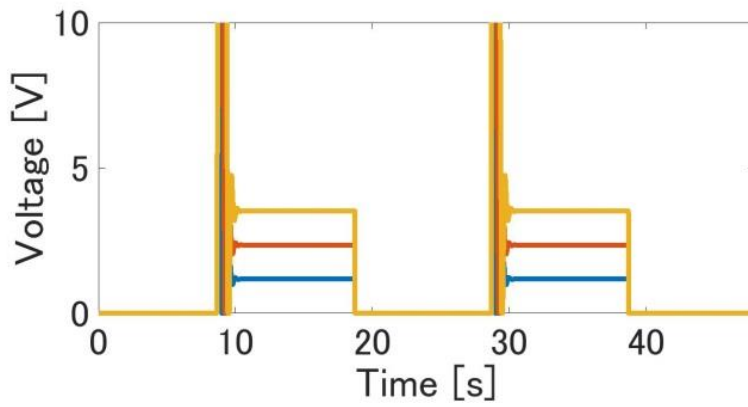


(b) Voltage

**Figure 48.** Simulation result of antagonistic actuator

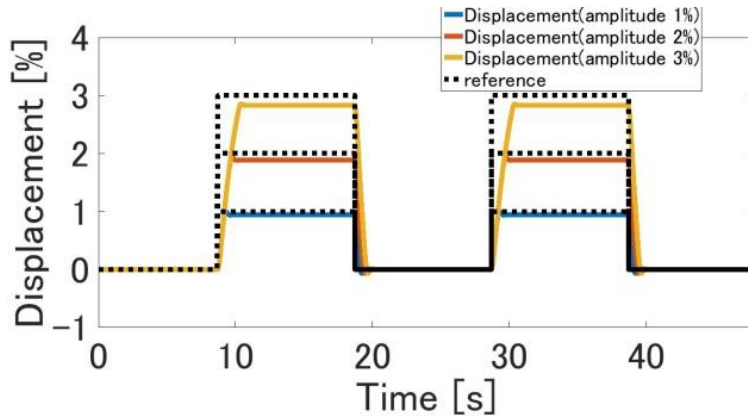


(a) displacement

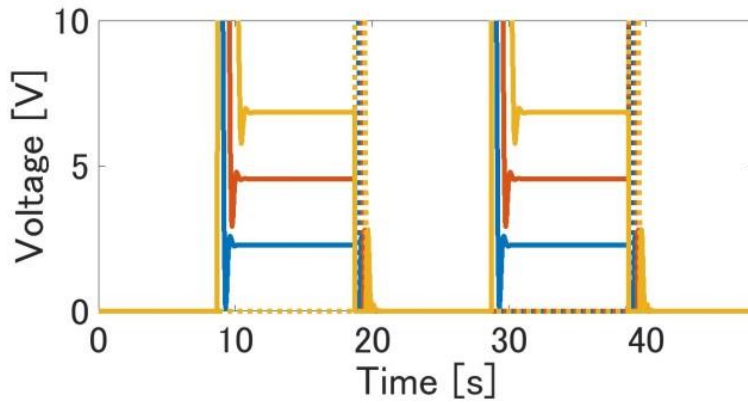


(b) input voltage

**Figure 49.** Simulation result of a single actuator in pulse wave



(a)displacement



(b) input voltage  $v_1$ (the solid line) and  $v_2$  (the dotted line)

**Figure 50.** Simulation result of an antagonistic actuator in pulse wave

### 4.2.3. Experiment verification of the displacement control

We investigate the validity of the antagonistic-structure through experiments. To verify the effect of the antagonistic structure, the proportional controller is applied as same as the numerical simulations. The setting of the reference signal is the same as above simulations. A schematic diagram of our experimental environment is shown in Figure 51. In the environment, the control input signals are calculated by using the measured displacement and reference signal in a digital signal processor (MTT, SBOX2). The control signal from the computer is applied to the power supply (KIKUSUI, PMX18-2A), which can output the driving voltage according to control signals. The displacement of the actuator is measured by a laser displacement meter (KEYENCE, LA-100). The displacement data is recorded to the computer through a multifunction I/O device (MTT, I/O board). In this experiment, control programs are implemented by using MATLAB/Simulink. The sample time of the controller is set as 0.001 s. In this experiment, room temperature is set as 23 °C as same as the modelling experiment. A weight of 50 g is hung on the other side of the actuator.

Experimental results are shown in Figure 52 and Figure 53. From Figure 52, large errors are observed when the actuator stretched back since negative control inputs were not applied. From Figure 53, as with the simulation result, the tracking errors in the antagonistic actuator decreased when the actuator stretched back since the inputs to both sides can be applied. Compared to the result of the single actuator, the tracking error of the antagonistic-type actuator decreased, especially in the stretching back to the initial length. The maximum error decreased from 0.6515% to 0.1466%.

Next, to evaluate the effect of the antagonistic-structure and control system, other experiments with the pulse reference signals. The experiment results are shown in Figure 54 and Figure 55. As the same way as the numerical simulations, the amplitude of the pulse reference signals are set as the value from 1 to 3 %. Although small vibrations of the displacement were observed, the experimental results show similar finding to the numerical simulation results.

In cases of the single actuator of Figure 54, the actuator contracted fast and the displacement converged to constant values near the reference signals quickly. When the reference signals return to the zero position, the actuator stretched back slowly since negative input cannot be applied. Especially, in cases that the amplitudes of the reference signals were 2 % and 3 %, the displacement did not return to the zero position within 10 s. This behavior depends on a thermolytic action. The dissimilarity with the numerical simulations arises from unconsidered nonlinearity of Joule heating and thermal characteristics.

In cases of the antagonistic actuator of Figure 55, when the reference signals return to the zero position, the actuator stretched back fast. The response of the expansion motions were improved by the effect of the antagonistic structure. The response speed of expansion motions was almost same as that of contraction motions. As described in previous section, steady-state errors remained since we applied the proportional controller. The tracking performance is improvable with applying a feedback controller with integral action such as a PID control.

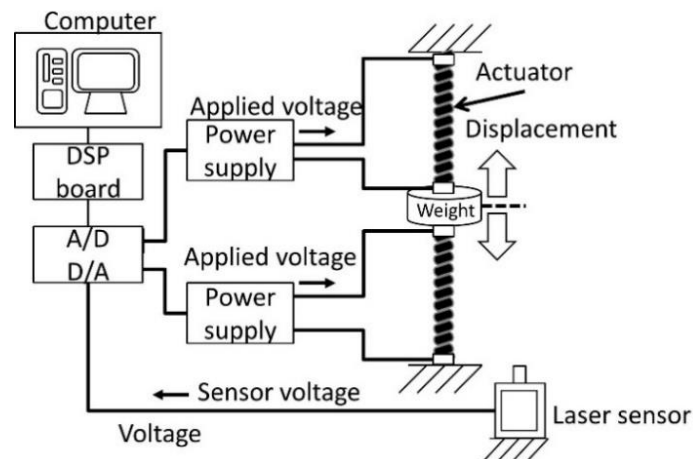
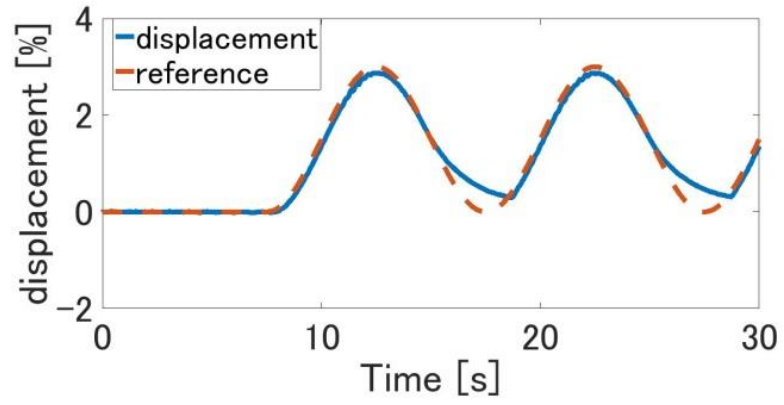
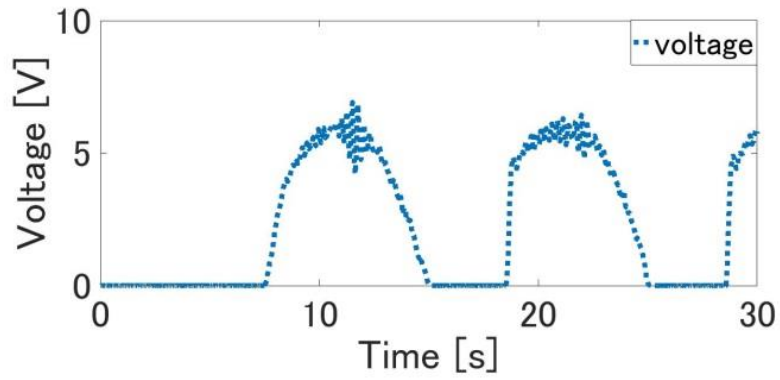


**Figure 51.** Experimental system

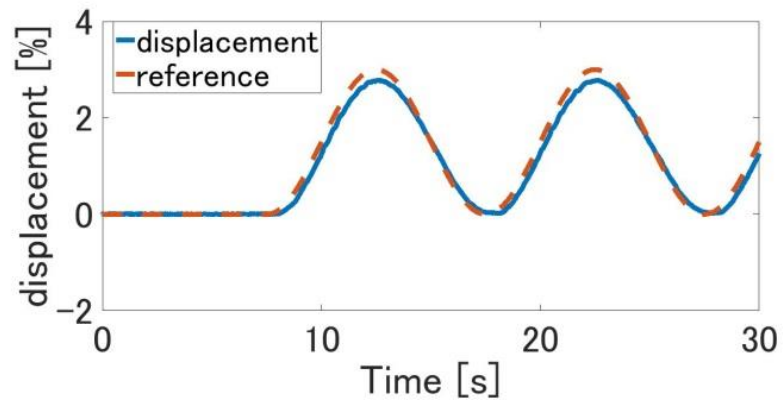


(a) Displacement

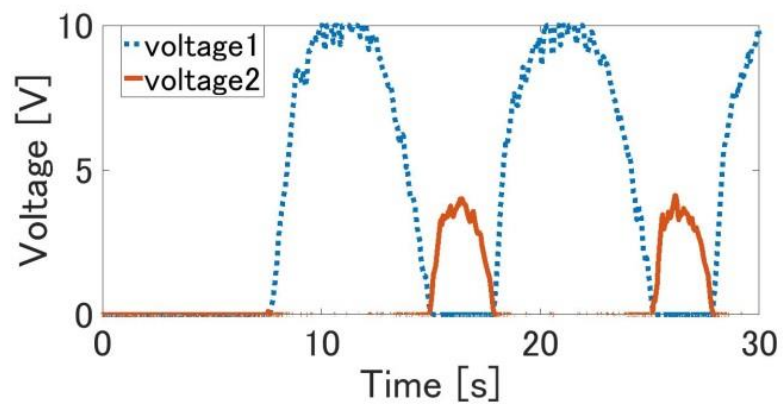


(b) Voltage

**Figure 52.** Experiment result of a single actuator

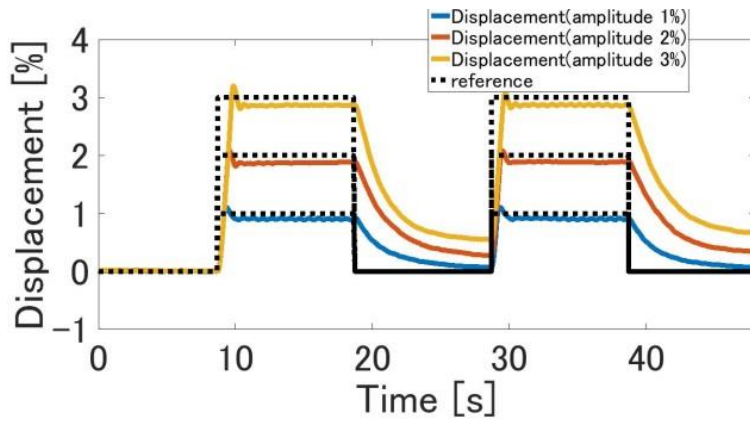


(a) Displacement

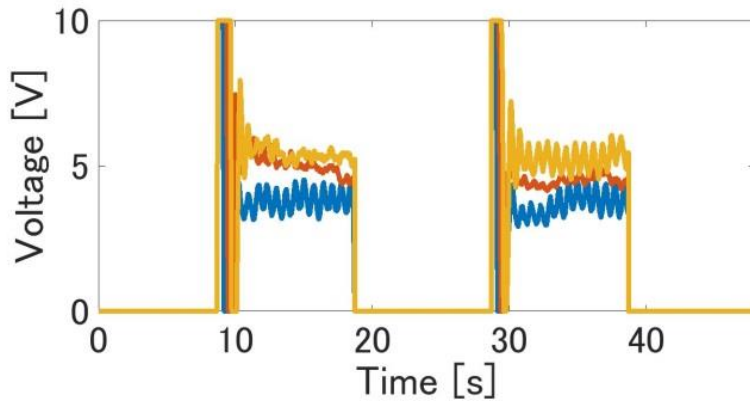


(b) Voltage

**Figure 53.** Experiment result of antagonistic actuator

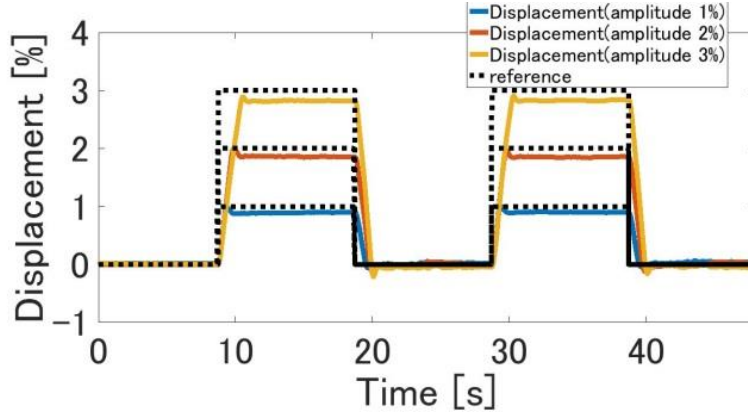


(a) Displacement and reference

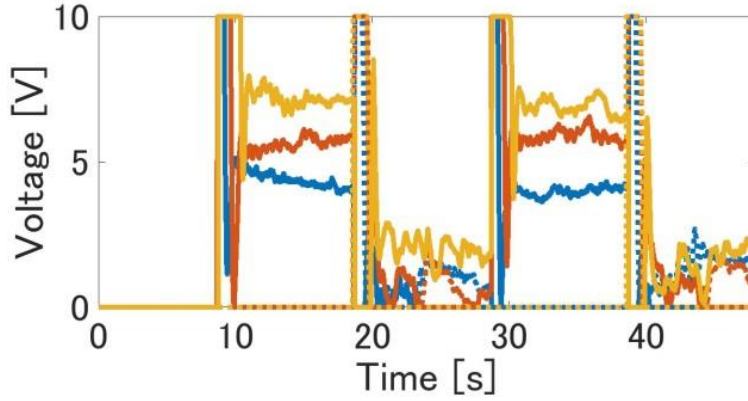


(b) Input voltage

**Figure 54.** Experiment results of a single actuator in pulse wave



(a) Displacement and reference



(b) Input voltage  $v_1$  (the solid line) and  $v_2$  (the dotted line)

**Figure 55.** Experiment results of an antagonistic actuator in pulse wave

To realize better controlled performance, 2 DOF controller is applied. A block diagram of 2 DOF controller is shown in Figure 56. This controller consists of two controllers, a feed-forward controller  $G_{FF}$  and a feedback controller  $G_{FB}$ , which are connected in parallel. In the control system, the feed-forward controller  $G_{FF}$  generates control input based on the identified model. The feedback controller  $G_{FB}$  generates control input from the deviation between the reference signal and the measured value of the displacement.

First, the design method of the feed-forward controller is explained. A reference model  $G_r$  is expressed as

$$G_r = \frac{1}{(T_s s + 1)^2} \quad (44)$$

where  $T_s$  is a time constant. The open-loop transfer function of the actuator, which is the voltage-displacement model, is expressed as

$$G_{OL} = \frac{b_0}{s^2 + a_1s + a_0} \quad (45)$$

The feed-forward controller  $G_{FF}$  is given by the inverse dynamics of the actuator model as

$$G_{FF} = G_{OL}^{-1} \cdot G_r. \quad (46)$$

The input voltage of feedforward controller  $u_{FF}(s)$  is obtained as

$$u_{FF}(s) = G_{FF}r(s) \quad (47)$$

where  $r(s)$  is a reference signal.

Next, the design method of the feedback controller is explained. In this paper, the PID controller is designed based on the identified model and a pole placement method. The PID controller  $G_{PID}$  is given as

$$G_{PID}(s) = K_p + K_Ds + \frac{K_I}{s} \quad (48)$$

where  $K_P$  is a proportional gain,  $K_I$  is an integral gain, and  $K_D$  is a differential gain. The PID gains can be calculated by placing the poles of closed-loop transfer function of the system. Let  $p_1$ ,  $p_2$  and  $p_3$  be the desired poles. By comparing the coefficient of the denominator polynomials of the closed loop system, the PID gains are given as

$$K_p = \frac{p_1p_2 + p_2p_3 + p_1p_3 - a_0}{b_0} \quad (49)$$

$$K_D = \frac{-p_1 - p_2 - p_3 - a_1}{b_0} \quad (50)$$

$$K_I = \frac{-p_1p_2p_3}{b_0}. \quad (51)$$

The input voltage  $u_{FB}(s)$  of feedback controller was obtained using the equation (47) and (48) as

$$u_{FB}(s) = \left\{ K_p + sK_D + K_I \frac{1}{s} \right\} \{ G_r(s)r(s) - y(s) \}. \quad (52)$$

Finally, the control input to the actuator is applied as the summation of the feed-forward and feed-back controllers as

$$u(s) = u_{FF}(s) + u_{FB}(s). \quad (53)$$

In this experiment, the time constant of the reference model  $T_s$  is set as 0.01 s. The poles of closed loop system are set as  $(-10.5 \pm 10.5i)/\sqrt{2}$  and  $-10.5$ . The PID gains are calculated as  $K_p=81.001$ ,  $K_I=362.8407$ ,  $K_D=4.0305$  by the equation (49), (50) and (51).

Experimental results of feedforward control are shown in Figure 57. The displacement of the actuator was not tracking to the reference signal. It is considered that large error between reference values and displacement occurs due to the nonlinearity of the actuator dynamics. Experimental results of 2 DOF-PID control are shown in Figure 58. From the figure, it is observed that the PID controller compensate the tracking error, as the maximum error is 0.0949 %. The displacement control can be realized with sufficient tracking performance by the effect of the antagonistic structure and appropriate controller design.

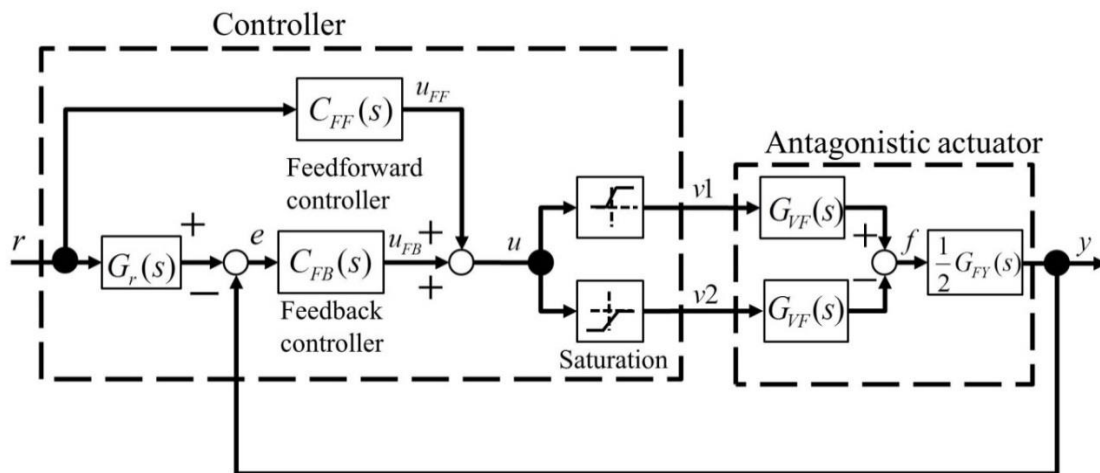
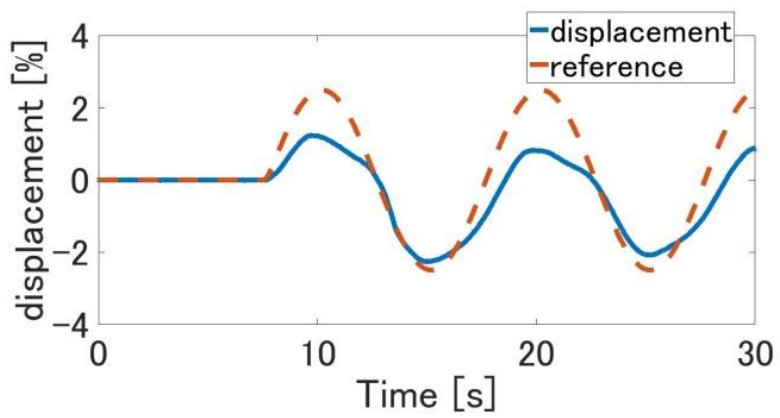
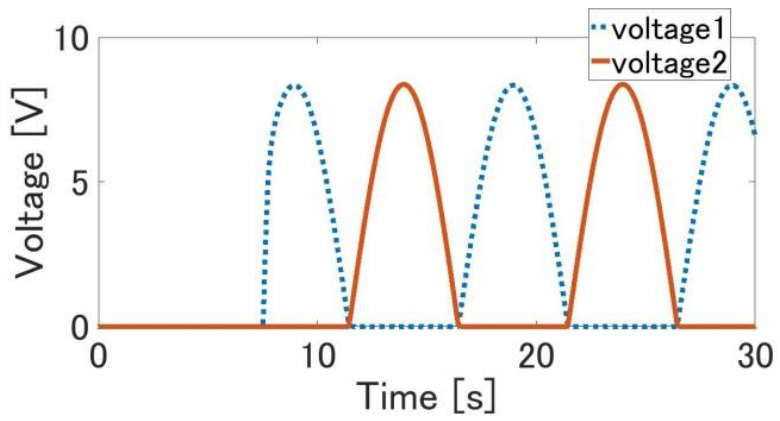


**Figure 56.** Block diagram of 2 DOF-PID control

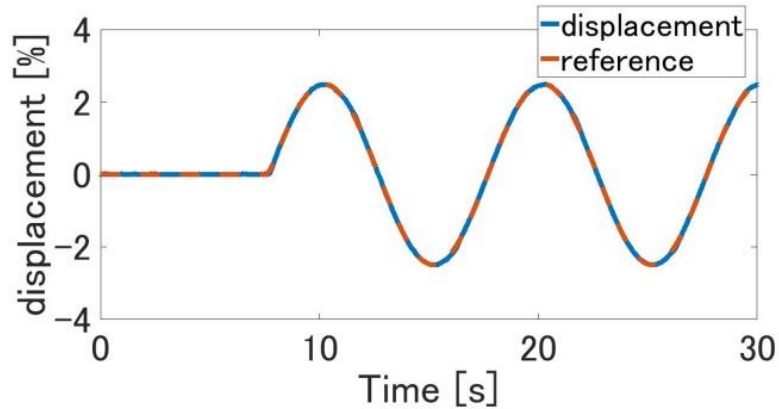


(a) Displacement

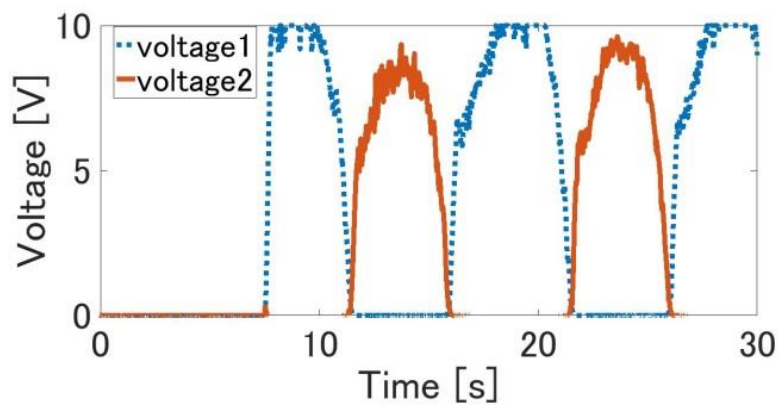


(b) Voltage

**Figure 57.** Experiment result of Feedforward control



(a) Displacement



(b) Voltage

**Figure 58.** Experimental result of 2DOF-PID control

### 4.3. Control system design for robot-arm with antagonistic-actuator

Applying the antagonistic-actuator to the manipulator, the robot-arm with TCPAs is demonstrated. In this section, we explain modeling and controller design of robot-arm. Numerical simulation and experiments results are explained.

#### 4.3.1. Modeling of robot arm

For numerical simulations and controller designs, the model of robot arm is derived. First, we derived the model of TCPA. The actuator model is described as Figure 59. Here, we assumed that the actuator

model consists of the mechanical model and the generated model. The mechanical property of the actuator is expressed as spring-mass-damper system;

$$G_{FY} = \frac{1}{m_a s^2 + ds + k} \quad (54)$$

where  $m_a$  is an mass of the actuator,  $d$  is coefficient of damper,  $k$  is coefficient of spring. The dynamics from  $p=v^2$  to  $y$  is expressed as

$$G_{PY} = \frac{1}{a_2 s^2 + a_1 s + a_0} \quad (55)$$

where  $a_i$  ( $i=0,1,2$ ) are parameters of dynamical model. Note that the order of the model is determined so that the generated model is proper. Therefore, the generated mode is calculated as

$$G_{PY} = \frac{m_a s^2 + ds + k}{a_2 s^2 + a_1 s + a_0} \quad (56)$$

These parameters are identified by using experiment data and n4sid function.

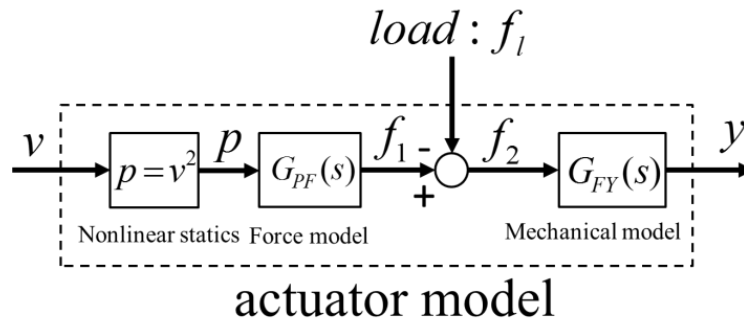


**Figure 59.** The block of diagram of actuator model

Using the actuator model, the model of robot arm is derived. The model of the robot arm is shown in Figure 60. Figure 61 shows a schematic overview of the robot arm, where two TCPA elements are arranged antagonistically. The robot arm without the actuator is expressed as 1 link manipulator as

$$(J + ml^2)\ddot{\theta} + c\dot{\theta} + mgl \sin \theta = \tau \quad (57)$$

where  $\theta$  is an angle of link,  $c$  is coefficient of viscosity,  $l$  is length of the link,  $\tau$  is a torque and  $m$  is mass of the link. These parameters were identified through experiments.

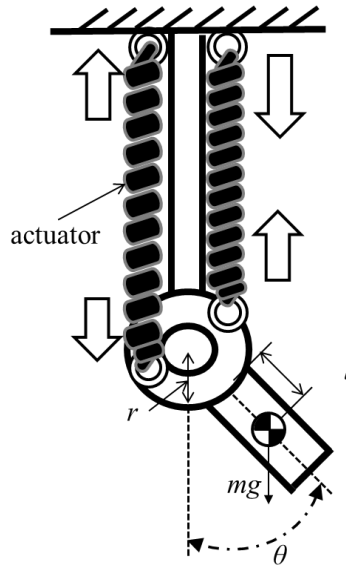


**Figure 60.** The model of robot arm

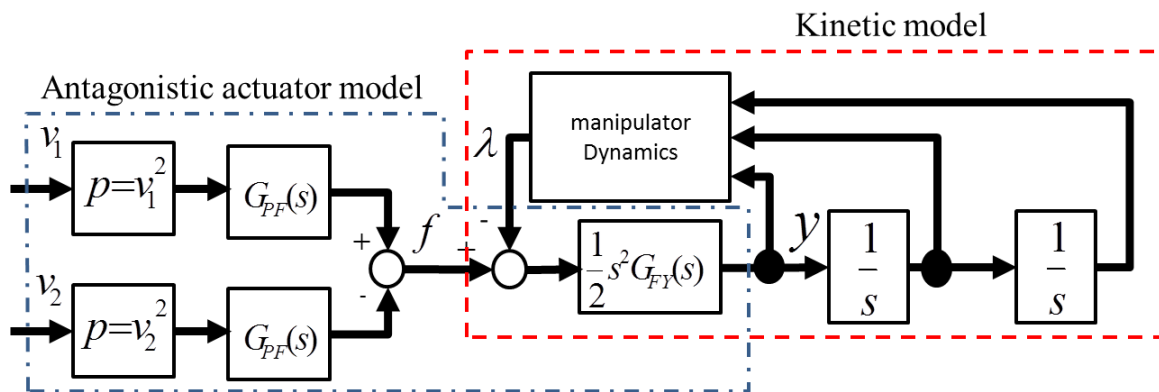


**Figure 61.** The block diagram of robot model

Here, the actuator dynamics is assumed to be expressed as loads of the manipulator. Based on assumption, the equation of the motion is described as the ordinary differential equation with constraint conditions between the actuator and the link. The model of the actuator and manipulator is described as affine systems separately:

$$\frac{dx_a}{dt} = f_a(x_a) + g_a(x_a)u_a \quad (58)$$

$$\frac{dx_l}{dt} = f_l(x_l) + g_l(x_l)u_l \quad (59)$$

From the equations, an augmented system is described as

$$x = \begin{bmatrix} x_a \\ x_l \end{bmatrix}, f(x) = \begin{bmatrix} f_a(x_a) \\ f_l(x_l) \end{bmatrix}, g(x) = \begin{bmatrix} g_a(x_a) & 0 \\ 0 & g_l(x_l) \end{bmatrix}, u = u_a \quad (60)$$

$$\frac{d}{dt}x = f(x) + g(x)u$$

Here, a constraint conditions is assumed to be represented as

$$h(x) = y - r\theta = 0 \quad (61)$$

Furthermore, a constraint force  $\lambda$  is assumed to be represented as

$$\frac{dx}{dt} = f(x) + g(x)u - g_c(x)\lambda \quad (62)$$

$$L_{g_c} h\lambda = 0$$

where  $L$  is Lie differential. Therefore, the dynamics of robots is simulated by the equation (62).

### 4.3.2. Control system design for robot arm

For realizing the motion control of the robot arm, the control system is designed. Figure 62 shows the control system of the robot arm. The normal length of each element is same. Since negative inputs for extending cannot be applied, the expanding motion depends on natural cooling. The robot arm can generate torque in both CCW and CW directions. Therefore, the response in the expansion motion can be improved by the antagonistic action. The control input of the antagonistic-type actuator is divided into positive and negative and applied to each element. In this robot-arm, windup phenomena may be caused by load variation due to manipulator dynamics and antagonistic-structure. Although Chapter 3 shows three feedback control methods, the feedback controller  $C(s)$  is applied as the PI control with anti-windup compensator for eliminating the influence of the windup. The parameter of the controller

is  $K_p = 400$ ,  $K_I = 50$ . The maximum input voltage and the minimum input voltage are set as 10 V and -10 V, respectively.

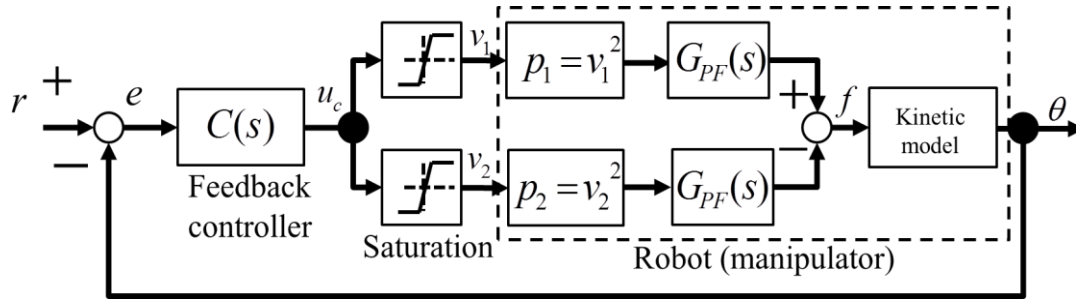
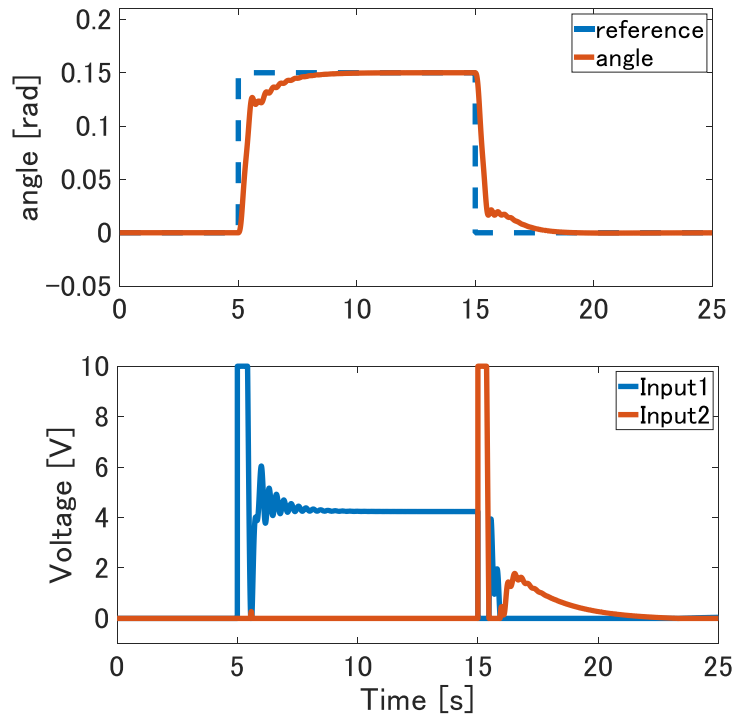


Figure 62. The control system of the manipulator

### 4.3.3. Numerical simulations and experiments

The validity of the control system is investigated through experiments. In this simulation, the simulation program is built in MATLAB/Simulink. In our numerical simulation, an ordinary differential equation was solved by using the Ode45 function of MATLAB. The reference signal is applied as the pulse signal.

The simulation result is shown in Figure 63. Although the input voltage is saturated, the angle of the robots converges to the reference signals. Although the input saturation is caused, the steady state error is eliminated and the control result is stable due to PI-AW controller. The experiment result is shown in Figure 64. Although the minor error is occurred, the angle converges to the reference signal as same with the numerical simulation. These errors are considered to be caused due to frictions between the actuator and the manipulator or nonlinear dynamics of actuator. From these results, our proposed control system can control of the robots.



**Figure 63.** Numerical simulation results of motion control

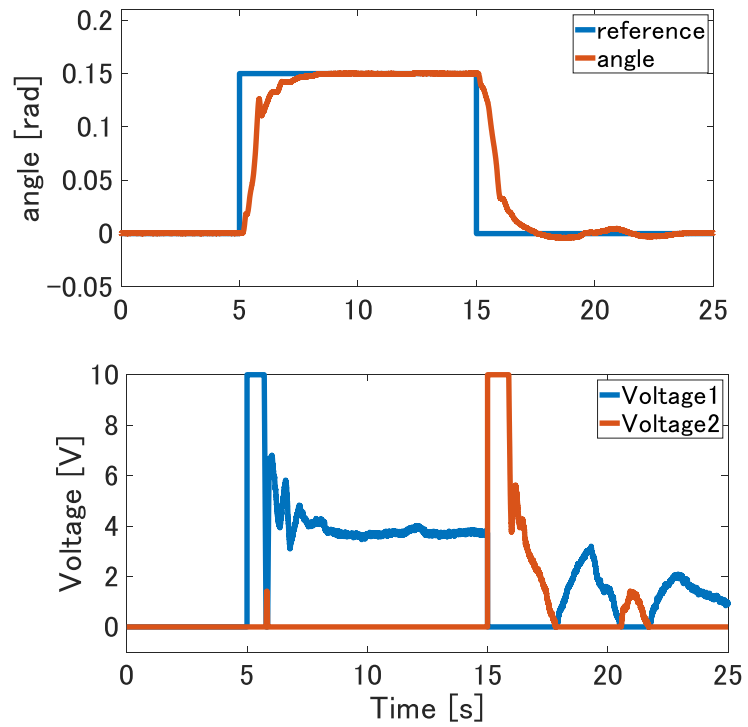


**Figure 64.** Experiment result of motion control

#### **4.4. Summary**

In this chapter, the antagonistic-type actuator of TCPA was proposed to compensate the asymmetric response characteristics. The validity of the antagonistic structure was investigated through the numerical simulations and experiments by applying simple proportional feedback control. The response speed in stretching state was improved and the tracking error decreased. In addition, the validity of the 2 DOF-PID control of the antagonistic-type actuator was investigated through the experiment. Furthermore, we demonstrated the robotic application of TCPAs. The antagonistic actuator was applied to 1link manipulator for verifying validity of our proposed control system. For numerical simulations, the actuator model and manipulator model was derived. Based on these models, the model of the robots was derived. We applied the feedback controller as The PI-AW control because the control signals is saturated by load variation. The validity of the control performance was investigated through numerical simulations and experiments. From numerical simulations and experiments, the angle control system based on PI-AW control can realize the good control results.

## 5. Conclusion

In this thesis, the simple and robust control system of the TCPA was proposed for applications. For control system design, we investigated the response properties by using a frequency response analysis. From experiment results, the simple model considering materials properties was derived based on experiments results. Furthermore, to solve problem of input-saturation, parameter-variation and tuning of controller, the control system design had been proposed. The validity of the control system design was verified through numerical simulations and experiments. Based on acknowledgment of modeling and controller design, we demonstrated the robotic applications. An antagonistic actuator was applied to the 1link manipulator. The control performance was investigated through numerical simulations and experiments.

In modeling experiments, the simple actuator model consisting a nonlinear statics and linear dynamics can be derived based on frequency response analysis. Our model can simulate the actuator properties and implemented easily. In control system design, our proposed control system can achieve good control results compared to conventional control methods. Our proposed model and control system design can be applied in common and be implemented because of simplify for applications. Therefore, our methods in this thesis can realize the simple and robust control system for the applications of TCPA.

In future works, we will achieve the fast motion of TCPAs for robotic application. The fabrication methods will be investigated for realizing fast motions. Furthermore, the speed control system or force control system will be designed for the robot using the TCPA Although the actuator model is identified by experiment-data in this thesis, the white box model of actuator will need for realizing control system design.

## References

- [1] Mirvakili S. M. and Hunter I. W. 2017 Multidirectional artificial muscles from nylon. *Advanced Materials*, **29**.
- [2] Asaka K. Oguro K., Nishimura Y. Mizuhata M., Takenaka H. 1995 Bending of polyelectrolyte membrane-platinum composites by electric stimuli I. response characteristics to various waveforms. *Polymer Journal*, **27**, 436-440.
- [3] Pelrine E. R., Roy D. R., Jose. P. J. 1998 Electrostriction of polymer dielectrics with compliant electrodes as a means of actuation. *Sensors and Actuators A: Physical*, **64**, 77-85.
- [4] Gursel A., Nam. N. H. 2006 Predicting force output of trilayer polymer actuator. *Sensors and Actuators A: Physical*, 616-625.
- [5] Haines C S *et al.* 2014 Artificial muscles from fishing line and sewing. *Science* **343** 868-872
- [6] Cho K H, Song M G, Jung H, Park J, Moon H, Koo J C, Nam J D, and Choi H R 2016 A robotic finger driven by twisted and coiled polymer actuator. *Proc. SPIE* **9798** 97981J
- [7] Simeonov A., Henderson T., Lan Z., Sundar G., Factor A., Zhang J., Yip M. 2018 Bundled Super-Coiled Polymer Artificial Muscles: Design, Characterization, and Modeling. *IEEE Robotics and Automation Letters*, **3**, 1671-1678.
- [8] Edmonds B. P.R. and Trejos L. A. 2017 Stiffness control of a nylon twisted coiled actuator for use in mechatronic rehabilitation devices. *Proc. IEEE International Conference on Rehabilitation Robotics* 1419-1424
- [9] Mirvakili S. M., Ravandi A. R., Hunter I. W., Haines C. S., Li N., Foroughi J., Naficy S., Spinks G. M., Baughman R. H. and Madden J. D. W. 2014 Simple and strong: twisted silver painted nylon artificial muscle actuated by Joule heating. *Proc. SPIE* **9056** 90560I
- [10] Wu L., Andrade M. J., Rome R. S., Haines C., Lima M. D., Baughman R H. and Tadesse Y. 2015 Nylon-muscle-actuated robotic finger. *Proc. SPIE* **9431** 94310I
- [11] Wu L., Andrade D. J. M. and Saharan K. L. 2016 Compact and low-cost humanoid hand powered by nylon artificial muscles. *Smart Mater. Struct.* **12** 026004
- [12] Saharan L., Andrade D. J. M., Saleem W. and Baughman H. R. 2017 iGrab: hand orthosis powered by twisted and coiled polymer muscles. *Smart Mater. Struct.* **26** 105048
- [13] Yip M. C. and Niemeyer G. 2015 High-performance robotic muscles from conductive Nylon sewing thread. *Proc. IEEE International Conference on Robotics and Automation* 2315-2316
- [14] Sutton L., Moein H., Rafiee A., Maddan J. D. W. and Menon C. 2016 Design of an assistive wrist orthosis using conductive nylon actuator. *Proc. IEEE International Conference on Biomedical Robotics and Biomechanics* 1074-1079

- [15] Hiraoka M., Nakamura K., Arase H., Asai K., Kaneko Y., John S. W., Tagashira K. and Omote A. 2016 Power-efficient low-temperature woven coiled fibre actuator for wearable applications. *Scientific Report* **6** 36358
- [16] Wu L., Andrade D. J. M., Brahme T., Tadaesse Y. and Baughman H. R. 2016 A reconfigurable robot with tensegrity structure using nylon artificial muscles. *Proc. SPIE* **9799** 97993K.
- [17] Li H., Liu L., Xiao T. and Ang H. 2016 Design and simulative experiment of an innovative trailing edge morphing mechanism driven by artificial muscles embedded in skin. *Smart Mater. Struct.* **25** 095004
- [18] Almubarak Y. Maly N. S., Tadesse Y. 2018 Fully embedded actuators in sinusoidal elastomeric skin for use in humanoid robots. *Proc. SPIE*, 10594, 1059416
- [19] Wu L. Karami F., Hamidi A., Tadesse Y. 2018 Biorobotic systems design and development using TCP muscles. *Proc. SPIE*, 10594, 1059417
- [20] Yip M C and Niemeyer 2017 On the Control and Properties of Supercoiled Polymer Artificial Muscles. *IEEE Transactions on robotics* vol. **33** No. 3 687-699
- [21] Arakawa T., Takagi K., Tahara K. and Asaka K. 2016 Position control of fishing line artificial muscles (coiled polymer actuators) from nylon thread. *Proc. SPIE* **9798** 97982W
- [22] Masuya K., Ono S., Takagi K. and Tahara K., 2017 Nonlinear dynamics of twisted and coiled polymer actuator made of conductive Nylon based on the energy balance. *Proc. IEEE International Conference on Advanced Intelligent Mechatronics* 779-784
- [23] Saharan L. and Tadesse Y. 2016 Fabrication parameters and performance relationship of twisted and coiled polymer muscles. *Proc. The ASME 2016 international mechanical engineering congress and exposition IMECE 2016* 67314
- [24] Luong A. T., Cho H. K., Song G. M., Koo C. J., Choi R. H. and Moon. H 2017 Nonlinear Tracking Control of a Conductive Supercoiled Polymer Actuator. *Soft robotics* **4** 607-612
- [25] Jafarzadeh M., Gans N., Tadesse Y. 2018 Control of TCP muscles using Takagi–Sugeno–Kang fuzzy inference system. *Mechatronics* **53** 124-139
- [26] Sharafi S. and Li G. 2015 A multiscale approach for modelling actuation response of polymeric artificial muscles. *Soft Matter* **11** 3833-3843
- [27] Yanf Q. and Li G. 2016 A top-down multi-scale modelling for actuation response of polymeric artificial muscles. *Journal of the Mechanics and Physics of Solids* **92** 237-259
- [28] Cho K. H., Song M. G., Jung H., Yang S. Y., Moon H., Koo J. C., Nam J. and Choi H. R. 2016 Fabrication and modeling of temperature-controllable artificial muscle actuator. *Proc. 6th IEEE International Conference on Biomedical Robotics and Biomechanics (BioRob)* 94-98
- [29] Abbas A. and Zhao J. 2017 A physics based model for twisted and coiled polymer actuator. *Proc. IEEE International Conference on Robotic and Automation* 6121-6126
- [30] Masuya K., Ono S., Takagi K. and Tahara K., 2017 Modeling framework for macroscopic dynamics of twisted and coiled polymer actuator driving by joule heating focusing on energy and convective heat transfer. *Sensor and actuator* vol. 267 443-454

- [31] Karami F. and Tadesse Y. 2017 Modeling of twisted and coiled polymer(TCP) muscle based on phenomenological approach, *Smart mater. Struct.* **26** 125010
- [32] Tang X. Liu Y. Li K., Chen W., Zhao J. 2018 Finite element and analytical models for twisted and coiled polymer actuator. *Materials Research Express*, **5**, 015701.
- [33] Arakawa T., Masuya K., Ono S., Takagi K. and Tahara K. 2016 Position control of twisted and coiled polymer actuator using a controlled fan for cooling. *Proc. SPIE* **10163** 101632V
- [34] Sutton L., Moein H., Rafiee A., Maddan J. D. W. and Menon C. 2016 Design of an assistive wrist orthosis using conductive nylon actuator. *Proc. IEEE International Conference on Biomedical Robotics and Biomechatronics* 1074-1079
- [35] Peng Y., Vracic D. and Hanus R. 1996 Anti-windup, bumpless, and conditioned transfer techniques for PID controllers. *IEEE Control System* Vol. **16** 48-57
- [36] Hanus R., Kinnaert M. and Henrotte J. L. 1987 Conditioning technique, a general anti-wind up and bumpless transfer method. *Automatica* **23** 607-612
- [37] Nakano M., Ohnishi K., Miyachi K. 1987 A Robust decentralized joint control based on interference estimation. *Proc. International Conference on Robotics and Automation* **4** 326-331
- [38] Astrom J. K. and Richard M. M. 2009 Feedback systems: an introduction for scientists and engineers (USA: Princeton university). 150-155
- [39] Astrom J. Karl. and Hagglund T. 1998 PID controllers: theory, design, and tuning 2<sup>nd</sup> edition (USA:The Instrumentation, Systems, and Automation Society) . 170-180
- [40] Morari M., Zafirou E. 1989 Robust Process Control (USA:Prentice hall). 39-56